Clemson University
TigerPrints

All Dissertations | Dissertations

8-2018

Computational Modeling of Nonlinear Behavior in Orthopaedics

Kyle Snethen
Clemson University, kyle.snethen@gmail.com

Follow this and additional works at: https://tigerprints.clemson.edu/all_dissertations

Recommended Citation
Snethen, Kyle, "Computational Modeling of Nonlinear Behavior in Orthopaedics" (2018). *All Dissertations*. 2184.
https://tigerprints.clemson.edu/all_dissertations/2184

This Dissertation is brought to you for free and open access by the Dissertations at TigerPrints. It has been accepted for inclusion in All Dissertations by an authorized administrator of TigerPrints. For more information, please contact kokeefe@clemson.edu.

COMPUTATIONAL MODELING OF NONLINEAR BEHAVIOR IN ORTHOPAEDICS

A Dissertation
Presented to
the Graduate School of
Clemson University

In Partial Fulfillment
of the Requirements for the Degree
Doctor of Philosophy
Bioengineering

---

by
Kyle Snethen
August 2018

Accepted by:
Melinda K. Harman, Committee Chair
Hai Yao, PhD
Guigen Zhang, PhD
Kyle Jeray, MD

ABSTRACT

Total knee replacement (TKR) is one of the most common orthopaedic procedures performed in the USA and is projected to exceed 4.3 million by 2030. Although TKR surgery has a success rate of 95% at 10 years for most TKR designs, revision surgery still occurs approximately once for every ten primary TKR surgeries. Failure modes in TKR involve the interplay between implant mechanical performance and surrounding biological tissues. The orthopaedic community has turned to computational modeling as an effective tool to analyze these complex interactions and improve patient outcomes. The objective of these studies was to utilize a combined computational and experimental approach to investigate modes of TKR failure where material nonlinearity plays a significant role in the biomechanics under investigation.

A finite element (FE) model of a modular TKR taper junction was developed in order to investigate the stress environment in relation to corrosive behavior under *in vivo* loading conditions. Linear elastic and elastoplastic material models were defined and angular mismatch parametrically varied in order to determine the sensitivity of model predicted stresses to material model selection and taper junction geometry. It was determined that positive angle mismatches cause plastic deformation and overestimated stresses in linear elastic analyses compared to elastoplastic analyses. Calculated stresses were also strongly correlated with angle mismatch when varied $\pm 0.25^{o}$. Model stress distributions agreed with corrosion patterns evident on retrieved modular TKR components and magnitudes corresponding with corrosive behavior *in vitro*.

Additionally, a series of passive FE TKR models were developed in order to investigate the intrinsic relationship between TKR component alignment, ligament tensions, and knee kinematics during intraoperative assessments. A kinematically-driven model was developed and validated with an open source dataset, and was able to discriminate clinical outcomes based on calculated ligament tensions when input *in vivo* kinematics. Patient-specific simulations found greater tension in lateral ligaments for poor outcome patients compared to good outcome patients, and statistically significant differences in tensions for the POL, PFL, DMCL, and ALS ligaments during mid-flexion. A force-driven model was also developed and validated with *in vitro* cadaver testing, and found that variation in tibial component alignment of $\pm 15^{o}$ influence intraoperative ligament tensions. However, definitive trends between TKR component alignment and ligament tension were not discerned. Nonetheless, both modeling approaches were found to be sensitive to subclinical abnormalities.

These findings suggest mechanical stress is a key contributor to taper junction corrosion and that ligament tensions are the mechanism leading to abnormal function in the passive TKR knee. These studies contributed innovative computational models that provide a foundation to advance the understanding of these complex relationships, and modeling frameworks that exemplify sound verification and validation practices.

DEDICATION

I dedicate this work to my wife, Gabrielle, who has supported me since day one of this journey, and I am grateful for her belief in me and the sacrifices she has made to allow me to pursue this accomplishment. I also dedicate this work to our two boys Clayton and Oliver, who have provided me constant joy in life and kept me humble to my true goals of being a caring and attentive father despite the hardships of this pursuit. I hope this dissertation serves as a reminder to them that with hard work, they can accomplish anything they set their minds to.

ACKNOWLEDGMENTS

I would like to acknowledge my advisor, Dr. Melinda Harman, for serving as a mentor to me beyond my research and being one of my strongest advocates. Her continuous support and dedication provided an environment to succeed. I would also like to thank my committee members, Dr. Hai Yao, Dr. Guigen Zhang, and Dr. Kyle Jeray for offering their expertise and guidance throughout my research.

In addition, I acknowledge Dr. Clare Fitzpatrick as her collaborative efforts and guidance during model development were pivotal in my research. I am also grateful for the assistance of Dr. James Cameron, Dr. Rob Carlisle, Jay Barnhardt and Stephanie Tanner during cadaver testing. Finally, I acknowledge assistance from my past and current lab colleagues, Madeline Bebler, Jorge Hernandez, and Zachary Hargett.

TABLE OF CONTENTS

Page

Table of Contents (Continued)

Page

Table of Contents (Continued)

Page

LIST OF TABLES

List of Tables (Continued)

Table Page

LIST OF FIGURES

List of Figures (Continued)

Figure Page

List of Figures (Continued)

Figure Page

List of Figures (Continued)

Figure Page

List of Figures (Continued)

Figure Page

List of Figures (Continued)

Figure Page

LIST OF ABBREVIATIONS AND ACRONYMS

3D	Three-dimensional
ACL	Anterior cruciate ligament
ALS	Anterolateral structure
ANOVA	Analysis of variance
AP	Anterior-posterior
COF	Coefficient of friction
CT	Computed tomography
DMCL	Deep medial collateral ligament
DOF	Degrees of freedom
DVRT	Differential variable reluctance transducer
E	Elastic modulus
FE	Finite element
FEA	Finite element analysis
FEM	Finite element method
HIP	Hot isostatic pressing
IE	Internal-external
LCL	Lateral collateral ligament
MAC	Mechanically assisted corrosion
MCL	Medial collateral ligament
ML	Medial-lateral
PC	Posterior capsule

PCL	Posterior cruciate ligament
PDE	Partial differential equation
PFL	Popliteofibular ligament
POL	Posterior oblique ligament
PT	Patellar tendon
QT	Quadriceps tendon
RMSE	Root mean square error
ROM	Range of motion
SI	Superior-inferior
THR	Total hip replacement
TKR	Total knee replacement
UHMWPE	Ultra-high-molecular-weight polyethylene
UTS	Ultimate tensile strength
VV	Varus-valgus
YS	Yield strength

Abbreviations and acronyms are redefined in each chapter for the reader's convenience.

PREFACE

Broad Objective and Specific Aims

Nonlinearity in implanted biological systems includes material nonlinearity (e.g. yield and hardening of implant materials or fibril recruitment in soft tissues), geometric nonlinearity (e.g. large deformations), and implant-tissue interface interactions (e.g. bond strength, contact friction). Computational finite element modeling has been used to investigate the mechanics and kinematics of the implanted knee joint for decades; however, finite element models often simplify these relationships by assuming linear properties due to computing cost and insufficient experimental data. Computational simulation of the implanted knee joint is significantly influenced by model input parameters, especially material behavior, and proper representation of material nonlinearity is essential for accurate prediction of model outputs. A finite element model of an implanted knee system consists of metallic implant components that can exhibit nonlinear yield behavior even when designed to function within elastic limits and soft-tissue structures that exhibit a nonlinear mechanical response under *in vivo* conditions due to their inherent biological composition.

The broad objective of this dissertation is to accurately represent material nonlinearity for analysis of the implanted knee joint by focusing on different aspects of TKR where material nonlinearity plays a major role in the biomechanics of the system under investigation. Through a combined experimental and computational approach, the following aims are addressed:

Aim 1. Determine the stresses within modular taper junctions using finite element analysis and their sensitivity to material model selection and geometry. It is hypothesized that

linear elastic finite element analysis will overestimate stresses compared to a nonlinear elastoplastic analysis when taper geometry causes significant plastic deformation.

Aim 2. Determine ligament tension patterns using a kinematically-driven finite element knee model simulating patient-specific passive kinematics that discriminate *in vivo* clinical TKR outcomes. It is hypothesized that ligament tension patterns predicted from patient-specific simulations will be significantly different between TKR patients with good and poor functional outcomes.

Aim 3. Determine the effect of TKR alignment on ligament tensions using a validated force-driven passive finite element knee model. It is hypothesized that specific ligaments will increase or decrease in tension during passive motion when TKR component rotational alignment is altered.

Aim 1 addresses technical gaps related to taper junction finite element models assuming linear elastic material properties despite evidence of plastic deformation in explants. Aims 2 & 3 address technical gaps related to the lack of quantification of the relationship between TKR component alignment and ligament tensions when assessed through passive motions during surgery.

List of Studies

Five studies were undertaken to address the three specific aims:

Chapter 2, titled "Comparison of Linear Elastic and Elastoplastic Finite Element Analysis of Bore-Cone Taper Junctions" will address Aim 1 by developing linear elastic and elastoplastic finite element models of a modular taper junction and evaluating the influence of material model selection on the predicted stress environment under *in vivo* loading conditions.

Chapter 3, titled "The Effect of Manufacturing Tolerances on the Mechanical Environment of Taper Junctions in Modular TKR" also will address Aim 1 by applying the elastoplastic taper junction finite element model developed in Chapter 2 to analyze the effect of taper junction geometry on the stress environment and micromotion, and defining the relationship between manufacturing tolerances and mechanical performance.

Chapter 4, titled "Sensitivity of Calculated Ligament Tensions to Intraoperative Knee Kinematics: A Finite Element Computational Study" will address Aim 2 by developing a validated kinematically-driven TKR knee model that inputs patient-specific *in vivo* kinematics and assessing the ability of the model to discriminate TKR functional outcomes based on model predicted ligament tensions during simulated passive range of motion.

Chapter 5, titled "Knee Ligament Tension During Intraoperative Passive Range of Motion Discriminates Functional Outcomes in Patient-Specific Finite Element Models" also will address Aim 2 by applying the kinematically-driven TKR knee model developed in Chapter 4 to perform individual simulations of patient-specific passive range of motion and analyze ligament tension to elucidate the mechanism contributing to poor functional outcome.

Chapter 6, titled "Validation of a Force-Driven TKR Knee Model to Simulate Intraoperative Passive Range of Motion" will address Aim 3 by defining intraoperative loading conditions *in vitro*, validating a force-driven TKR knee model that perturbs TKR component alignment, and quantifying the relationship between component alignment and ligament tension.

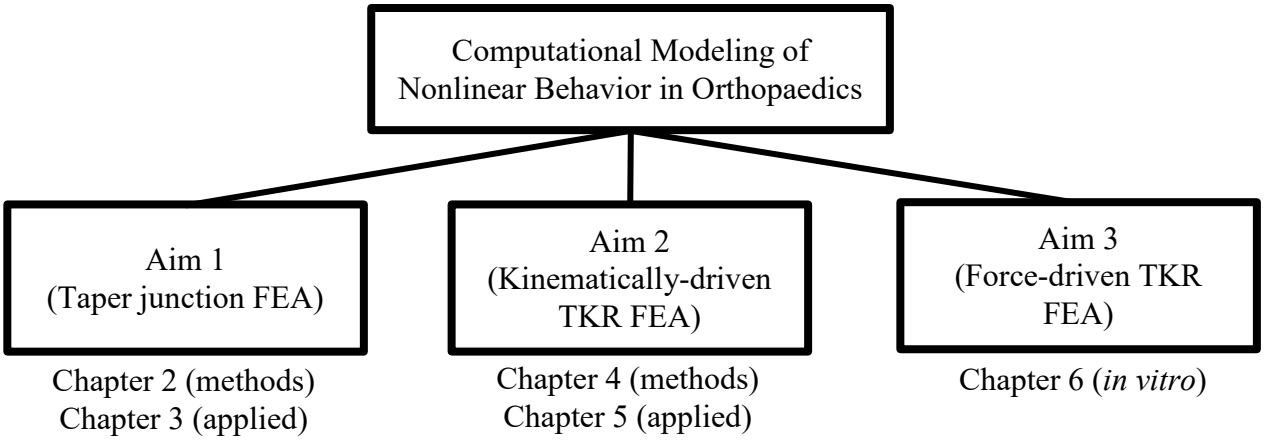

Figure P.1. Organization of dissertation and relationship between each chapter and the specific aims.

CHAPTER ONE

INTRODUCTION

Clinical Significance of Total Knee Replacement

Total knee replacement (TKR) is one of the most common orthopaedic procedures performed in the USA [1] and is projected to exceed 4.3 million by 2030, more than a 600% increase from procedures performed in 2005 [2]. Although TKR surgery has a success rate of 95% at 10 years for most TKR designs, revision surgery still occurs at a rate of approximately one revision for every ten primary TKR surgeries [3], and patient dissatisfaction is even higher [4]. Leading causes of failure include aseptic loosening, knee instability, infection, polyethylene wear, arthrofibrosis (increased knee stiffness) and component malalignment, and vary as a function of time following surgery [5]. Early failure, defined as within five years of surgery, accounts for approximately half of all TKR failures [6]. Although failure beyond 10 years can be inevitable due to mechanical breakdown of available materials (e.g. wear or loosening), prevention of early failure is of great importance due to the cascade of consequential events negatively impacting patient quality of life. Knee instability, arthrofibrosis, and component malalignment alone account for approximately 50% of early revisions [5-7], and are recognized as preventable causes for revision at the time of surgery [5, 8, 9].

A TKR procedure replaces diseased or damaged articular surfaces of the knee with metal and plastic components in order to provide the patient pain relief and improved quality of life. A successful TKR requires both proper resection of bone tissue for optimal

component alignment and proper handling of the soft-tissues surrounding the knee joint, referred to clinically as ligament balance [8]. It is generally accepted that early revision reasons and patient dissatisfaction are related to these surgical factors. During the TKR procedure, surgeons routinely perform assessments on the implanted knee in order to determine if proper TKR component alignment and ligament balance have been achieved. These assessments are based on manual feedback, or the "feel", of the surgeon, and thus highly subjective [10]. The influence of TKR component alignment and ligament balance on the mechanical environment of the knee is poorly understood due to this lack in intraoperative quantitative measures.

In the event of TKR failure, a revision surgery is required where one or all of the primary TKR components are replaced. Revision of an initial revision surgery is more than five times more likely than revision of a primary TKR [11]. Revision surgery further compromises the structural integrity of the knee joint and often require specialized TKR components to replace the primary TKR. Revision TKR components commonly exhibit a modular design that allow additional metal augments or extensions to be assembled onto the TKR components in order to provide surgeons versatility to address patient-specific needs and improve implant fixation [12]. Despite the advantages modular TKR components provide surgeons intraoperatively, the bore-cone taper junctions used to assemble modular components have received significant attention from the orthopaedic community due to evidence of corrosion [13]. The corrosion at these metal taper interfaces occurs from both chemical and mechanical mechanisms. The corrosion by-products, specifically metallic debris, has detrimental consequences on the patient including

osteolysis, aseptic loosening, and a strong lymphatic response, and ultimately limit implant longevity necessitating additional revisions [14].

Computational Modeling to Analyze Orthopaedic Implants

Computational modeling is a numerical approach that uses computer simulation to predict behavior of complex systems. At its foundation, computational modeling is a combination of mathematics, physics, and computer science, and can simulate systems across multiple fields of science including solid mechanics, fluid mechanics, thermodynamics, and biology. Advances in computer science, specifically the increasing computing power of computers, have facilitated the use of computational modeling as an efficient tool for approximating parameters of interest that are either difficult or impossible to measure during physical experiments. Finite element analysis (FEA) represents one of the more common computational modeling approaches used in engineering.

Finite element analysis uses the finite element method (FEM) numerical technique to simulate physical phenomena. Based on the laws of physics and thermodynamics, many physical phenomena related to structural mechanics, fluid behavior, mass transport, and heat flow can be described by mathematical expressions called partial differential equations (PDE). These differential equations relate physical behavior to field variables present in a physical domain, such as a mechanical structure or spatial volume, with respect to time and spatial locations. Field variables depend on the type of problem being solved and can include displacements, stresses and strains, temperature, or mass fluxes among others. Solving PDEs can provide a better understanding of underlying mechanisms that influence these physical behaviors under given conditions and aid engineers to design solutions to

real-world problems. The FEM is a numerical method a computer can utilize to solve PDEs applied to a physical domain provided appropriate boundary conditions. In this numerical approach, the physical domain is divided into smaller, simpler geometric units called finite elements which remain connected together through points, known as nodes, forming a network of elements over the domain called mesh. Subdividing the domain into finite elements make solving the PDEs more manageable. Boundary conditions can be specified as loads or displacements and are required to prevent an indeterminate system and serve to actuate the model simulation. Finite element model simulations that are prescribed displacements are referred to as kinematically-driven and simulations that are prescribed loads as force-driven. The equations that model individual elements are then assembled into a system of equations based on the connections at nodes and boundary conditions in order to solve for field quantities over the entire domain, or as often called the finite element (FE) model. It is important to note that the FEM provides an approximation of the real solution to these PDEs. Therefore, it is important to establish credibility in simulation predictions by proving the equations are being solved correctly, termed verification, and that the physical phenomena is being accurately represented, termed validation.

The FEM was conceptualized as early as the 1940s by Alexander Hrennikoff and Richard Courant. Initial application of FEM was used to analyze structural mechanics in civil and aerospace engineering in the 1950s, and eventually applied to more complex models in biology in the 1970s [15]. Today, FE modeling is commonplace in academia as a research tool for investigating complex systems and in industry as part of product design

workflows across a wide range of engineering disciplines. In the field of bioengineering, medical devices are being innovated that interface directly with the biological systems of the human body. With the aim of improving patient treatments, optimizing device design is difficult to accomplish through experimental testing alone. FEA provides a numerical approach to analyze the function of such devices in these complex biological systems under a variety of different design and environment conditions. Orthopaedics, in particular, has adapted FEA as an effective tool for analyzing the interaction between the musculoskeletal system and total joint replacement devices in order to understand the fundamental mechanics of the bone-implant system and inform future design decisions [16]. FE models ranging in size and complexity have been utilized to analyze how implant fixation affects bone mechanics [17, 18], contact mechanics and wear of articulating implant surfaces [19-21], mechanics of bone-cement-implant interfaces [22, 23], induced soft-tissue loads and the influence of surgical factors on implant performance [24, 25]. Early finite element models of bone-implant systems consisted of idealized two-dimensional geometries [26, 27] while current models are commonly three-dimensional anatomical representations of specific subjects. This increase in geometric complexity parallels growth in computational capacity from hundreds of finite elements in a given model back in the 1980s to hundreds of thousands today. FEA in orthopaedics has also advanced in other aspects including more sophisticated algorithms defining contact at implant interfaces, explicit formulations that allow for dynamic activities to be simulated, and adaptive modeling techniques that allow for model parameters to be updated during simulation. A common misconception is that increasing the complexity of a FE model will yield more accurate predictions.

However, justified simplifications are a trait shared amongst all credible models. Instead, comparison of model predictions from simulations to *in vitro* test data is essential for assessing the predictive capability of the model within its intended scope.

Material Behavior of an Implanted Knee Joint

The implanted knee joint consists of artificial TKR components and biological components. Although a plethora of different TKR designs are available, the overwhelming majority of them consist of a metal component that replaces the end of the femur and a metal tray joined with a plastic polymer insert to replace the end of the tibia. Biological components include the patella, femur and tibia bones, and numerous other soft-tissue structures, mainly ligaments and tendons. Material mechanical behavior is characterized by defining the relationship between an applied force and material deformation, or stress versus strain. Development of a FE implanted knee model requires implementing the material behavior of each of these artificial and biologic materials. Thus, it is important to understand the fundamental behavior of these materials.

Metals generally exhibit high stiffness, high strength, ductility and isotropy due in part to a crystalline microstructure and strong atomic bonds. The stiffness of metals range from 48 GPa to 410 GPa and tensile strength as high as 4100 MPa, orders of magnitude higher than other types of materials [28]. In general, the initial stress-strain mechanical response of metals is linear elastic. Linear refers to a directly proportional relationship between deformation and applied load, and elastic refers to deformations being completely recovered once the applied load is removed. The yield strength defines an approximated limit to this linear elastic behavior in metals, and when subjected to stresses beyond the

yield strength the metal undergoes significant changes in microstructure causing a nonlinear stress-strain response and experiences permanent, or plastic, deformations, until fracture. Another key attribute to the mechanical behavior of metals is ductility which refers to the capacity to undergo deformations without fracturing. From an engineering perspective, these characteristics allow metal parts to endure high loads while still maintaining their shape and most importantly avoid fracture; a perfect combination for a weight-bearing TKR component. Metal alloys commonly used in TKR today include CoCrMo and Ti6Al4V alloys, due to biocompatibility and corrosion resistant properties in addition to the aforementioned mechanical characteristics.

In contrast to the mechanical behavior of metals, plastic polymers exhibit much lower stiffness (7MPa-4 GPa) and strength (~100 MPa) properties but greater ductility (> 1000% elongation) [28]. Additionally, polymers, in general, are highly sensitive to the rate of deformation (strain rate) with respect to time, temperature, and the chemical composition of the environment. The microstructure and increased molecular mass of ultra-high-molecular-weight polyethylene (UHMWPE) contributes to favorable mechanical properties and wear resistance, and the reason it dominates bearing materials used in joint replacements today [29]. UHMWPE is a semicrystalline polymer composed of a crystalline phase and an amorphous phase, and thus, exhibits the combined mechanical characteristics of a solid (from crystalline phase) and a liquid (from amorphous phase), known as viscoelasticity [28]. Important viscoelastic characteristics include creep, an increase in deformation over time under a constant load, and stress relaxation, a decrease in stress within a material under constant deformation, and are by definition rate-dependent

nonlinear behaviors. One aspect of the viscoelastic nature of polymers relevant to function in a TKR is the rate-dependent nonlinear phenomena known as creep, due to frequent scenarios of applied constant load over time (e.g. standing). Additionally, polymers can experience rate-independent nonlinear elastic behavior as polymer chains are stretched, and similar to metals, can exhibit both a linear elastic response prior to reaching the yield strength and rate-independent nonlinear behavior because of plasticity [30]. Also, changes in mechanical properties of polymers, most notably a decrease in ductility towards brittleness, are known to occur due to oxidation in the *in vivo* environment [31].

Biological soft-tissues including ligaments and tendons exhibit nonlinear elastic, anisotropic mechanical behavior that is highly dependent on the complex interactions between collagen fibers, proteoglycans of the ground substance, and high water content that compose them [32]. The tensile strength of soft-tissues comes from the collagen fibers which are optimally arranged to fulfill a specific mechanical function [33]. Soft-tissues exhibit a nonlinear elastic mechanical response to initial loading due to the recruitment of collagen fibers from a crimped to uncrimped state (i.e. the toe-region) beyond which linear behavior exist until failure. Moreover, soft tissues are inherently viscoelastic due to high water content, and thus have a time- and history-dependent material response. Although bone is not intuitively thought of as a "soft" tissue, it too exhibits nonlinear, viscoelastic behavior and is highly anisotropic due to the orderly pattern of hydroxyapatite crystals within the collagen network when forming lamellar osteons (e.g. parallel to the axis of long bones). Most notably, the tensile strength and elastic modulus of bone is directly

proportional to strain rate. Moreover, long bones are stronger in axial compression than tension, and shear strength is about one-third of the compressive strength [30].

Modeling Material Behavior of an Implanted Knee Joint

Computational modeling has been used for decades as a tool for investigating the complex kinematic and biomechanic behavior of the knee joint. As with all computational simulations, the predicted variables from these simulations are heavily influenced by model input parameters and boundary conditions. The most significant model input parameter is material model which defines the mechanical behavior of geometry being represented. Material models available vary significantly in complexity, and require diligence when choosing which material model to implement. For an implanted knee joint, this involves material model selection for both artificial and biologic components.

Metal materials are commonly modeled as linear elastic isotropic and completely neglect any nonlinear behavior that results from plasticity or direction dependent behavior. Since metal implants are usually designed to function well below the yield strength, this representation is appropriate. However, any evidence of post-yield behavior warrants use of a more complex plasticity material model in order to capture material nonlinearity. Linear elastic and plasticity models similar to those used for metals have been implemented to model UHMWPE and other polymers to represent linear and nonlinear behavior. Nevertheless, it is argued that these representations are insufficient due to distinct differences in deformation mechanisms between metals and polymers [34]. More complex material models unique to semicrystalline UHMWPE polymers have been developed that incorporate independent contributions of the amorphous and crystalline phases to account

for the nonlinear elastic and plastic behavior [34, 35]. In TKR studies, such material models are typically only used when the contact mechanics and wear characteristics of the UHMWPE tibial insert are specifically being investigated. The simplest and computationally efficient model representation of implant materials is that of a rigid body which neglects any deformation (elastic or plastic). This representation is only used when an implanted biologic system is being analyzed and deformation of implant components relative to biologic components is deemed negligible.

Material models used for biologic soft-tissues can significantly vary in complexity depending on whether time-dependent behavior is of interest. Viscoelastic material models capture the time-dependent nonlinear behavior and can include individual contributions of the solid phase, fluid phase and ion diffusion, but are only used when the internal mechanics of isolated ligaments are being analyzed such as in sports injury applications. When the time-dependent material response is not of interest, mechanical models used to represent soft tissue behavior focus on the nonlinear response of the solid phase (the collagen fibers, in particular) such as hyperelastic, fiber reinforced, and nonlinear spring models [36]. This approach is very common when analyzing the global biomechanics and kinematic behavior of the knee joint. It is also important to note that, in contrast to implant components, the geometric representation of biologic components are often simplified in the FE model based on the material model used.

Incorporating the physical behavior of materials when developing a FE model requires choosing material models that are appropriate for the specific scope of the analysis. In many instances, a more complex material model may not provide added

benefits to the analysis over a simpler model, yet require substantially more computational time to complete the model simulation. Engineers must constantly assess how detailed a material model needs to be in order to appropriately represent parameters of interest within the system being analyzed while minimizing computational time. Regardless of the complexity, all material models require the incorporation of experimental test data in order to fully define them which can be challenging to obtain, especially for biological materials. The underlying theme is that a variety of different material models can be used to represent artificial and biological components in FEA so long as it is appropriate for the scope of the study and takes into consideration the parameters of interest.

References

[1] American Joint Replacement Registry. 2014 AJRR Annual Report on Hip and Knee Arthroplasty Data. http://www.ajrr.net/images/annual_reports/AJRR_2014_Annual_Report_final_11-11-15.pdf.

[2] Kurtz SM, Lau E, Ong K, Zhao K, Kelly M, Bozic KJ. Future young patient demand for primary and revision joint replacement: National projections from 2010 to 2030. Clinical Orthopaedics and Related Research. 2009, 467:2606–2612.

[3] Kurtz SM, Ong KL, Lau E, Widmer M, Maravic M, Gomez-Barrena E, de Pina M, Manno V, Torre M, Walter WL, de Steiger R, Geesink RGT, Peltola M, Roder C. International survey of primary and revision total knee replacement. International Orthopaedics (SICOT). 2011, 35:1783-1789.

[4] Bourne RB, Chesworth BM, Davis AM, Mahomed NN, Charron KD. Patient satisfaction after total knee arthroplasty: who is satisfied and who is not? Clinical Orthopaedics and Related Research. 2010, 468(1):57-63.

[5] Schroer WC, Berend KR, Lombardi AV, Barnes CL, Bolognesi MP, Berend ME, Ritter MA, Nunley RM. Why are total knees failing today? Etiology of total knee revision in 2010 and 2011. Journal of Arthroplasty. 2013, 28(8 Suppl):116-119.

[6] Le DH, Goodman SB, Maloney WJ, Huddleston JI. Current modes of failure in TKA: Infection, instability, and stiffness predominate. Clinical Orthopaedics and Related Research. 2014, 472:2197-2200.

[7] Dalury DF, Pomeroy DL, Gorab RS, Adams MJ. Why are total knee arthroplasties being revised? Journal of Arthroplasty. 2013, 28(Suppl 1):120-121.

[8] Babazadeh S, Stoney JD, Lim K, Choong FM. The relevance of ligament balancing in total knee arthroplasty: how important is it? A systematic review of the literature. Orthopedic Reviews. 2009, 1:e26.

[9] Fehring TK, Odum S, Griffin WL, Mason JB, Nadaud M. Early failures in total knee arthroplasty. Clinical Orthopaedics and Related Research. 2001, 392:315-18.

[10] Smith T, Elson L, Anderson C, Leone W. How are we addressing ligament balance in TKA? A literature review of revision etiology and technological advancement. Journal of Clinical Orthopaedics and Trauma. 2016, In Press.

[11] Ong KL, Lau E, Suggs J, Kurtz SM, Manley MT. Risk of subsequent revision after primary and revision total joint arthroplasty. Clinical Orthopaedics and Related Research. 2010, 468:3070-3076.

[12] Nadorf J, Gantz S, Kohl K, Kretzer JP. Tibial revision knee arthroplasty: influence of modular stems on implant fixation and bone flexibility in AORI type T2a defects. International Journal of Artificial Organs. 2016,39(10):534-540.

[13] Arnholt, CM, MacDonald D W, Tohfafarosh M, Gilbert JL, Rimnac CM, Kurtz SM, Klein G, Mont MA, Parvizi J, Cates HE, Lee G, Malkani A, Kraay M. Mechanically assisted taper corrosion in modular TKA. Journal of Arthroplasty. 2014, 29 Suppl. 2: 205-208.

[14] Jacobs JJ, Gilbert JL, Urban RM. Current concepts review- corrosion of metal orthopaedic implants. Journal of Bone & Joint Surgery. 1998, 80:268-282.

[15] Henninger HB, Reese SP, Anderson AE, Weiss JA. Validation of computational models in biomechanics. Journal of Engineering in Medicine. 2010, 224(H): 801-812.

[16] Taylor M, Prendergast PJ. Four decades of finite element analysis of orthopaedic devices: where are we now and what are the opportunities? Journal of Biomechanics. 2014, 48(5): 767-778.

[17] Huiskes R, Weinans H, Grootenboer HJ, Dalstra M, Fudala B, Sloof TJ. Adaptive bone remodeling theory applied to prosthetic-design analysis. Journal of Biomechanics. 1987, 20: 1135-1150.

[18] Fernandes PR, Folgado J, Jacobs C, Pellegrini V. A contact model with ingrowth control for bone remodeling around cementless stems. Journal of Biomechanics. 2002, 35(2): 167-176.

[19] Bevill SL, Bevill GR, Penmetsa JR, Petrella AJ, Rullkoetter PJ. Finite element simulation of early creep and wear in total hip arthroplasty. Journal of Biomechanics. 2005, 38(12): 2365-2374.

[20] Netter J, Hermida JC, D'Alessio J, Kester M, D'Lima DD. Effect of polyethylene crosslinking and bearing design on wear of unicompartmental arthroplasty. Journal of Arthroplasty. 2015, 30(8): 1430-1433.

[21] Donaldson, F. E., Coburn, J. C., Lohmann Siegel, K., 2014. Total hip arthroplasty head-neck contact mechanics: A stochastic investigation of key parameters. Journal of Biomechanics 47, 1634-1641

[22] Verdonschot N, Huiskes R. Mechanical effects of stem cement interface characteristics in total hip replacement. Clinical Orthopaedics and Related Research. 1996, 329: 326-336.

[23] Stolk J, Verdonschot N, Critofolini L, Toni A, Huiskes R. Finite element and experimental models of cemented hip joint reconstructions can produce similar bone and cement strains in pre-clincal tests. Journal of Biomechanics. 2002, 35(4): 499-510.

[24] Halloran JP, Petrella AJ, Rullkoetter PJ. Explicit finite element modeling of a total knee replacement mechanics. Journal of Biomechanics. 2005, 38:323-331.

[25] Fitzpatrick CK, Clary CW, Rullkoetter PJ. The role of patient, surgical, and implant design variation in total knee performance. Journal of Biomechanics. 2012, 45:2092-2102.

[26] Huiskes R. The various stress patterns of press-fit, ingrown and cemented femoral stems. Clinical Orthopaedics. 1990, 261: 27-38.

[27] Vasu R, Carter DR, Harris WH. Stress distributions in the acetabular region- I. Before and after total joint replacement. Journal of Biomechanics. 1982, 15(3): 155-164.

[28] Callister WD. Materials science and engineering: an introduction. 2007, 7th edition. Wiley. ISBN: 0471736961.

[29] Bracco P, Bellare A, Bistolfi A, Affatato S. Ultra-high molecular weight polyethylene: influence of the chemical, physical and mechanical properties on the wear behavior. Materials. 2017, 10(7): doi:10.3390/ma10070791.

[30] Mow VC, Hayes WC. Basic orthopaedic biomechanics. 1997, 2nd edition. Lippincott-Raven, Philadelphia, PA. ISBN: 0397516843.

[31] Reinitz SD, Currier BH, Levine RA, Collier JP, Van Critters DW. Oxidation and other property changes of a remelted highly crosslinked UHMWPE in retrieved tibial bearings. Journal of Biomedical Materials Research Part B: Applied Biomaterials. 2017, 105(1): 39-45.

[32] Mow VC, Huiskes R. Basic orthopaedic biomechanics & mechano-biology. 2005, 3rd edition. Lippincott Williams & Wilkins, Philadelphia, PA. ISBN: 0781739330.

[33] Fung YC. Biomechanics: mechanical properties of living tissues. 1993, 2nd edition. Springer-Verlag New York. ISBN: 0387979472.

[34] Rimnac CM, Sobieraj MC. Ultra high molecular weight polyethylene: mechanics, morphology, and clinical behavior. Journal of the Mechanical Behavior of Biomedical Materials. 2009, 2(5): 433-443.

[35] Bergstrom JS, Kurtz SM, Rimnac CM, Edidin AA. Constitutive modeling of ultra-high molecular weight polyethylene under large-deformation and cyclic loading conditions. Biomaterials. 2002, 23: 2329-2343.

[36] Freutel M, Schmidt H, Durselen L, Ignatius A, Galbusera F. Finite element modeling of soft tissues: material models, tissue interaction and challenges. Clinical Biomechanics. 2014, 29: 363-372.

CHAPTER TWO*

COMPARISON OF LINEAR ELASTIC AND ELASTOPLASTIC FINITE ELEMENT ANALYSIS OF BORE-CONE TAPER JUNCTIONS

Introduction

Bore-cone taper junctions, also known as Morse tapers, are a common design feature used in modular joint replacements. The mating bore and cone components are uniformly tapered and provide a self-locking connection upon assembly. Essentially, an interference fit is achieved through localized material deformation and subsequent residual stresses where the cone compresses against the bore walls at a location dependent on the taper fit [1, 2]. Taper surfaces of modular components explanted from patients during revision surgery reveal evidence of such material deformation, visualized as a micro-grooved texture in which the peaks have been flattened or become imprinted onto the walls of the mated bore taper [3-6]. Explanted modular components also reveal evidence of mechanically-assisted corrosion mechanisms, which suggests the taper junctions can experience elevated stresses in concentrated regions and cyclic micromotion [5, 7-12]. The role of localized material deformation on taper junction performance is poorly understood.

The literature analyzes material deformation of the taper junction both globally and locally. *In vitro* testing and retrieval analyses have primarily focused on global

*Results and data provided in this chapter were submitted for publication in: Snethen K, Harman MK, Zhang G. Comparison of linear elastic and elastoplastic finite element analysis of bore-cone taper junctions. Computer Methods in Biomechanics and Biomedical Engineering. Manuscript submitted and in review, 2018.

deformation of the modular implant system as a whole, commonly expressed flexural rigidity, due to the difficulty in measuring mechanics within the bore-cone taper interface [9, 13-15]. Finite element (FE) simulations have allowed for the analysis of local deformations that occur at the contacting bore and cone surfaces [16-19]. These experimental and computational studies analyze taper deformation as an elastic behavior. Conversely, the reported permanent deformations of surface topography [2, 5] have been complemented by microscale submodeling to suggest that localized plastic deformations play a crucial role in the performance of bore-cone taper junctions [20, 21]. Still, macroscale finite element models have assumed elastic behavior through the implementation of linear elastic material properties, despite macroscale finite element simulations also reporting interfacial stresses above material yield strengths [18, 19]. It has been shown that linear elastic material properties can be insufficient in representing the mechanics of medical devices when material nonlinearity exists as would be evident if plastic behavior is present [22]; however, this has not been explored for FE models of modular taper junctions. It is possible that finite element simulations implementing linear elastic material properties are insufficient for predicting stresses within modular taper junctions given that plastic deformation has been shown to occur even at the macroscale [18, 19].

The purpose of this study was to compare predicted residual stresses within modular TKR taper junctions between macroscale FE simulations implementing either linear elastic or elastoplastic material properties to represent implant material behavior. This comparison will be conducted under various taper fit conditions as this is known to

impact the mechanics of the taper junction. It is hypothesized that a linear elastic analysis will over approximate residual stresses when the taper fit produces minimal contact area between the interfacing bore and cone taper surfaces leading to localized plastic deformation.

Methods

The computational approach used in this study required experimental datasets in order to accurately model the modular TKR taper junction. Specifically, model development incorporated experimental data to define material behavior, loading and boundary conditions, and contact behavior.

Development of Linear Elastic and Elastoplastic Material Models

Linear elastic and elastoplastic material behaviors were constructed for both cast CoCrMo (ASTM F75) and wrought Ti6Al4V (ASTM F136) from experimental stress-strain data. The linear elastic material behavior was defined by an elastic modulus (E) and a Poisson's ratio (Table 2.1). The elastoplastic material behavior was developed from yield strength (YS), ultimate tensile strength (UTS), and percent elongation values collected from the literature pertaining to these specific materials. Selection criterion for the inclusion of experimental material data in developing the elastoplastic models required tensile testing of the alloys with intent for medical device application and reported YS, UTS, percent elongation and alloy chemical composition be in agreement with each material specific ASTM standard. Since many experimental studies only list handbook values for measured material properties and not full stress-strain curves, a power law was

implemented to approximate the nonlinear post-yield region of the stress-strain curves using the values reported in the literature sources, and was defined as

$$\sigma = K\varepsilon^{n}$$

where σ is the stress, ε is the strain, K is the strength coefficient, and n is the strain hardening coefficient [23].

Table 2.1. Material property parameters assigned to the linear elastic and elastoplastic material behaviors for each material.

Material	Cast CoCrMo	Wrought/Forged Ti6Al4V
Model Component	Baseplate with Cone Taper	Stem with Bore Taper
Standard	ASTM F75	ASTM F136
Elastic Modulus [GPa]	210	110
Poisson's Ratio	0.3	0.31
Yield Strength [MPa]	515*	990*
% Elongation	12*	13*
n	0.1162	0.0416
K	1015.7	1200.4
Published Sources	[24-33]	[24, 34, 35]

*Based on average values from the published source data

For each experimental dataset, the yield strain was calculated from the elastic modulus and reported yield stress, and defined the linear region of the stress-strain behavior. Additionally, the UTS was assumed to occur at the failure elongation; an assumption justified by the failure behavior of these specific alloys evident in the stress-strain curves collected. This provided two pairs of data points that could then be compared to the power law approximation. The strength coefficient, K, and the strain hardening component, n, were assigned initial values and the squared difference at the two aforementioned stress-strain data points was calculated. Coefficients K and n were then optimized in order to minimize the sum of the squared differences, and approximate the unknown post-yield region of the stress-strain curve. This routine was shown to have a RMSE of 8.9, 20.6, 41.4, and 16.3 MPa when performed on known full stress-stress curves of wrought Ti6Al4V, wrought/forged CoCrMo, as-cast CoCrMo, and cast CoCrMo processed with hot isostatic pressing (HIP), respectively (Figure 2.1).

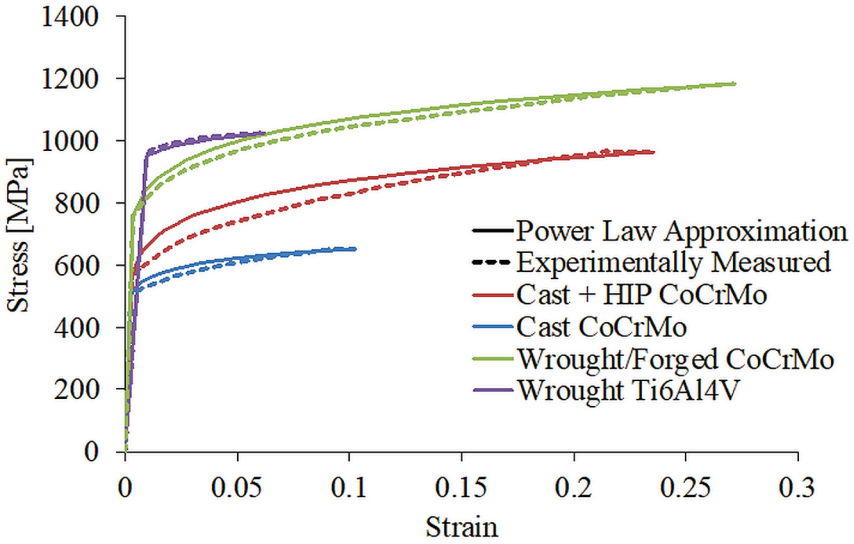

Figure 2.1. Power law approximations of experimental full stress-strain curves for two cast CoCrMo alloys, a wrought Ti6Al4V alloy, and a wrought/forged CoCrMo alloy.

Once the stress-strain curve was approximated for each experimental dataset, the same optimization routine was repeated to fit a curve to represent the overall material subset (e.g. cast CoCrMo) by minimizing the sum of squares between the fit curve and each approximated stress-strain curve simultaneously (Figure 2.2). The linear sub-yield region of the elastoplastic curve was defined using the average yield strength of the reported values from each material subset and the elastic modulus from the corresponding linear elastic material behavior (Table 2.1). The approximated stress-strain data was converted to true stress and true strain for implementation in the FE model. All materials were assumed to behave isotropically.

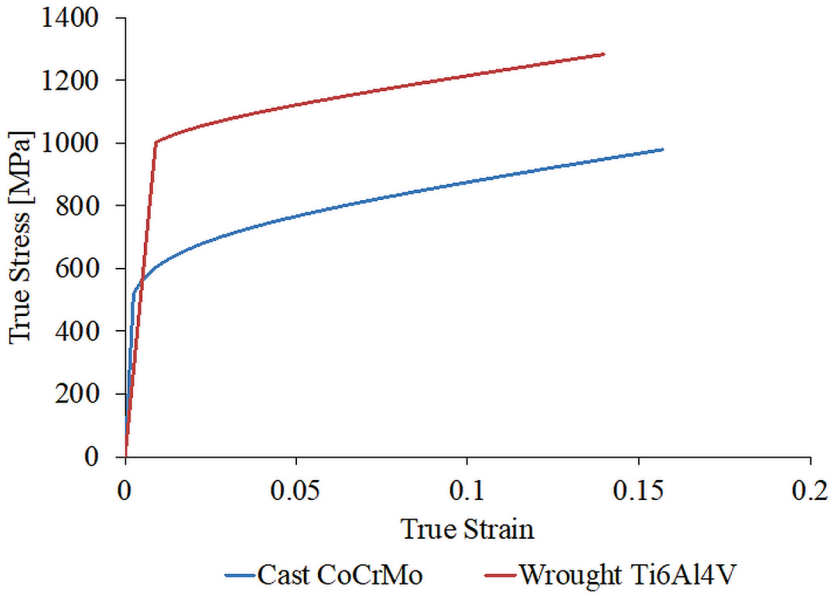

Figure 2.2. True stress-strain curves implemented in the finite element analysis to model elastoplastic behavior for each represented material.

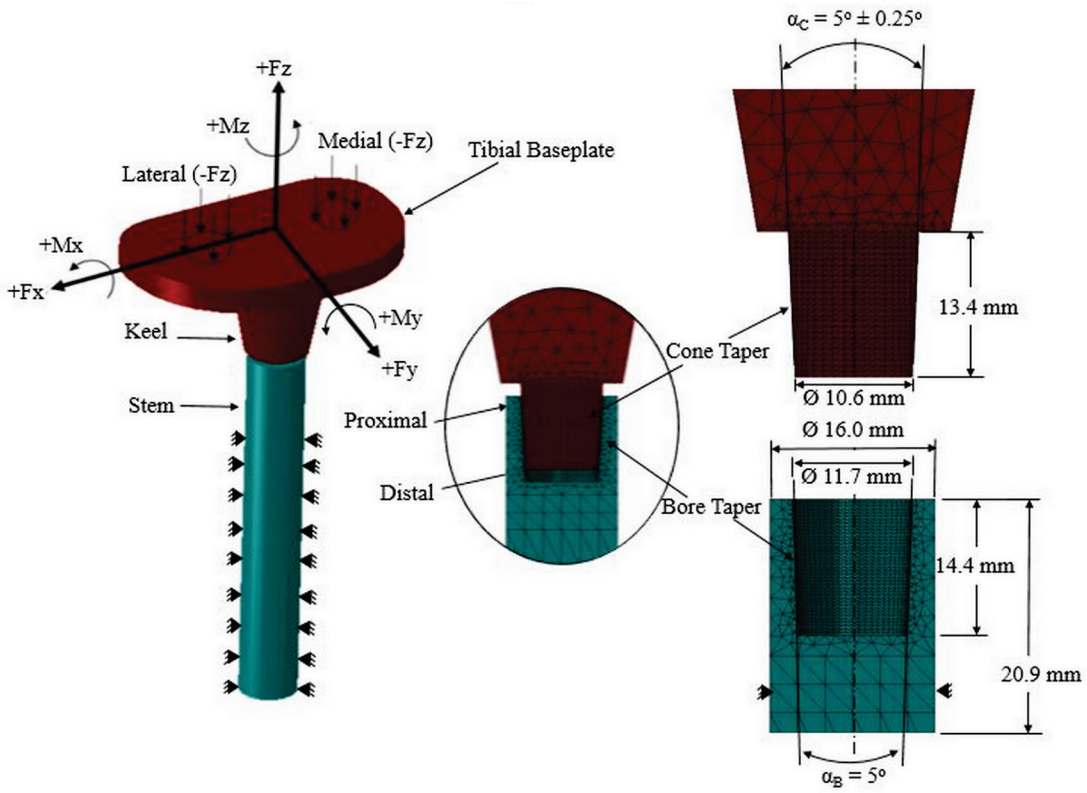

Figure 2.3. Schematic of the modeled 3D modular TKR with applied loading orientations. Exploded cross-section annotates dimensions used to create the model and demonstrates the localized mesh at the bore-cone taper interface. Location on stem from which fixed constraints were applied along its length in the finite element simulations is shown. α_B: Bore Taper Angle, α_C: Cone Taper Angle.

Development of Taper Junction Finite Element Model

The linear elastic and elastoplastic material models were applied to a three-dimensional finite element (FE) model of a modular long-stem tibial TKR component. A generalized bore-cone taper junction geometry was created in design software (Solidworks 2014, Dassault Systemes, Waltham, MA) using measurements from retrieved modular long-stem tibial TKR components. The geometric reconstruction included a tibial baseplate having a cone taper located on the distal end of the keel and a stem component

having a bore taper located on its proximal end (Figure 2.3). The taper junction was initially designed with a 5° taper angle on both the bore taper (α_B) and cone taper (α_C) (Figure 2.3). Thus, the initial geometry exhibited an angle mismatch, defined as the bore angle minus the cone angle, of 0° which represents a perfect fit and can only be idealized due to inherent manufacturing tolerances.

To account for this manufacturing tolerance, two additional taper junction geometries were developed with an angle mismatch of ±0.25° by only perturbing the angle of the cone taper. This generated three distinct taper fit scenarios: perfect fit, positive fit, and negative fit. The positive fit scenario is defined as the bore taper angle being 0.25° greater than the cone taper angle, also referred to as a positive mismatch. The negative fit scenario is defined as the bore taper angle being 0.25° smaller than the cone taper angle, or a negative mismatch. In this study, the cone taper angle dimension was 4.75° for positive mismatch and 5.25° for negative mismatch. The angle mismatch defining the positive and negative taper fit scenarios were chosen based on extreme values found in the literature for taper junctions of modular orthopaedic devices [14]. All other geometric dimensions remained constant. The three-dimensional geometric models were subsequently imported into ABAQUS (v6.14, Dassault Systemes, Waltham, MA) to perform the deterministic FE analysis (Figure 2.3). Material properties of cast CoCrMo (ASTM F75) were assigned to the cone taper and material properties of wrought Ti6Al4V (ASTM F136) were assigned to the bore taper. Taper junction material combination will be specified as bore material-cone material.

The FE model consisted of 52950 tetrahedral elements, including a locally refined mesh of 34669 elements at the taper junction. For computational efficiency, quadratic tetrahedral elements with improved surface stress visualization (C3D10I) were used in the regions of taper contact [36], and linear tetrahedral elements (C3D4) were used outside this region of interest. The mesh density was justified through completion of a convergence analysis where maximum stress in the taper junction and total strain energy were converged to within 5% for all three of the taper fits modeled using elastoplastic material properties.

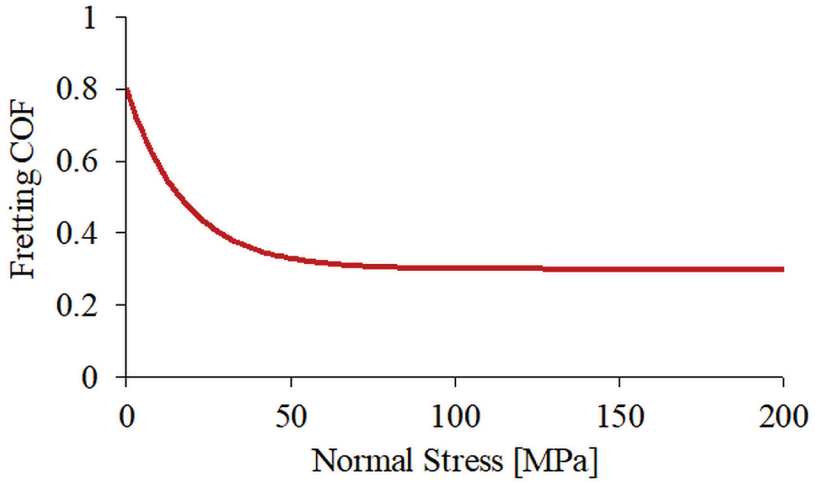

Figure 2.4. Fretting coefficient of friction (COF) and normal stress relationship implemented in FE model contact for the Ti6Al4V-CoCrMo bore-cone material combination.

Contact at the bore-cone taper junction was modeled using a surface-to-surface finite sliding contact formulation. The contact was defined using contact pairs with the cone taper assigned the master surface and the bore taper the slave surface, and enforced using the penalty method. The coefficient of friction (COF) at the taper interface was

defined as a function of the contact pressure. An exponential decay model [38] was used to fit experimental fretting COF versus normal stress data for a Ti6Al4V-CoCrMo material combination [39] and represented by

$$\mu = \mu_0 + (\mu_0 - \mu_\infty)e^{-d_c P}$$

where P is the contact pressure, μ_o is the coefficient of friction at zero contact pressure, μ_∞ is the coefficient of friction at increasing contact pressure, and d_c is the decay factor. The coefficient of friction parameters were defined μ_o=0.8 and μ_∞ =0.3, and the decay factor, d_c, was optimized to a value of 0.056 in order to match the experimental test data (Figure 2.4).

Model Loading and Boundary Conditions

A dynamic, implicit simulation was completed in two steps: (1) a prescribed axial assembly load to seat the cone taper into the bore taper; and (2) a prescribed load profile of two gait cycles. In the first step, a 4400 N assembly load, measured to be the average impaction force applied by orthopaedic surgeons [39], was applied to a node on the inferior surface of the stem in alignment with the stem central axis and a fixed constraint was enforced on the superior surface of the tibial baseplate. The gait loading cycle applied in the second step was defined from published telemetric data and included axial loads (Fz), flexion-extension (Mx) moments, and external-internal (Mz) moments (Figure 2.5) [40]. The resultant compressive force (-Fz) was split 55% medial-45% lateral [41] and distributed in a circular pattern about 4 nodes in approximated medial and lateral regions on the superior surface of the tibial baseplate generating a resultant abduction-adduction moment (My) in the frontal plane. Corresponding flexion-extension (Mx) and external-

internal moment (Mz) profiles were directly applied about the medial-lateral and superior-inferior axes (Figure 2.3), respectively, via a reference node coupled to the superior surface of the baseplate. A 940 N body weight, representing the average patient weight of the subjects who participated in the telemetric study [40], was used to calculate the magnitudes of the loads and moments. Only two gait loading cycles were simulated after a preliminary analysis consisting of five gait cycles revealed that the taper junction stabilized with changes in micromotion <1 μm and stress <5 MPa after two cycles. During the gait loading cycles, boundary conditions were representative of a worst-case scenario of distal stem fixation without support of the proximal tibial bone (Figure 2.3), a common physiological condition in TKR revision surgeries that often necessitates use of a modular long-stem tibial component [42].

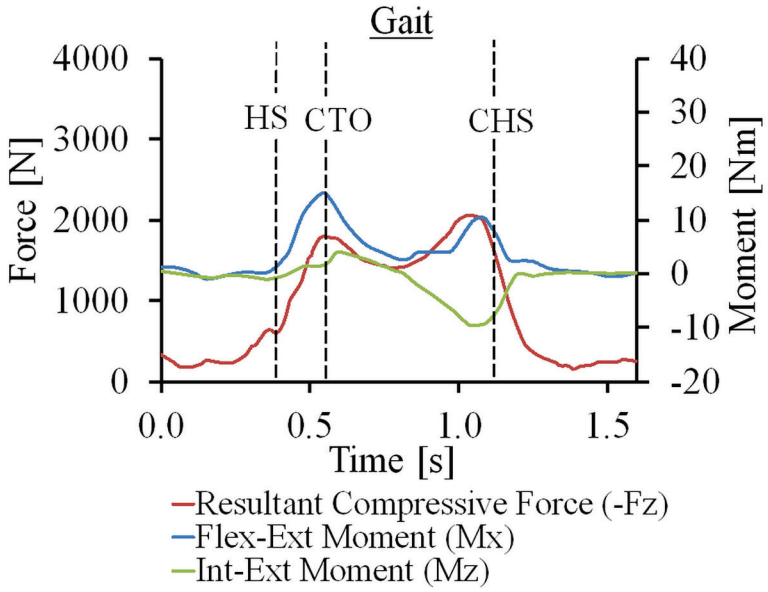

Figure 2.5. Gait activity loading cycles applied in the dynamic finite element simulation with respect to the corresponding axes. HS = heel strike; CHS = contralateral heel strike; CTO = contralateral toe off.

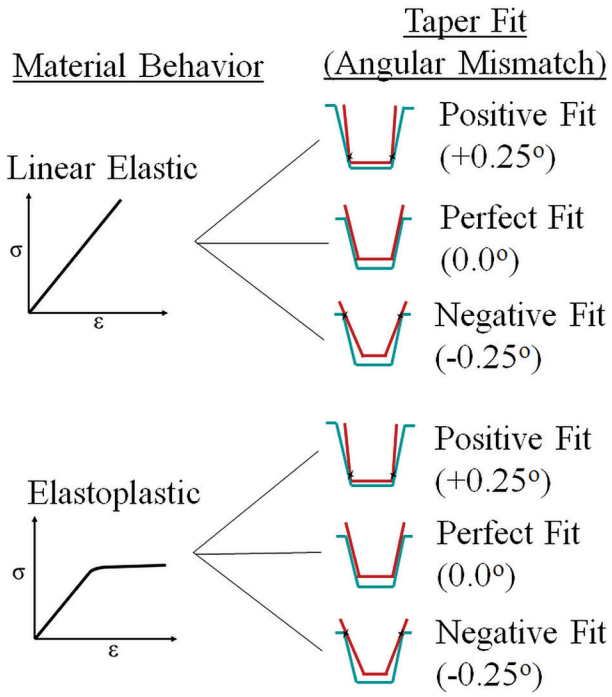

Figure 2.6. Experimental design to compare residual stresses of taper junctions for linear elastic and elastoplastic FE analysis for three distinct taper fit scenarios.

Experimental Design of Study

A total of six FE simulations were run in order to compare the residual stresses within the taper junction between linear elastic and elastoplastic analyses under three different taper fit scenarios (Figure 2.6). To compare the stresses in the taper junction across all analyses, von Mises stress, σ, defined as

$$\sigma = \sqrt{\frac{3}{2} S_{ij} S_{ij}}$$

where S_{ij} is the deviatoric stress tensor, was chosen due to a triaxial stress environment within the taper junction as well as the general use of the von Mises yield criterion in engineering design of isotropic ductile metals. The von Mises stresses were recorded for

both the bore and cone tapers at the end of the assembly step, gait cycle 1, and gait cycle 2. These stresses represent residual stresses since they were recorded at the end of the loading cycles when the applied load was minimal (~200 N compared to 2000 N peak load) and the taper junction had reached a state of equilibrium. Additionally, plastic strain will be reported to analyze the extent of plastic deformation.

Results

Trends in stress distributions were similar between linear elastic and elastoplastic analyses. The stress distribution was determined by the taper fit between the bore and cone taper geometries regardless of the material model used (Figure 2.7). The perfect fit condition resulted in a uniform stress distribution, while positive and negative fits led to distal and proximal stress concentrations within the taper junction, respectively (Figure 2.7). Furthermore, the maximum residual stress within the taper junction was located on the cone taper in positive fit scenarios and on the bore taper in negative fit scenarios; hence, the maximum residual stresses reported are from these respective locations for these taper fit scenarios.

Differences in predicted stress in the linear elastic and elastoplastic analyses were only present in the positive fit scenario because it was the only taper fit scenario that produced stresses above the yield limit, and thus nonlinear material behavior. The post-yield stresses only existed in the lower strength cast CoCrMo cone taper characterized by a yield strength (515MPa) approximately half that of the bore taper (990MPa). In the positive fit condition, the final maximum residual stress calculated was 691MPa in the linear elastic model and 538.8MPa in the elastoplastic model, a 24.8% difference in stress

between the two analyses (Figure 2.8). The perfect fit and negative fit conditions resulted in identical final maximum residual stresses in both the linear elastic and elastoplastic analyses (Figure 2.8). This 0% difference in predicted stress between the linear elastic and elastoplastic analyses can be explained by the absence of post-yield stresses in the perfect and negative fit conditions.

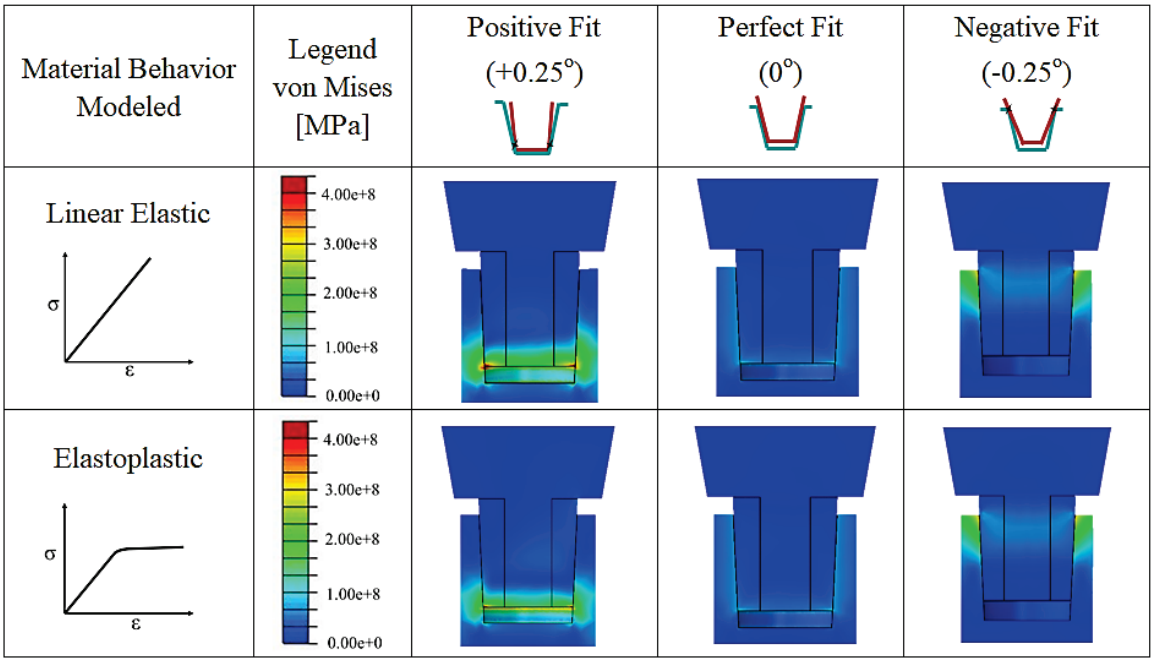

Figure 2.7. Von Mises stress distributions at the bore-cone taper interface for the linear elastic and elastoplastic model simulations for all taper fits simulated.

Focusing on the positive fit condition, the maximum residual stress varied throughout the simulation steps, but changes in percent difference between linear elastic and elastoplastic analyses were insignificant. The greatest percent difference in residual stress was 26.7% for the cone taper and 3.4% for the bore taper. These percent differences between the two analyses varied less than 2.1% across the whole simulation.

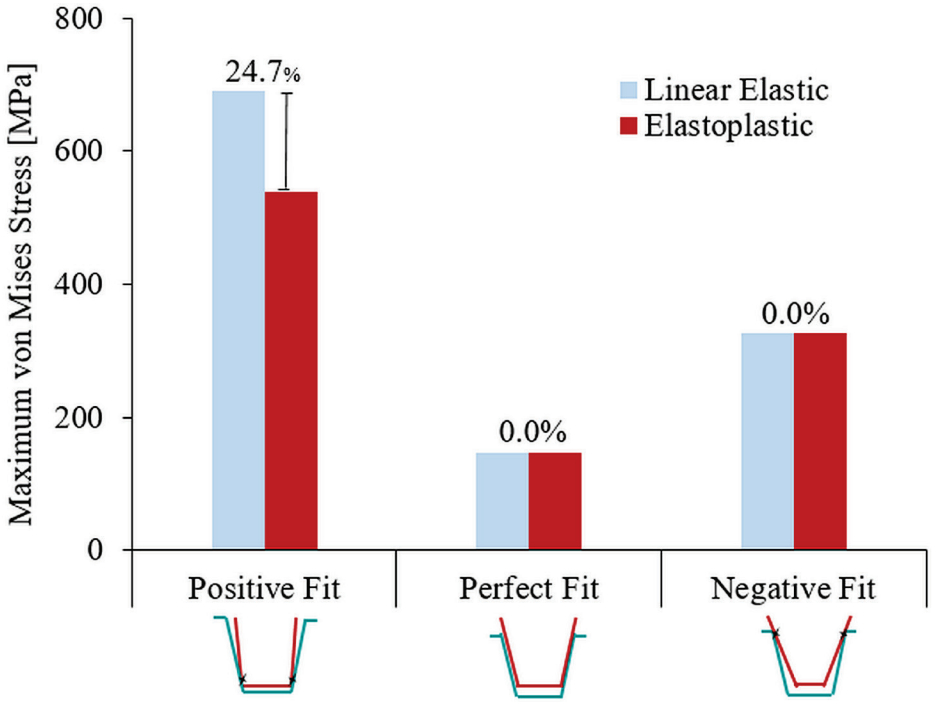

Figure 2.8. Percent difference between von Mises stress values for linear elastic and elastoplastic simulation for each taper fit simulated.

The residual stresses were greatest following taper junction assembly, and decreased in the cone taper and to a greater extent in the bore taper during the subsequent gait loading cycles. In the linear elastic analysis, residual stress decreased from 710 MPa to 690 MPa in the cone taper and from 483 MPa to 374 MPa in the bore taper (Figure 2.9). In the elastoplastic analysis, residual stress decreased from 542 MPa to 539 MPa in the cone taper and from 470 MPa to362 MPa in the bore taper (Figure 2.9). The majority of the plastic deformation experienced in the taper junction was accumulated during the assembly step. Principal plastic strain was calculated to be 1.71E-03 after assembly and increased to 2.05E-03 and 2.10E-3 after the first and second gait cycles, respectively.

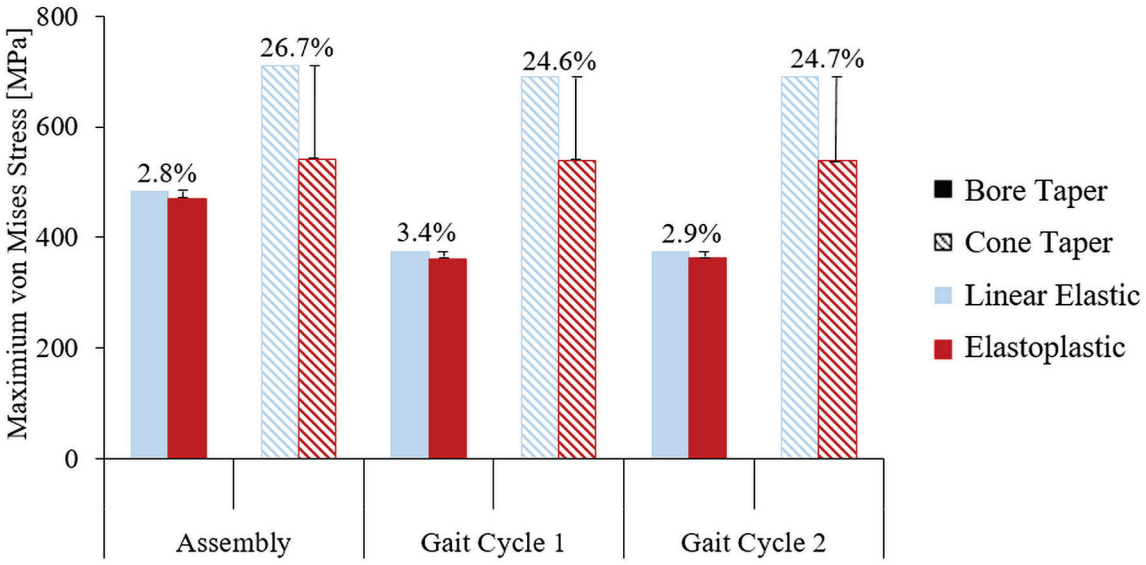

Figure 2.9. Progression and comparison of maximum von Mises stress in the bore taper and maximum stress in the cone taper between linear elastic and elastoplastic models throughout the simulation steps for the positive taper fit scenario. Percent difference calculations are displayed above the bar graphs.

Discussion

This study demonstrated that a linear elastic FE analysis of modular TKR taper junctions will overestimate stresses in comparison to an elastoplastic analysis for a common taper fit scenario. When the taper junction exhibits a positive fit where contact occurs at the leading edge of the cone taper, post-yield stresses and plastic deformations are experienced leading to a divergence in residual stress predictions between linear elastic and elastoplastic analyses. In modular total hip replacements, the positive fit has been suggested to be advantageous over the negative fit due to a decrease in moment arm between the point of contact and resultant load as well as the allowance of fluid ingress [13]. Furthermore, the previous design standard for bore-cone taper junctions in modular

femoral heads specified nominal positive fits for all bore-cone taper pairings [43]. Hence, the positive fit condition shown to undergo plastic behavior is of great relevance.

The distinct stress distributions evident in the linear elastic and elastoplastic analysis results (Figure 2.7) were attributed to the unique contact environment generated by a given taper fit. In a positive fit condition, where the bore angle is larger than the cone angle, the cone is able to penetrate into the bore until the distal tip contacts the internal bore taper surface. On the contrary, the smaller bore angle present in the negative fit condition limits the penetration of the cone taper due to interference at the proximal region of the taper junction. This produced elevated stress on the cone taper for the positive fit scenario and on the bore taper for the negative fit. The simulations only surpassed the yield strength in the positive fit condition since the cone taper was modeled with the much weaker cast CoCrMo (yield strength 515 MPa) when compared to the wrought/forged Ti6Al4V alloy (yield strength 990 MPa) applied to the bore taper; hence, there was no plastic strain present in the perfect fit or negative fit scenarios. This explains why there were no differences in residual stress seen between the linear elastic and elastoplastic analyses for the perfect fit or negative fit conditions (Figure 2.9) because the elastoplastic material behavior remained within the linear region of the stress-strain curve matching that of the linear elastic material.

The yield strength of the cone taper was exceeded in the positive fit condition. This post-yield stress occurred in the assembly step where the impaction of an intraoperative hammer blow was simulated (Figure 2.9). Due to the immediate decrease in stiffness of metal alloys upon reaching the yield stress, the maximum residual stress was much higher

in the linear elastic material compared to the elastoplastic material which incorporates this stiffness decrease. This over-approximation of stress (25% difference) may be acceptable when conservative estimates are desired. However, depending on the material being modeled, the analysis may produce unrealistic results. In this study, the linear elastic Ti6Al4V-CoCrMo taper junction produced a maximum residual stress approximately 91% of the UTS for the generalized cast CoCrMo material while the same simulation with elastoplastic material behavior produced a maximum stress only 70% of the UTS. Although not directly reported, it can be assumed that the peak stresses endured during taper junction assembly exceeded the UTS in the linear elastic model considering a residual stress 91% UTS was calculated after the 4400 N load was removed. This would cause material failure which is not a clinically reported occurrence at the macroscale.

The presence of cyclic loading during *in vivo* conditions further emphasized the distinctions between the linear elastic and elastoplastic analyses. When a metal material is loaded and then unloaded its stress-strain behavior follows a straight-line path from the point of unloading that parallels that of the elastic modulus. For stresses below the elastic limit (i.e. the yield strength) this unloading path matches the initial linear region of the material; however, if stress has surpassed the yield strength, the unloading path will now be offset from the linear region. The loading-unloading path matched the linear region in the linear elastic analysis despite post-yield stresses generated in the assembly step because material behavior was defined by a single stiffness value. Since the elastoplastic analysis accounts for the nonlinear stress-strain behavior that occurs beyond the elastic limit, the loading-unloading path was offset from the linear region during the assembly step. This

initial offset in loading-unloading paths between the two material models resulted in nearly constant (less than 2% variation) percent differences in stress throughout the gait cycles following assembly (Figure 2.9).

Furthermore, once a metal experiences stresses beyond its elastic limit, it enters into a plastic region and becomes more difficult to deform under additional loading, a phenomenon known as strain hardening. The greater change in residual stress following the assembly step for the linear elastic analysis compared to the elastoplastic analysis could be attributed to the absence of strain hardening behavior in the linear elastic material model. The elastoplastic analyses calculated relatively constant stresses in the cone taper beyond assembly and negligible change in plastic strain as expected given applied loading was significantly less in the subsequent gait cycles. The strain hardening behavior is difficult to discern in this analysis since residual stress in the linear elastic analysis decreased after assembly due to lower loading cycles, but these observations suggest the strain hardening behavior helps stabilize the stress environment of the taper junction. All of the trends discussed are expected to be further emphasized if higher loads were applied such as an above-average assembly force or more demanding physical activity.

This study is limited by its use of generalized material models and a generalized taper junction geometry. Use of the generalized material model was intended to represent material properties corresponding to relevant ASTM standards and to capture industry practices without limiting the analysis to a specific material processing technique. Use of a generalized taper junction geometry was intended to represent key taper dimensions with a focus on varying the taper angle to create three distinct taper fit scenarios. Taper angle

was focused on since angle mismatch has been strongly correlated with surface stresses [17], and it was expected perturbing this parameter would produce unique stress conditions to compare linear elastic and elastoplastic analyses.

Conclusion

In summary, linear elastic and elastoplastic FE analyses of the modular TKR taper junction calculated different stress magnitudes when the taper geometry represented a positive mismatch condition. In the positive mismatch condition, the stress concentrated on the cone taper and induced post-yield stresses in the lower strength cast CoCrMo material leading to an overestimation in stress in the linear elastic analysis compared to the elastoplastic analysis. The linear elastic and elastoplastic analyses calculated identical stresses for the perfect fit and negative fit scenarios since the yield strength was not surpassed in the bore or cone taper. Nonetheless, given the industry bias towards positive mismatch in modular taper junctions, it is recommended that an elastoplastic material model be used in FE analysis of taper junctions in order to generate realistic approximations of interfacial stresses. The elastoplastic model would be beneficial in design phase analyses where material optimization is desired or when attempting to recreate *in vitro* testing. If a linear elastic model is used, the user should be aware of post-yield behavior and cautiously report results if the yield strength of the material being modeled is exceeded.

References

[1] Hernigou P, Queinnec S, Flouzat Lachaniette CH. One hundred and fifty years of history of the Morse taper: from Stephen A. Morse in 1864 to complications related to modularity in hip arthroplasty. International Orthopaedics. 2013, 37: 2081-2088.

[2] Witt F, Guhrs J, Morlock MM, Bishop NE. Quantification of the contact area at the head-stem taper interface of modular hip prostheses. Plos One. 2015, 10(8): 1-15.

[3] Arnholt CM, MacDonald DW, Malkani AL, Klein GR, Rimnac CM, Kurtz SM, Implant Research Center Writing Committee, Kocagoz SB, Gilbert JL. Corrosion damage and wear mechanisms in long-term retrieved CoCr femoral components for total knee arthroplasty. Journal of Arthroplasty. 2016, 31(12): 2900-2906.

[4] Harman MK, Baleani M, Juda K, Viceconti M. Repeatable procedure for evaluating taper damage on femoral stems with modular necks. Journal of Biomedical Materials Research Part B. 2011, 99B: 431-439.

[5] Pourzal R, Hall DJ, Ha HQ, Urban RM, Levine BR, Jacobs JJ, Lundberg HJ. Does surface topography play a role in taper damage in head-neck modular junctions? Clinical Orthopaedics and Related Research. 2016, 474: 2232-2242.

[6] Van Citters DW, Martin AJ, Currier JH, Park S-H, Edidin AA, "Factors Related to Imprinting Corrosion in Modular Head-Neck Junctions," Modularity and Tapers in Total Joint Replacement Devices, ASTM STP1591, A. S. Greenwald, S. M. Kurtz, J. E. Lemons, and W. M. Mihalko, Eds., ASTM International, West Conshohocken, PA 2015: 83–98, doi:10.1520/STP159120140138.

[7] Porter DA, Urban RM, Jacobs JJ, Gilbert JL, Rodriguez JA, Cooper HJ. Modern trunnions are more flexible: a mechanical analysis of THA taper designs. Clinical Orthopaedics and Related Research. 2014, 472: 3963-3970.

[8] Arnholt CM, MacDonald DW, Tohfafarosh M, Gilbert J, Rimnac CM, Kurtz SM, Implant Research Center Writing Committee. Mechanically assisted taper corrosion in modular TKA. Journal of Arthroplasty. 2014, 29 (Suppl. 2): 205-208.

[9] Grupp TM, Weik T, Bloemer W, Knaebel HP. Modular titanium alloy neck adapter failures in hip replacement- failure mode analysis and influence of implant material. BMC Musculoskeletal Disorders. 2010, 11:3.

[10] Langton DJ, Sidaginamale R, Lord JK, Nargol AVF, Joyce TJ. Taper junction failure in large-diameter metal-on-metal bearings. Bone & Joint Research. 2012, 1: 56-63.

[11] Goldberg JR, Gilbert JL, Jacobs JJ, Bauer TW, Paprosky W, Leurgans S. A multicenter retrieval study of taper interfaces of modular hip prostheses. Clinical Orthopaedics and Related Research, 2002, 401: 149-161.

[12] Lieberman JR, Rimnac CM, Garvin KL, Klein RW, Salvati EA. An analysis of the head-neck taper interface in retrieved hip prostheses. Clinical Orthopaedics and Related Research. 1994, 300: 162-167.

[13] Jani SC, Sauer WL, McLean TW, Lambert RD, Kovacs P. Fretting corrosion mechanisms at modular implant interfaces. American Society for Testing and Materials ASTM STP 1301. 1997.

[14] Goldberg JR., Gilbert JL. *In vitro* corrosion testing of modular hip tapers. Journal of Biomedical Material Research Part B: Applied Biomaterials. 2003, 64: 78-93.

[15] Jauch SY, Huber G, Haschke H, Sellenschloh K, Morlock MM. Design parameters and the material coupling are decisive for the micromotion magnitude at the stem-neck interface of bi-modular hip implants. Medical Engineering & Physics. 2014, 36: 300-307.

[16] Shareef N, Levine D. Effect of manufacturing tolerances on the micromotion at the Morse taper interface in modular hip implants using the finite element technique. Biomaterials. 1996, 17: 623-630.

[17] Donaldson FE, Coburn JC, Lohmann Siegel K. Total hip arthroplasty head-neck contact mechanics: A stochastic investigation of key parameters. Journal of Biomechanics. 2014, 47: 1634-1641.

[18] Chu Y, Elias JJ, Duda GN, Frassica FJ, Chao EYS. Stress and micromotion in the taper lock joint of a modular segmental bone replacement prosthesis. Journal of Biomechanics. 2000, 33: 1175-1179.

[19] Lanting BA, Teeter MG, Vasarhelyi EM, Ivanov TG, Howard JL, Naudie DDR. Correlation of corrosion and biomechanics in the retrieval of a single modular neck total hip arthroplasty design: modular neck total hip arthroplasty system. Journal of Arthroplasty. 2015, 30: 135-140.

[20] Zhang T, Harrison NM, McDonnell PF, McHugh PE, Leen SB. Micro-macro wear-fatigue of modular hip implant taper-lock coupling. Journal of Strain Analysis. 2013, 0(0): 1-17.

[21] Lundberg HJ, Ha NQ, Hall DJ, Urban RM, Levine BR, Pourzal R. Contact mechanics and plastic deformation at the local surface topography level after assembly of

modular head-neck junctions in modern total hip replacement devices. Modularity and Tapers in Total Joint Replacement Devices. 2015, ASTM STP1591: 59-82.

[22] Zhang G. Geometric and material nonlinearity in tensioned wires of an external fixator. Clinical Biomechanics. 2004, 19:513-518.

[23] Hosford WF. Power Law Approximation. In: Mechanical Behavior of Materials. Cambridge University Press, NY. 2010: 67-68.

[24] ASM Materials for Medical Devices Database Committee, 2009. Materials and Coatings for Medical Devices: Cardiovascular. ASM International, Materials Park, Ohio.

[25] Berlin RM, Gustavson LJ, Wang KK. Influence of post processing on the mechanical properties of investment cast and wrought Co-Cr-Mo alloys. Cobalt-Base Alloys for Biomedical Applications. 1999, ASTM STP 1365: 62-70.

[26] Berry G, Bolton JD, Brown JB, McQuaide S. The production and properties of wrought high carbon Co-Cr-Mo alloys. Cobalt-Base Alloys for Biomedical Applications. 1999, ASTM STP 1365: 11-31.

[27] Cohen J, Rose RM, Wulff J. Recommended heat treatment and alloy additions for Cast Co-Cr surgical implants. Journal of Biomedical Materials Research. 1978, 12(6): 935-937.

[28] Devine TM, Wulff J. Cast vs. wrought cobalt-chromium surgical implant alloys. Journal of Biomedical Materials Research. 1975, 9 (2): 151-167.

[29] Dobbs HS, Robertson JLM. Heat treatment of cast Co-Cr-Mo for orthopaedic implant use. Journal of Materials Science. 1983, 18: 391-401.

[30] Hodge FG, Lee TS. Effects of processing on performance of cast prosthesis alloys. Corrosion. 1975, 31(3): 111-114.

[31] Hollander R, Wulff J. New technology for mechanical property improvement of cast Co-Cr-Mo-C surgical implants. Engineering in Medicine. 1974, 3(4): 8-9.

[32] Mishra AK, Hamby MA, Kaiser WB. Metallurgy, microstructure, chemistry and mechanical properties of a new grade of cobalt-chromium alloy before and after porous-coating. Cobalt-Base Alloys for Biomedical Applications. 1999, ASTM STP 1365: 71-88.

[33] Spires WP, Kelman DC, Pafford JA. Mechanical evaluation of ASTM F75 alloy in various metallurgical conditions. Quantitative Characterization and Performance of Porous Implants for Hard Tissue Applications. 1987, ASTM STP 953: 47-59.

[34] Murr LE, Esquivel EV, Quinones SA, Gayton SM, Lopez MI, Martinez EY, Medina F, Hernandez DH, Martinez E, Martinez JL, Stafford SW, Brown DK, Hoppe T, Meyers W, Lindhe U, Wicker RB. Microstructures and mechanical properties of electron beam-rapid manufactured Ti-6Al-4V biomedical prototypes compared to wrought Ti-6Al-4V. Materials Characterization. 2009, 60: 96-105.

[35] Ploeg HL, Burgi M, Wyss UP. Hip stem fatigue test prediction. International Journal of Fatigue. 2009, 31(5): 894-905.

[36] Tadepalli SC, Erdemir A, Cavanagh PR. Comparison of hexahedral and tetrahedral elements in finite element analysis of foot and footwear. Journal of Biomechanics. 2011, 44: 2337-2343.

[37] Oden JT, Martins JAC. Models and computational methods for dynamic friction phenomena. Computer Methods in Applied Mechanics and Engineering. 1985, 52: 527-634.

[38] Swaminathan V, Gilbert JL. Fretting corrosion of CoCrMo and Ti6Al4V interfaces. Biomaterials. 2012, 33(22): 5487-5503.

[39] Heiney JP, Battula S, Vrabec GA, Parikh A, Blice R, Schoenfeld AJ, Njus GO. Impact magnitudes applied by surgeons and their importance when applying the femoral head onto the Morse taper for total hip arthroplasty. Archives of Orthopaedic and Trauma Surgery. 2009, 129: 793-796.

[40] Kutzner I, Henlein B, Graichen F, Bender A, Rohlmann A, Halder A, Beier A, Bergmann G. Loading of the knee joint during activities of daily living measured *in vivo* in five subjects. Journal of Biomechanics. 2010, 43: 2164-2173.

[41] Zhao D, Banks SA, D'Lima DD, Colwell Jr. CW, Fregly BJ. *In vivo* medial and lateral tibial loads during dynamic and high flexion activities. Journal of Orthopaedic Research. 2007, 25: 593-602.

[42] Indelli PF, Giori N, Maloney W. Level of constraint in revision knee arthroplasty. Current Reviews in Musculoskeletal Medicine: Revision Knee Arthroplasty. 2015, 8: 390-397.

[43] ASTM F1636-95e2, Standard specification for bores and cones for modular femoral heads (withdrawn 2001), ASTM International, West Conshohocken, PA, 1995, www.astm.org.

CHAPTER THREE*

THE EFFECT OF MANUFACTURING TOLERANCES ON THE MECHANICAL ENVIRONMENT OF TAPER JUNCTIONS IN MODULAR TKR

Introduction

Taper modularity has become a common design feature in orthopaedic devices due to the versatility it provides surgeons intraoperatively to address patient-specific needs. During revision total knee replacement (TKR), the bore-cone taper junctions allow surgeons to augment modular TKR components with intramedullary stem extensions for improved stability and bone fixation in patients with poor bone quality or defects [1, 2]. Despite these advantages, taper junctions have been associated with corrosive behavior because of mechanical instability [3-5] causing adverse tissue responses and limiting device longevity [6-8]. Mechanically assisted corrosion (MAC) is a commonly recognized corrosion mechanism in taper junctions, and involves the combination of localized stresses under loading and fretting, or micromotion between contacting surfaces [9, 10].

In response to the concerns surrounding modular taper junctions, the effect of taper design parameters on corrosion have been investigated. Both retrieval analyses on explanted taper junctions of modular total hip replacements (THR) [10, 11] and in vitro studies [12-14] have supported the occurrence of MAC mechanisms and confirmed that

*Results and data provided in this chapter were submitted for publication in:
Snethen K, Hernandez J, Harman MK. Effect of manufacturing tolerances on the mechanical environment of taper junctions in modular TKR. Journal of the Mechanical Behavior of Biomedical Materials. Manuscript submitted and in review, 2018.

taper design parameters influence corrosion. However, retrievals offer limited information regarding in vivo mechanics and in vitro studies are inefficient to perturb and repeat. Finite element (FE) analysis provides a more efficient framework and has been completed to determine the effect of material combination on stress and micromotion of modular bone replacement prostheses [15] and the effect of taper design parameters on contact mechanics in modular THR [16, 17]. Although retrieval analyses have also shown evidence of MAC mechanisms in modular TKR [18, 19], no studies have been completed to date analyzing taper design in modular TKR.

Despite the common objective in the aforementioned studies of determining the optimal taper junction design, a great deal of uncertainty surrounds this topic. The previous ASTM Standard F-1636 specified manufacturing tolerances for specific bore-cone taper pairs, but was discontinued leaving industry without guidance on appropriate manufacturing tolerances for taper designs [20]. Although manufacturing tolerance has been established as a design parameter critical to taper junction corrosion [11, 12, 16, 17], the isolated effects of incremental changes in manufacturing tolerance on the contact mechanics is still poorly understood. With the goal of minimizing taper junction corrosion, there is a need to define target manufacturing tolerances based on the effect it has on the taper junction mechanical performance.

The purpose of this study was to utilize parametric FE analysis in order to investigate the effect of manufacturing tolerance on stress and micromotion of modular TKR taper junctions. In this study, the angular mismatch between the cone and bore taper angles represented manufacturing tolerance and was perturbed in 0.05^{o} increments between

±0.25° by modeling different cone taper angles. The effect of manufacturing tolerance on the taper junction mechanical environment was investigated under multiple material combinations and applied loads representing various activities of daily living. The intent of the study was to provide insight to engineers as to what manufacturing tolerances should be targeted during taper junction design.

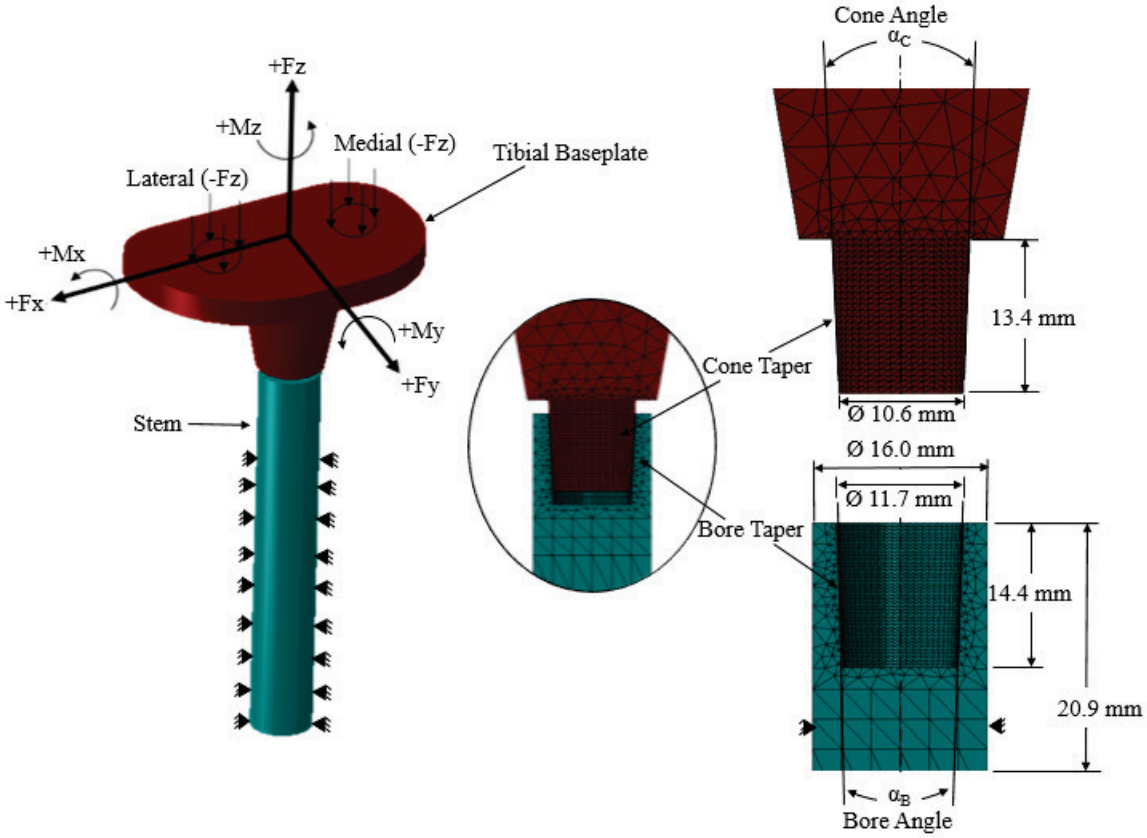

Figure 3.1. Schematic of the FE taper junction model with applied loading orientations.

Methods

In this study, the taper junction FE model developed in Chapter 2 was applied to perform a parametric analysis on taper junction geometry, and in particular, angular

mismatch between the bore and cone taper angles. The FE model implemented the elastoplastic material models defined in Chapter 2, and was validated against experimental data acquired through collaboration. The effect of these geometric variations on stress and micromotion was analyzed under loading conditions representing various activities.

Development of Taper Junction Finite Element Model

The FE taper junction model developed in Chapter 2 was used to complete this study, and thus modeling details will only be discussed briefly here. The generalized bore-cone taper junction model was initially created with a 5° angle for both tapers and a 0° angle mismatch between the bore and cone tapers representing a perfect fit (Figure 3.1).

Table 3.1. Variation of the cone taper angle design parameter and angular mismatch.

Bore Angle, α_B	Cone Angle, α_C	Angle Mismatch, $(\alpha_B-\alpha_C)$
5.00°	4.75°	+0.25°
5.00°	4.80°	+0.20°
5.00°	4.85°	+0.15°
5.00°	4.90°	+0.10°
5.00°	4.95°	+0.05°
5.00°	5.00°	0.00°
5.00°	5.05°	-0.05°
5.00°	5.10°	-0.10°
5.00°	5.15°	-0.15°
5.00°	5.20°	-0.20°
5.00°	5.25°	-0.25°

To account for the inherent manufacturing tolerances, the angle mismatch, defined as the bore angle minus the cone angle, was varied from 0° to ±0.25° at 0.05° increments by perturbing the angle of the cone taper located on the tibial baseplate (Table 3.1). The

positive mismatch condition is defined as the bore taper angle being greater than the cone taper angle, and contrarily the negative mismatch condition is defined as the bore taper angle being smaller than the cone taper angle. In order to isolate the effects of the angle mismatch (i.e. manufacturing tolerance), all other geometric parameters remained constant. ABAQUS (v6.14, Dassault Systemes, Waltham, MA) was used to perform the deterministic finite element analysis (Figure 3.1).

Table 3.2. Material property parameters assigned to the elastoplastic models for each material.

Material	Cast CoCrMo	Wrought/Forged CoCrMo	Wrought/Forged Ti6Al4V
Model Component	Baseplate with Cone Taper	Stem with Bore Taper	Stem with Bore Taper
Standard	ASTM F75	ASTM F1537, ASTM F799	ASTM F136
Elastic Modulus [GPa]	210	210	110
Poisson's Ratio	0.3	0.3	0.31
Yield Strength [MPa]	515*	935*	990*
% Elongation	12*	23*	13*
n	0.1162	0.0739	0.0416
K	1015.7	1438.8	1200.4
Published Sources	[21-30]	[21-23, 29, 31, 32]	[21, 33, 34]

*Based on average values from the published source data

Material properties of cast CoCrMo (ASTM F75) were assigned to the cone taper and the bore taper was assigned material properties of either wrought Ti6Al4V (ASTM F136) or wrought/forged CoCrMo (ASTM F1537/F799). Taper junction material combination will be specified as bore material-cone material. From this point forward, CoCrMo material designation will represent cast CoCrMo when in application of the cone taper of the baseplate and wrought/forged CoCrMo when in application of the bore taper of the stem; the Ti6Al4V designation will be in representation of wrought Ti6Al4V. An elastoplastic material model was developed for each material using experimental stress-strain data [21-34] and a power law approximation as described in Chapter 2. Optimization of the power law parameters to match the experimental data resulted in the parameters listed in Table 3.2 and stress-strain curves displayed in Figure 3.2. All materials were assumed to behave isotropically.

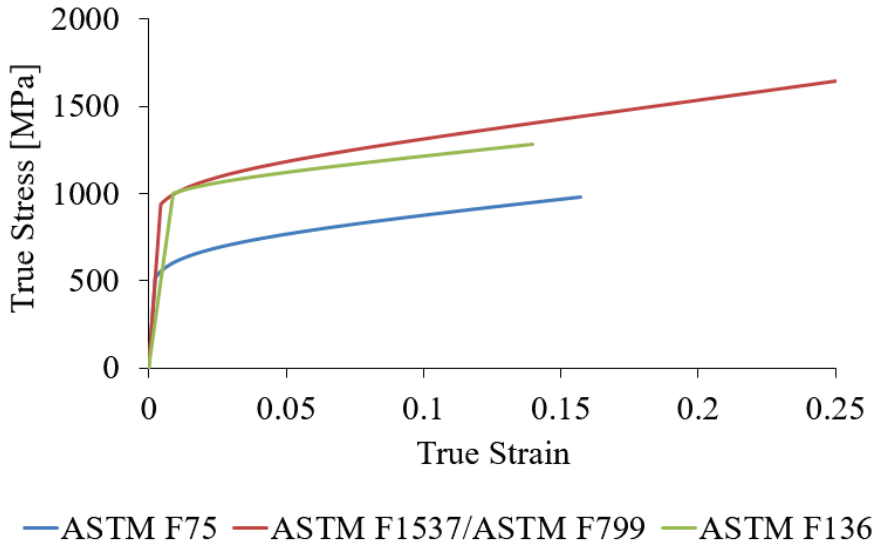

Figure 3.2. Engineering stress-strain curves implemented in the finite element analysis to model elastoplastic behavior for each represented material.

Contact was modeled using contact pairs with the cone taper assigned the master surface and the bore taper the slave surface, and enforced using the penalty method. The coefficient of friction (COF) at the taper interface was defined as a function of the contact pressure using an exponential decay model [35] fit to experimental data [36] represented by

$$\mu = \mu_0 + (\mu_0 - \mu_\infty)e^{-d_c P}$$

where P is the contact pressure, μ_o is the coefficient of friction at zero contact pressure, μ_∞ is the coefficient of friction at increasing contact pressure, and d_c is the decay factor. The decay factor, d_c, was optimized in order to match *in vitro* test data for Ti6Al4V-CoCrMo and CoCrMo-CoCrMo interfaces, respectively. Both material pairs had μ_o=0.8 and μ_∞ =0.3 with varying d_c of 0.056 for Ti6Al4V-CoCrMo and 0.079 for CoCrMo-CoCrMo (Figure 3.3).

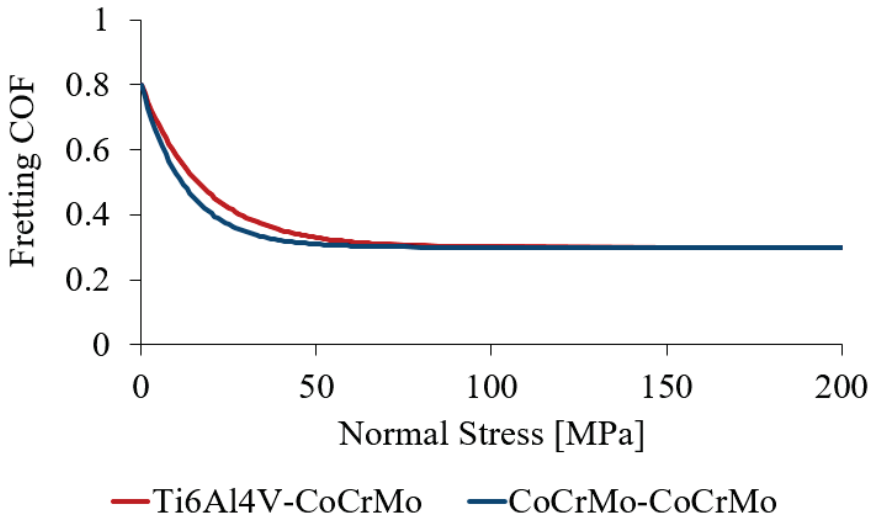

Figure 3.3. Fretting COF and normal stress relationship for each bore-cone material combination defined as part of the contact formulation in the finite element analysis.

Model Loading and Boundary Conditions

A dynamic, implicit simulation was completed in two steps: (1) a compressive axial assembly load equivalent to surgical impaction force to seat the cone taper into the bore was applied and (2) a physiological activity loading profile composed of vertical compressive forces along with flexion-extension and internal-external moments. Gait, stair descent, and chair rise/sit activities were each simulated individually. During the assembly step, a 4400 N assembly load, measured to be the average impaction force applied by orthopaedic surgeons in a study by Heiney et al., was applied [37]. Loading conditions for all activity cycles were defined from published telemetric data (Figure 3.4) [38]. The resultant compressive force (-Fz) was split 55% medial-45% lateral [39] and distributed in a circular pattern about 4 nodes in the respective regions on the superior surface of the tibial baseplate generating an abduction-adduction moment (My) in the frontal plane.

Moment and force profiles assumed a 940 N body weight for each activity, and were applied to the corresponding axes via a reference node coupled to the superior surface of the baseplate as detailed in Chapter 2 [38]. The physiological loading step required two loading cycles for each activity in order to allow the taper junction to stabilize. Boundary conditions were representative of a worst-case scenario of distal stem fixation without support of the proximal tibial bone (Figure 3.1).

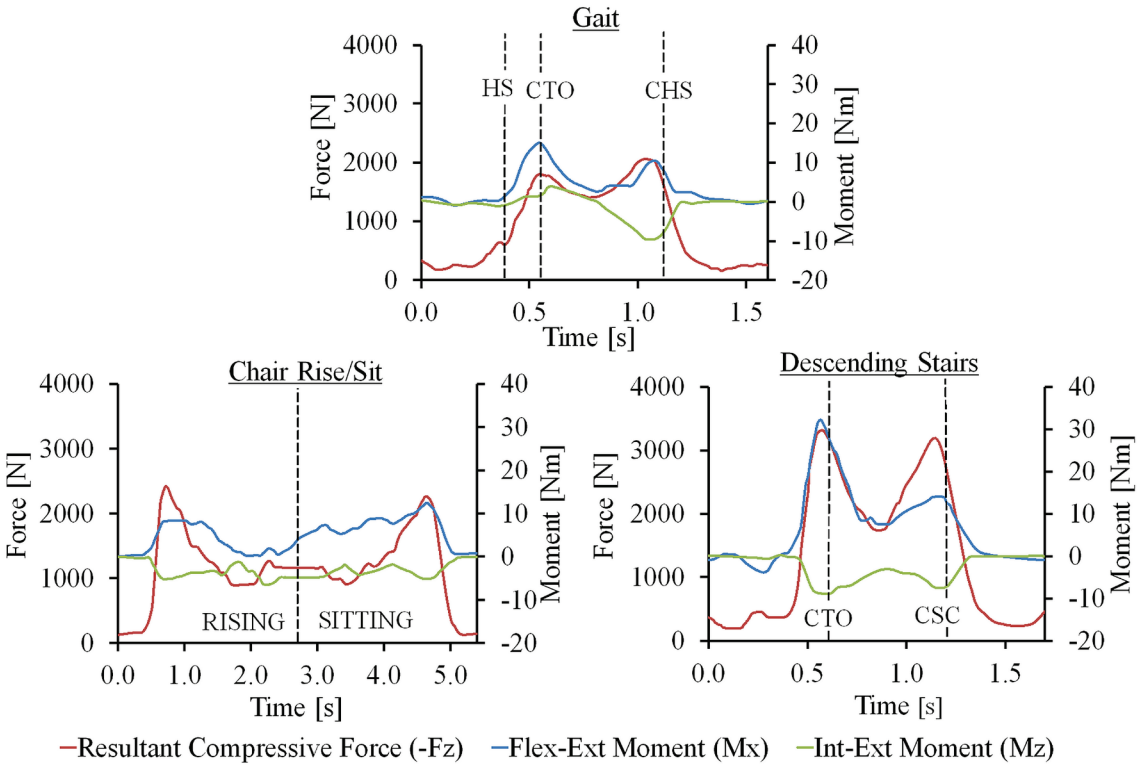

Figure 3.4. Physiological loading cycles for gait, chair rise/sit and stair descent applied in the dynamic finite element simulation with respect to the corresponding axes. HS = heel strike; CHS = contralateral heel strike; CTO = contralateral toe off; CSC = contralateral stair contact.

Validation of Taper Junction Finite Element Model

Through collaboration with a previous study [17], the FE models were validated against experimental micromotion measured on two sets of bore-cone pairs, generating 4 different angular mismatch combinations (Figure 3.5). The experimental testing implemented a 5000 N axial compressive load followed by a 0-5000 N ramp load at 45° off-axis. The experimental taper junction was machined out of 6061 aluminum at approximately a 3:1 scale in order to meet micromotion measurement capabilities and to allow for accurate measurement of taper angles on the machined parts. Experimental

micromotion of the isolated bore-cone taper junction was measured using two differential variable reluctance transducers (DVRTs) capable of 600 nm accuracies axially aligned across the taper interface. Although the initial intent of the experimental setup was for modular THR application with varying center offsets, the largest center offset of 60 mm well represented the loading condition of the modular TKR taper junction being modeled in this study; hence, only micromotion data from this condition was used for validation. The experimental study resulted in micromotions at superior and inferior regions due to the inclination of the taper junction in THR which translated to the lateral and medial regions in TKR based on the orientation of the resultant moment acting on the taper junction. Further details for the experimental setup can be found in the previously published study by Donaldson et al. [17]. Separate FE models were created to match the exact geometry of the four different experimental bore and cone taper parts and the experimental loading and boundary conditions resulting in four simulations. Experimentally measured and model predicted micromotions were compared for each bore-cone taper pair.

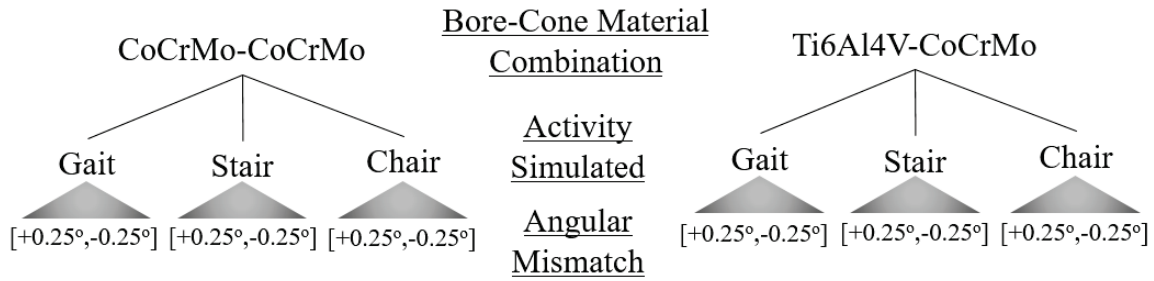

Figure 3.5. Diagram of the experimental design demonstrating the variable parameters.

Experimental Design of Study

A total of 66 simulations were run in order to analyze the effect of angular mismatch on the mechanics of the taper junction when the bore-cone material combination and activity simulated are varied (Figure 3.5). Micromotion and von Mises stress were the mechanical parameters analyzed. Micromotion was calculated as the magnitude of relative tangential motion in the two directions perpendicular to the surface normal of the contact elements at the location where bore-cone taper contact existed. The micromotion reported represented the maximum magnitude calculated across the taper interface, and is not an accumulative value, but instead calculated relative to the end of the previous loading step. To compare the stresses in the taper junction across all analyses, von Mises stress, σ, defined as

$$\sigma = \sqrt{\frac{3}{2} S_{ij} S_{ij}}$$

where S_{ij} is the deviatoric stress tensor, was chosen due to a triaxial stress environment within the taper junction as well as the general use of the von Mises yield criterion in stress analysis of isotropic ductile metals.

The maximum von Mises stress was recorded for both the bore and cone tapers at the end of the assembly step, activity cycle 1, and activity cycle 2 when only nominal loads were being applied; thus, the reported stresses represent residual stresses. A plastic strain magnitude, ε_{pl}, defined as

$$\varepsilon_{pl} = \sqrt{\frac{2}{3} E_{ij} E_{ij}}$$

where E_{ij} is the plastic strain tensor, was recorded to analyze the elastoplastic material behavior under different angular mismatches and activity cycles. Finally, spearman's rank correlation coefficient was used to analyze the correlation between parameters of interest and angular mismatch.

Results

Experimental and model predicted micromotions showed good agreement in trends and an average absolute difference of 25.5 μm (Figure 3.6). The variation in micromotion could be attributed to the precision of machining and measuring the physical taper parts as the FE models were developed from nominal dimensions of the taper design specifications. Additionally, higher accuracy is expected for the true size models compared to the scaled up validation geometry.

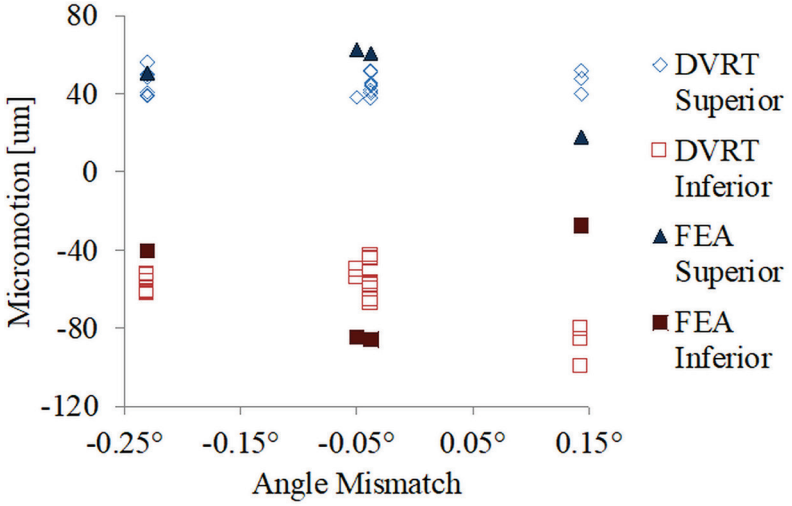

Figure 3.6. Validation analysis using experimental micromotion from four different bore-cone taper pairs exhibited to compressive axial and off-axis loading.

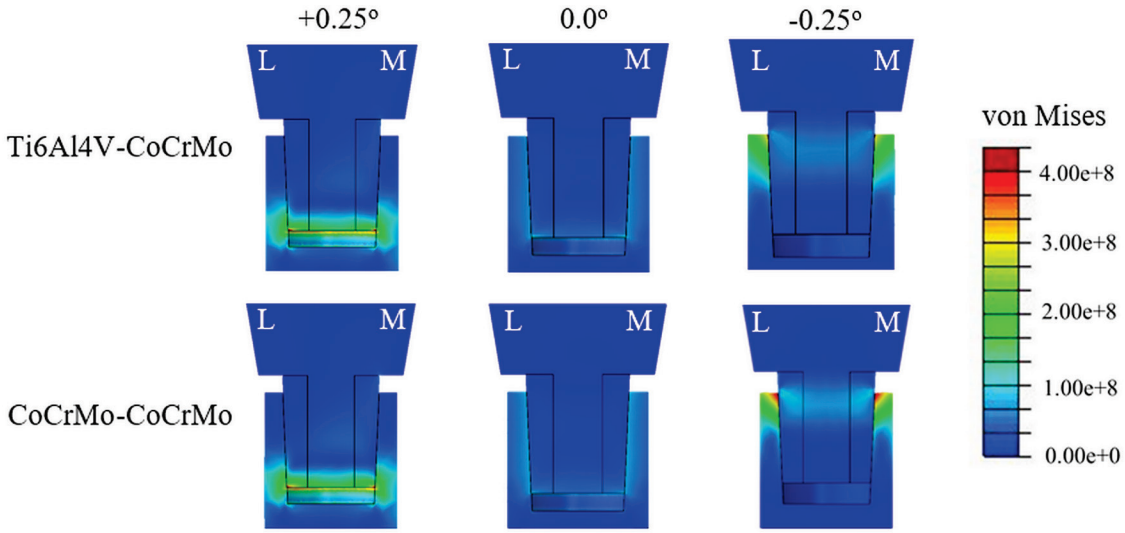

Figure 3.7. Frontal section of modular TKR taper junctions displaying von Mises stress distribution under physiological loading of a gait cycle simulation for both Ti6Al4V-CoCrMo and CoCrMo-CoCrMo bore-cone material combinations at +0.25°, 0°, and -0.25° angle mismatch. Medial and lateral regions denoted by M and L, respectively.

The parametric analysis of angular mismatch revealed distinct stress distributions for positive and negative angle mismatches regardless of bore-cone material combination or activity simulated. A perfect fit resulted in a relatively uniform stress distribution while positive and negative mismatches lead to distal and proximal stress concentrations, respectively (Figure 3.7). As the angle mismatch transitioned from a positive to a negative mismatch, the maximum stress shifted from the cone to the bore taper. In further analyzing the stress environment of the taper junction, triaxial compression was experienced by the cone taper with the two principal stress components in the transverse plane corresponding to radial and tangential, or hoop, stress as the cone penetrates the bore taper during compressive loading. The stress environment in the bore taper was similar to that of the

cone with the exception of a tensile hoop stress in response to the bore taper expanding outward to impede further penetration of the cone taper.

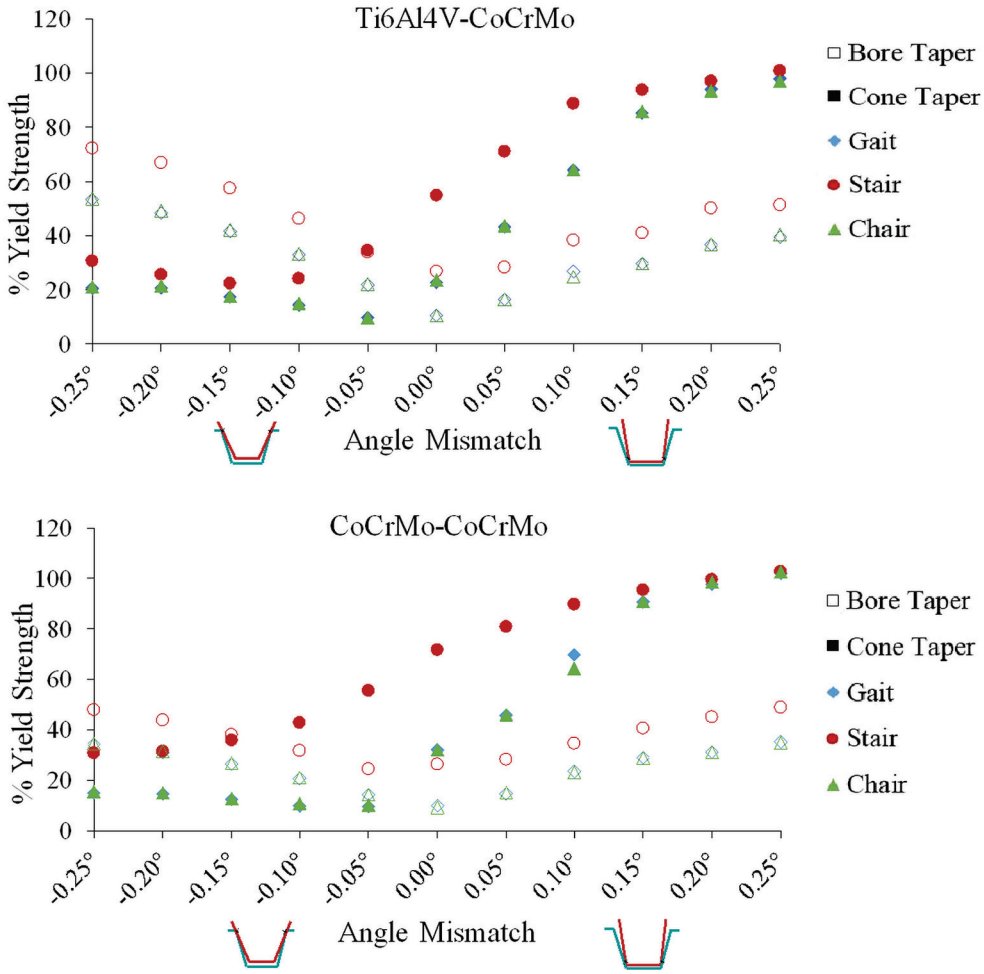

Figure 3.8. Maximum stress in the bore and cone tapers plotted as the percentage of yield strength for the Ti6Al4V-CoCrMo and CoCrMo-CoCrMo material combination over the entire range of angle mismatches for gait, stair descent and chair rise/sit activities.

Residual von Mises stress at the cone and bore tapers peaked at +0.25° and -0.25° of mismatch, respectively, but followed distinct trends as angle mismatch increased. Stress in the bore taper was a minimum near 0° angle mismatch and increased as angle mismatch

increased regardless of mismatch direction. Stress in the cone taper increased from -0.25° mismatch towards +0.25° until reaching approximately 100% yield stress at +0.10° (Figure 3.8). Beyond +0.10°, cone taper stress remained relatively constant with increasing positive mismatch up to +0.25°. The stair descent activity generated higher stresses compared to the gait and chair rise/sit activities, but stress in the cone taper converged across the three activities as mismatch increased, especially for positive mismatch (Figure 3.8).

Post-yield stresses and plastic deformation only occurred in the cone taper under positive mismatch conditions. For positive angle mismatches >0.10°, plastic strain was produced during assembly and was further increased under stair descent loading conditions only, with the exception of +0.25° angle mismatch which experienced increases in plastic strain during all activity loading cycles. Positive mismatch conditions ≤0.10° only produced plastic strain after subsequent stair descent loading cycles.

Overall, micromotion increased with increased angle mismatch, and exhibited less variation for gait and chair rise/sit simulations compared to stair descent. The maximum micromotion experienced across all activities was 32.1 μm, and occurred at -0.25° mismatch under stair descent conditions for a Ti6Al4V-CoCrMo taper junction. A 0° angle mismatch, the ideal condition, consistently resulted in the lowest settled micromotion across all simulations. For the gait and chair rise/sit activities, micromotion ranged from 0.2-8.9 μm for both cycles, and varied less than a 1.7 μm between the two activities across all angle mismatches (Figure 3.9). The stair descent activity varied as much as a 28.1 μm between the first and second activity cycle (Figure 3.9), and calculated a range in

micromotion of 11.5-32.1 μm during the first cycle compared to 1.5-10.0 μm during the second.

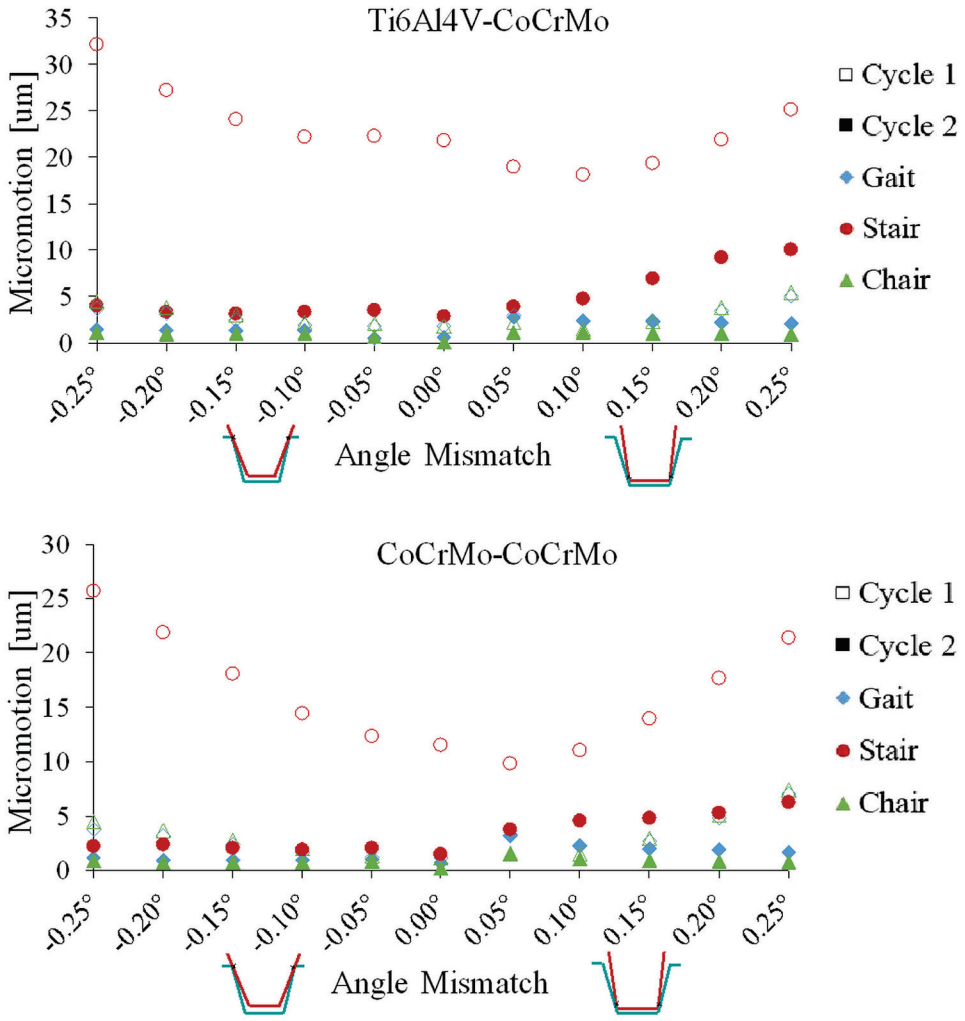

Figure 3.9. Maximum micromotion at the bore-cone taper interface for the first and second cycle of each activity simulated across all angle mismatches.

Strong correlations were seen between angle mismatch and stress within the taper junction for both material combinations under all activity levels with stronger correlations for stress in the bore taper compared to the cone taper (Table 3.3). In general, as the angle

mismatch became more negative or more positive the stress within the taper junction increased. Correlations between angle mismatch and micromotion were not as strong, and were weaker for micromotion during cycle 2 relative to cycle 1. In most cases, an increase in mismatch in either the positive or negative direction led to a greater micromotion. Overall, material combination and physiological activities showed similar trends in correlations.

Table 3.3 Spearman's rank correlation coefficients between angle mismatch direction and stress and angle mismatch and micromotion (denoted μm) for both material combinations under each activity loading conditions.

		Ti6Al4V-CoCrMo				CoCrMo-CoCrMo			
		Stress in Bore	Stress in Cone	μm Cycle 1	μm Cycle 2	Stress in Bore	Stress in Cone	μm Cycle 1	μm Cycle 2
Gait	(+)	1.00	1.00	0.86	-0.14	1.00	1.00	0.83	-0.14
	(-)	-1.00	-0.86	-0.74	-1.03	-1.00	-0.09	-0.74	-0.49
Stair	(+)	1.00	1.00	0.60	1.00	1.00	1.00	0.83	1.00
	(-)	-0.94	1.00	-0.94	-0.57	-1.00	0.49	-1.00	-0.80
Chair	(+)	1.00	1.00	0.83	-0.20	1.00	1.00	0.94	-0.14
	(-)	-1.00	-0.14	-1.00	-1.00	-1.00	-0.09	-1.00	-0.51

Comparison of material combination predicted greater stresses in the CoCrMo-CoCrMo combination and greater micromotion in Ti6Al4V-CoCrMo. In negative mismatch conditions, the CoCrMo-CoCrMo taper junction generated up to a 37.7% increase in stress on the bore taper and 31.5% increase on the cone taper (Figure 3.10). The Ti6Al4V-CoCrMo and CoCrMo-CoCrMo taper junctions produced very similar stress results in the positive mismatch condition when the stress is concentrated on the cone taper.

This trend in differences in stress between the two material combinations was evident in all activities simulated. Comparing micromotion, the Ti6Al4V-CoCrMo taper junction generated greater micromotions in comparison to CoCrMo-CoCrMo in all three mismatch conditions, and was more apparent under stair descent activity loading (Figure 3.11). The greatest difference was a 58.1% increase at negative mismatch for stair descent.

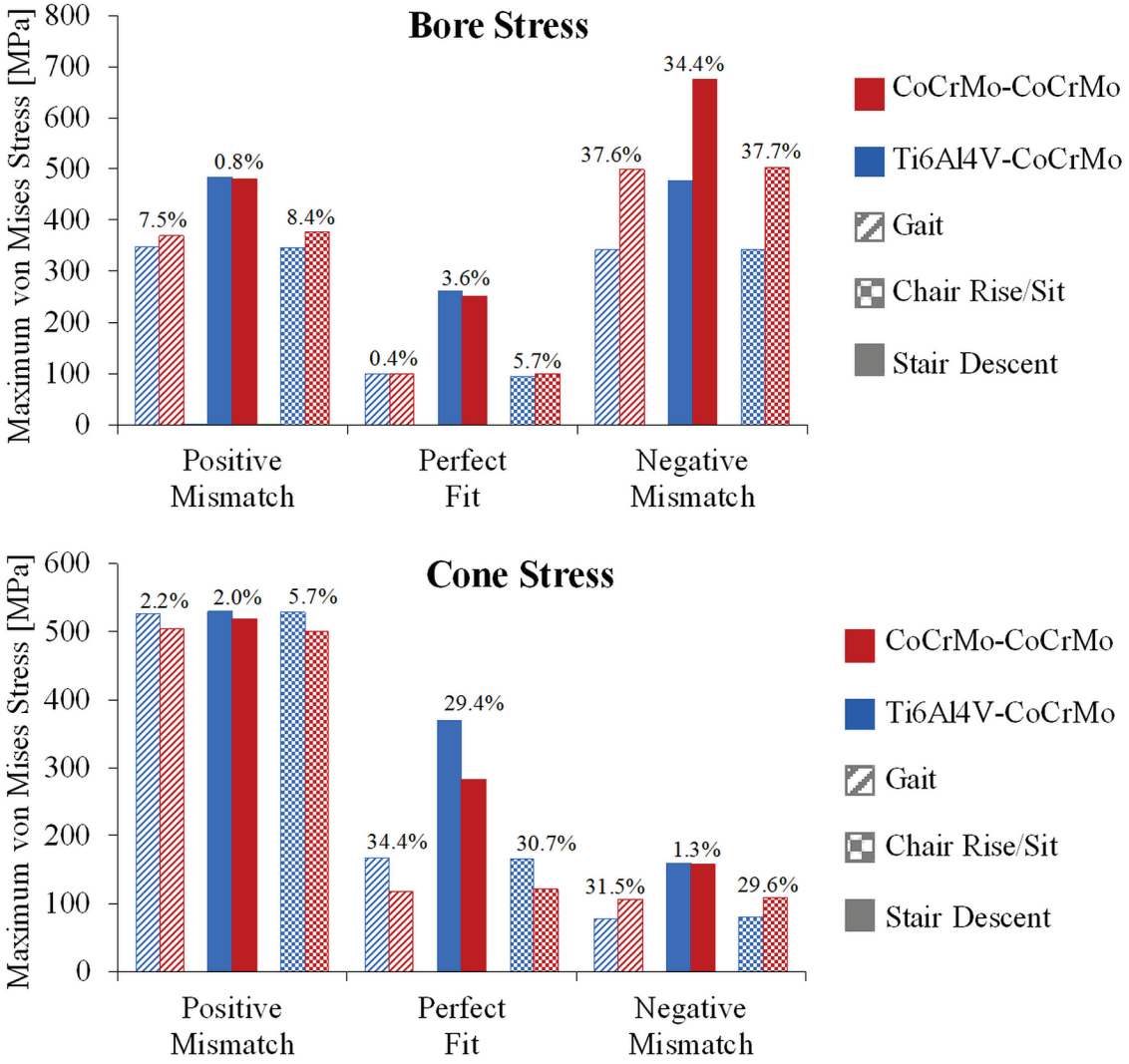

Figure 3.10. Comparison of bore and cone stress between Ti6Al4V-CoCrMo and CoCrMo-CoCrMo material combinations under different simulated activities and +0.25°, 0°, and -0.25°. Percent difference is presented above each comparison.

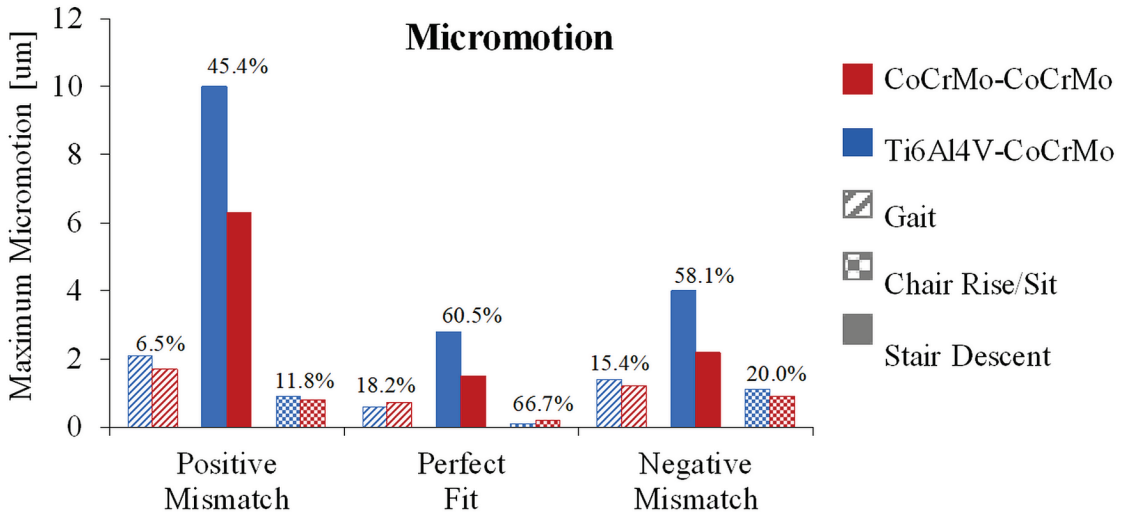

Figure 3.11. Comparison micromotion between Ti6Al4V-CoCrMo and CoCrMo-CoCrMo material combinations under different simulated activities and +0.25°, 0°, and -0.25°. Percent difference is presented above each comparison.

Discussion

The parametric FE analysis of angular mismatch in modular TKR taper junctions found that an increase in mismatch generally resulted in higher stress and micromotion. However, micromotion exhibited less variation in angle mismatches near 0° and stress exhibited less variation at the mismatch approached ±0.25°. This resulted in stronger correlations between angle mismatch and stress than angle mismatch and micromotion which agrees with a previous multivariate FE study [17]. Plastic deformation was only present in the cone taper, but for all positive mismatches. Plastic strain was greatest for +0.25° corresponding with the convergence of stress in the cone taper between the different activities simulated. Although the stair descent simulation produced the greatest stresses and micromotion, similar trends between these parameters and angle mismatch were observed regardless of loading activity or material combination.

Stress distributions within the bore-cone taper junction were a direct result of the proximal and distal initial contact conditions set forth by a negative and positive angle mismatch, respectively. Stress in the cone taper increased for positive mismatches and decreased for negative mismatches due in part to the bore taper providing less mechanical resistance proximally compared to distally because of less material support at its opening. Furthermore, as angle mismatch increased the interfacial contact area to distribute the applied load over decreased leading to the increasing stress magnitudes with increasing angle mismatch evident in the results. These mechanics led to the strongest correlations between stress in the bore taper and negative angle mismatch and between stress in the cone taper and positive angle mismatch.

The combination of a stress concentration and plastic behavior caused the stress in the cone taper to plateau and converge between the three activates simulated as positive angular mismatch increased. In the positive mismatch condition, the leading edge of the cone taper contacts the bore taper forming a line of contact. For smaller positive mismatches, the stress distributes away from the leading edge due to material deformation and the small gap between the bore and cone taper interface, but as the mismatch increases the contact area decreases and the stress concentrates at the leading edge. Since the geometry of the leading edge was kept constant, eventually additional changes in angle mismatch did not significantly alter contact and caused the stress to plateau. This is recognized as a worst-case scenario and would be mitigated with a machined fillet in reality. The stress concentration also produced post-yield stresses leading to plastic behavior, specifically strain hardening. As the plastic deformation produced during

assembly increased with increasing positive mismatch, it became increasingly difficult for subsequent loading to further yield behavior and alter the stress environment. Essentially, the final stress environment became more influenced by the assembly step as the positive mismatch increased, and activity loading had a decreasing effect leading to cone taper stress to converge.

Micromotion was also influenced by the taper fit. As expected, the perfect taper fit led to the least amount of motion a result of complete interfacial contact between the bore and cone tapers (i.e. no initial gap separation). Once the angle mismatch deviated from this ideal condition, a pivot point was developed at a specific corner of the taper junction generating a rocking motion about this point. The pivot point was located at the proximal medial contact region and at the distal medial contact region for negative and positive mismatch conditions, respectively. Higher micromotions were produced in the positive mismatch condition during gait and chair rise/sit simulations because of the larger moment arm from the pivot point to the medial compressive load generating a greater frontal plane moment. The same trend was not seen in the stair descent simulations which could be attributed to the presence of plastic deformation locally increasing the contact area and consequently decreasing micromotion. In general, increased mismatch led to a decreased contact area to resist the relative sliding motion. Compared to reported micromotion in other modular orthopaedic devices, micromotions reported herein were within the ranges of some studies [14, 41, 42] while much less than reported in others [15, 43]. The decrease in micromotion in comparison to THR is not surprising given the offsetting moments

(medial and lateral compressive forces) present during TKR physiological loading compared to a concentrated load acting on the same moment arm in THR.

The model predicted stress distributions agreed with retrieval analysis and *in vitro* corrosion behavior. The predicted stress distributions for the different angle mismatch conditions simulated agreed with corrosion patterns evident in taper junctions of retrieved modular TKR devices [19]. A similar correlation between FE predicted stress concentrations and regions of more severe corrosion in retrieved modular taper junctions was made in a study investigating potential failure modes for a specific modular THR design [44]. Additionally, the FE analysis in this study calculated stress magnitudes less than the material yield strength across the majority of the taper junction interface. A recent *in vitro* study showed corrosion rates and pitting can peak at stresses 50-75% yield strength which was within the range reported in this study [45]. Despite completed *in vitro* testing providing insight on parameters that influence MAC mechanisms [13, 14, 46], further experiments linking corrosive behavior to micromotion and local stresses could supplement such computational analyses in order to define robust target ranges for manufacturing tolerances of taper junctions in modular TKR.

The reported effects of angular mismatch on stress and micromotion are also consistent with the previous ASTM standard. The ASTM Standard F-1636 for modular THR specified a maximum individual taper tolerance of ±0.1° with all nominal angle mismatches being positive. Based on the results of the conducted study, this ±0.1° tolerance range would be suitable if the design intent was for a nominal perfect fit (0°) between the bore and cone tapers. In this tolerance range, the study showed micromotion

to vary less than 3.4 microns for all activities and maximum stresses within the taper junction to be generally less than 50% of yield strength. Taking into account the compound tolerance of the bore and cone tapers with the specified nominal angle mismatch, the angle mismatches of the taper junction pairs ranged from +0.48° to -0.20° in the ASTM standard. This study does not support the extreme angle mismatches listed when considering a non-perfect nominal fit as these produced much higher micromotions and stresses in comparison to the perfect fit condition. It should be noted that manufacturing tolerances are not limited to taper angle and also involve roundness and straightness of the conical tapers; however, these were outside the scope of this study and taper contours were modeled as perfectly straight and round.

Conclusion

In summary, the mechanical environment within taper junctions of modular TKR is influenced by manufacturing tolerance (i.e. angle mismatch between bore and cone tapers). Greater angular mismatch generated higher stresses and micromotions; however the direction of the mismatch dictated the extent of micromotion and the location of the stress concentration. Overall, negative angular mismatches led to higher stresses on the bore taper and smaller micromotions in comparison to positive angular mismatches which led to higher stresses on the cone. Correspondence between model stress distributions and magnitudes with corrosion patterns on retrieved taper junctions and *in vitro* corrosive behavior suggests that localized stresses play a crucial role in taper junction corrosion. Stronger correlations were found between angular mismatch and maximum stress compared to between angular mismatch and micromotion due to little variance in

micromotion seen within ±0.1° of mismatch. This finding supports the ±0.1° maximum taper tolerance specified in the previous ASTM F-1636 Standard assuming a nominal perfect fit between bore and cone tapers. Further understanding of the role mechanical parameters such as stress and micromotion play in the incidence of taper junction corrosion would complement such computational analyses to help inform industry on target manufacturing tolerance ranges.

References

[1] Rawlinson JJ, Closkey RF, Davis N, Wright TM, Windsor R. Stemmed implants improve stability in augmented constrained condylar knees. Clinical Orthopaedics and Related Research. 2008, 466: 2639-2643.

[2] Scott CEH, Biant LC. The role of the design of tibial components and stems in knee replacement. Journal of Bone and Joint Surgery. 2012, 94: 1009-1015.

[3] Harman MK, Baleani M, Juda K, Viceconti M. Repeatable procedure for evaluating taper damage on femoral stems with modular necks. Journal of Biomedical Materials Research Part B. 2011, 99B: 431-439.

[4] Jones DM, Marsh JL, Nepola JV, Jacobs JJ, Skipor AK, Urban RM, Gilbert JL, Buckwalter JA. Focal osteolysis at the junctions of a modular stainless-steel femoral intramedullary nail. Journal of Bone and Joint Surgery. 2001, 83-A.

[5] Lieberman JR, Rimnac CM, Garvin KL, Klein RW, Salvati EA. An analysis of the head-neck taper interface in retrieved hip prostheses. Clinical Orthopaedics and Related Research. 1994, 300: 162-167.

[6] Cooper JH, Della Valle CJ, Berger RA, Tetreault M, Paprosky WG, Sporer SM, Jacobs JJ. Corrosion at the head-neck taper as a cause for adverse local tissue reaction after total hip arthroplasty. Journal of Bone and Joint Surgery. 2012, 94: 1655-1661.

[7] Lombardi AVJ. Case studies in management of THA failure secondary to taper corrosion, modular junctions and metal-on-metal bearings. Journal of Arthroplasty. 2014, 29: 663-667.

[8] McMaster WC, Patel J. Adverse local tissue response lesion of the knee associated with morse taper corrosion. Journal of Arthroplasty. 2013, 28(2): 375.e5-375.e8.

[9] Gilbert JL, Buckley CA, Jacobs JJ. *In vivo* corrosion of modular hip prosthesis components in mixed and similar metal combinations. The effect of crevice, stress, motion, and alloy coupling. Journal of Biomedical Material Research Part A. 1993, 27(12): 1533-1544.

[10] Goldberg JR, Gilbert JL, Jacobs JJ, Bauer TW, Paprosky W, Leurgans S. A multicenter retrieval study of taper interfaces of modular hip prostheses. Clinical Orthopaedics and Related Research, 2002, 401: 149-161.

[11] Langton DJ, Sidaginamale R, Lord JK, Nargol AVF, Joyce TJ. Taper junction failure in large-diameter metal-on-metal bearings. Bone & Joint Research. 2012, 1: 56-63.

[12] Jani SC, Sauer WL, McLean TW, Lambert RD, Kovacs P. Fretting corrosion mechanisms at modular implant interfaces. American Society for Testing and Materials ASTM STP 1301. 1997.

[13] Goldberg JR., Gilbert JL. *In vitro* corrosion testing of modular hip tapers. Journal of Biomedical Material Research Part B: Applied Biomaterials. 2003, 64: 78-93.

[14] Jauch SY, Huber G, Haschke H, Sellenschloh K, Morlock MM. Design parameters and the material coupling are decisive for the micromotion magnitude at the stem-neck interface of bi-modular hip implants. Medical Engineering & Physics. 2014, 36: 300-307.

[15] Chu Y, Elias JJ, Duda GN, Frassica FJ, Chao EYS. Stress and micromotion in the taper lock joint of a modular segmental bone replacement prosthesis. Journal of Biomechanics. 2000, 33: 1175-1179.

[16] Shareef N, Levine D. Effect of manufacturing tolerances on the micromotion at the Morse taper interface in modular hip implants using the finite element technique. Biomaterials. 1996, 17: 623-630.

[17] Donaldson FE, Coburn JC, Lohmann Siegel K. Total hip arthroplasty head-neck contact mechanics: A stochastic investigation of key parameters. Journal of Biomechanics. 2014, 47: 1634-1641.

[18] Arnholt CM, MacDonald DW, Tohfafarosh M, Gilbert J, Rimnac CM, Kurtz SM, Implant Research Center Writing Committee. Mechanically assisted taper corrosion in modular TKA. Journal of Arthroplasty. 2014, 29 (Suppl. 2): 205-208.

[19] Panigrahi P, Schwartzman K, Lutzner J, Kirschner S, Harman MK. Surface corrosion of taper interfaces in explanted total knee replacements with modular stems. 2014 International Conference on Biotribology, Toronto, Canada.

[20] ASTM F1636-95e2, Standard specification for bores and cones for modular femoral heads (withdrawn 2001), ASTM International, West Conshohocken, PA, 1995, www.astm.org.

[21] ASM Materials for Medical Devices Database Committee, 2009. Materials and Coatings for Medical Devices: Cardiovascular. ASM International, Materials Park, Ohio.

[22] Berlin RM, Gustavson LJ, Wang KK. Influence of post processing on the mechanical properties of investment cast and wrought Co-Cr-Mo alloys. Cobalt-Base Alloys for Biomedical Applications. 1999, ASTM STP 1365: 62-70.

[23] Berry G, Bolton JD, Brown JB, McQuaide S. The production and properties of wrought high carbon Co-Cr-Mo alloys. Cobalt-Base Alloys for Biomedical Applications. 1999, ASTM STP 1365: 11-31.

[24] Cohen J, Rose RM, Wulff J. Recommended heat treatment and alloy additions for Cast Co-Cr surgical implants. Journal of Biomedical Materials Research. 1978, 12(6): 935-937.

[25] Devine TM, Wulff J. Cast vs. wrought cobalt-chromium surgical implant alloys. Journal of Biomedical Materials Research. 1975, 9 (2): 151-167.

[26] Dobbs HS, Robertson JLM. Heat treatment of cast Co-Cr-Mo for orthopaedic implant use. Journal of Materials Science. 1983, 18: 391-401.

[27] Hodge FG, Lee TS. Effects of processing on performance of cast prosthesis alloys. Corrosion. 1975, 31(3): 111-114.

[28] Hollander R, Wulff J. New technology for mechanical property improvement of cast Co-Cr-Mo-C surgical implants. Engineering in Medicine. 1974, 3(4): 8-9.

[29] Mishra AK, Hamby MA, Kaiser WB. Metallurgy, microstructure, chemistry and mechanical properties of a new grade of cobalt-chromium alloy before and after

porous-coating. Cobalt-Base Alloys for Biomedical Applications. 1999, ASTM STP 1365: 71-88.

[30] Spires WP, Kelman DC, Pafford JA. Mechanical evaluation of ASTM F75 alloy in various metallurgical conditions. Quantitative Characterization and Performance of Porous Implants for Hard Tissue Applications. 1987, ASTM STP 953: 47-59.

[31] Kumar P, Hickl AJ, Asphahani AI, Lawley A. Properties and characteristics of cast, wrought, and powder metallurgy (P/M) processed Cobalt-Chromium-Molybdenum implant materials. Corrosion and Degradation of Implant Materials: Second Symposium. 1985, ASTM STP 859: 30-56.

[32] Lippard HE, Kennedy RL. Processm of wrought CoCrMo alloy. Cobalt-Base Alloys for Biomedical Applications. 1999, ASTM STP 1365: 96-107.

[33] Murr LE, Esquivel EV, Quinones SA, Gayton SM, Lopez MI, Martinez EY, Medina F, Hernandez DH, Martinez E, Martinez JL, Stafford SW, Brown DK, Hoppe T, Meyers W, Lindhe U, Wicker RB. Microstructures and mechanical properties of electron beam-rapid manufactured Ti-6Al-4V biomedical prototypes compared to wrought Ti-6Al-4V. Materials Characterization. 2009, 60: 96-105.

[34] Ploeg HL, Burgi M, Wyss UP. Hip stem fatigue test prediction. International Journal of Fatigue. 2009, 31(5): 894-905.

[35] Oden JT, Martins JAC. Models and computational methods for dynamic friction phenomena. Computer Methods in Applied Mechanics and Engineering. 1985, 52: 527-634.

[36] Swaminathan V, Gilbert JL. Fretting corrosion of CoCrMo and Ti6Al4V interfaces. Biomaterials. 2012, 33(22): 5487-5503.

[37] Heiney JP, Battula S, Vrabec GA, Parikh A, Blice R, Schoenfeld AJ, Njus GO. Impact magnitudes applied by surgeons and their importance when applying the femoral head onto the Morse taper for total hip arthroplasty. Archives of Orthopaedic and Trauma Surgery. 2009, 129: 793-796.

[38] Kutzner I, Henlein B, Graichen F, Bender A, Rohlmann A, Halder A, Beier A, Bergmann G. Loading of the knee joint during activities of daily living measured *in vivo* in five subjects. Journal of Biomechanics. 2010, 43: 2164-2173.

[39] Zhao D, Banks SA, D'Lima DD, Colwell Jr. CW, Fregly BJ. *In vivo* medial and lateral tibial loads during dynamic and high flexion activities. Journal of Orthopaedic Research. 2007, 25: 593-602.

[40] Tadepalli SC, Erdemir A, Cavanagh PR. Comparison of hexahedral and tetrahedral elements in finite element analysis of foot and footwear. Journal of Biomechanics. 2011, 44: 2337-2343.

[41] Jauch SY, Huber G, Hoenig E, Baxmann M, Grupp TM, Morlock MM. Influence of material coupling and assembly condition on the magnitude of micromotion at the stem-neck interface of a moduar hip endoprosthesis. Journal of Biomechanics. 2011, 44: 1747-1751.

[42] Grupp TM, Weik T, Bloemer W, Knaebel HP. Modular titanium alloy neck adapter failures in hip replacement- failure mode analysis and influence of implant material. BMC Musculoskeletal Disorders. 2010, 11:3.

[43] Viceconti M, Baleani M, Squarzoni S, Toni A. Fretting wear in a modular neck hip prosthesis. Journal of Biomedical Material Research. 1997, 35(2): 207-2016.

[44] Lanting BA, Teeter MG, Vasarhelyi EM, Ivanov TG, Howard JL, Naudie DDR. Correlation of corrosion and biomechanics in the retrieval of a single modular neck total hip arthroplasty design: modular neck total hip arthroplasty system. Journal of Arthroplasty. 2015, 30: 135-140.

[45] Panigrahi P, Poursaee A, Harman MK. Corrosion behavior of Ti-6Al-4V orthopaedic alloy under tensile stress. 2015 Society for Biomaterials, Charlotte, NC.

[46] Baxmann M, Jauch SY, Shilling C, Blomer W, Grupp TM, Morlock MM. The influence of contact conditions and micromotions on the fretting behavior of modular titanium allow taper connections. Medical Engineering & Physics. 2013, 35: 676-683.

CHAPTER FOUR*

SENSITIVITY OF CALCULATED LIGAMENT TENSIONS TO INTRAOPERATIVE KNEE KINEMATICS: A FINITE ELEMENT COMPUTATIONAL STUDY

Introduction

During total knee replacement (TKR) procedures, intraoperative assessments of passive (non-weight bearing) range of motion (ROM) are routinely performed by the surgeon to assess ligament balance, providing them manual feedback about ligament tension. Given that inadequate ligament balance after TKR contributes to approximately 25% of revisions within 2 years [1], it can be inferred that discrepancies in ligament tension go undetected during passive ROM in some patients. Current determination of ligament tension intraoperatively is achieved by the "feel" of the surgeon and is highly subjective [2]. Attempts to quantify ligament tension intraoperatively during TKR have focused on global representations of tension in the soft-tissue envelope, but their findings have not been linked to postoperative outcomes [3-6]. Thus, adequate ligament tension is difficult to define and there is little evidence to guide.

Due to the challenges of directly measuring ligament tensions *in vivo* in patients and *in vitro* in cadavers, computational modeling is a common approach to predict ligament tensions from experimentally measured joint kinematics or applied loads [7-10]. Recent advances in motion capture technology are making intraoperative kinematics more readily

*Results and data provided in this chapter were submitted for publication in:
Snethen K, Harman MK, Lutzner J, Yao H, Fitzpatrick C. Sensitivity of calculated ligament tensions to intraoperative knee kinematics: a FE computational study. Journal of Biomechanics. Manuscript submitted and in review, 2018.

available [11-13]. In a previous clinical study, intraoperative knee kinematics collected during passive ROM were indicative of TKR functional outcome at 2 years follow-up [14, 15]. It is the premise of this study that such kinematics can be used as model inputs in a computational model to discriminate functional outcomes based on calculated ligament tensions during simulated passive ROM. This is only a viable approach if model calculations are sensitive to clinically observed variations in passive kinematics.

The purpose of this study was to determine the sensitivity of model calculated ligament tensions to variations in knee kinematics collected during passive ROM from TKR patients with good and poor functional outcomes. The workflow for this study involved acquiring anatomical geometry from an open source dataset and developing an unimplanted knee finite element model which was then validated against cadaver testing (Figure 4.1). This validated model served as the foundation for a subsequent TKR model simulating passive ROM using intraoperative kinematic data from the patient groups with good and poor functional outcomes. The integration of an open source dataset that included specimen-specific ligament parameters provided an improved modeling approach for using a generalized knee model with patient-specific inputs. Model sensitivity was quantified by comparing the calculated ligament tensions of the good function and poor function groups.

Methods

Completion of this study involved the development of two finite element (FE) models of the knee joint including an unimplanted natural knee model and a TKR knee model. The unimplanted knee model was validated against published *in vitro* cadaver data,

and served as the foundation for the TKR knee model used to input *in vivo* kinematics to simulate passive ROM.

Development of Passive Unimplanted Knee Finite Element Model

The unimplanted knee model was developed in ABAQUS/EXPLICIT (Simulia, Providence, RI) [16, 17] from an open source dataset (SimTK.org) using specimen-specific 3D anatomical geometry reconstructions of the proximal femur, proximal tibia, femoral cartilage, tibial cartilage, patella and patellar cartilage, ligament attachment sites, and tibiofemoral kinematic and load data collected during *in vitro* laxity testing (Figure 4.1)[18]. The bony anatomy of the knee was meshed using HYPERMESH software (Altair, Troy, MI) with rigid triangular shell elements (R3D3) [16, 19] and cartilage with eight-noded hexahedral elements (C3D8R) [19, 20]. Tibiofemoral cartilage contact was defined by a pressure-overclosure relationship [21].

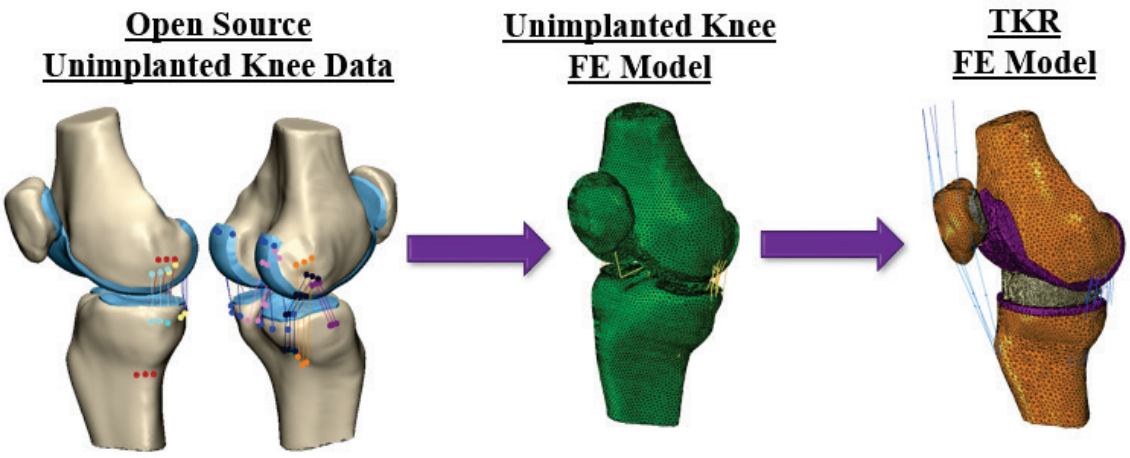

Figure 4.1. Schematic of the modeling workflow starting with open source data of an unimplanted knee model to the development of an unimplanted knee FE model and finally the adaption to a TKR FE model.

Nine soft tissue structures were represented in the unimplanted knee model (Table 4.1). These structures were chosen based on previous anatomic studies identifying soft-tissues critical to passive constraint of the knee joint [22-30]. The ACL was not included in the TKR model. Each soft tissue structure was represented by bundles of point-to-point, tension-only, nonlinear spring elements [31-34]. Specimen-specific reference strains and linear stiffness parameters were adopted from a previous study in which these parameters were calibrated to minimize differences in model and experimental kinematics during laxity tests performed on the same open source knee specimen described above [18]. As shown in Table 4.1, the MCL was modeled as three separate springs representing the anterior (MCLa), middle (MCLm), and posterior (MCLp) portions of the superficial MCL in order to cover the large insertion area. The PCL was also divided into the anterolateral PCL and posteromedial PCL each composed of two springs. The POL was modeled with two springs, the PFL with three springs in series to replicate the interaction with the popliteus tendon and the remaining ligaments were each modeled with three springs between femur and tibia attachment sites. In addition, the patellar tendon (PT) was represented with four spring elements exhibiting nonlinear force-displacement behavior in agreement with experimental tensile testing [35], and the quadriceps tendon (QT) as four connector elements with a distributed 40N tensile load applied (compared to 1500-4000N range experienced during daily activities) in order to keep the QT taut during passive range of motion and allow the patella to track physiologically without inducing significant forces across the joint.

Table 4.1. List of ligaments represented in the FE model with the number of spring elements used and corresponding stiffness and reference strain parameters implemented to define ligament behavior.

Ligaments	Acronym	# of Springs	Ligament Stiffness [N/mm]	Reference Strain
1) Superficial Medial Collateral				
Anterior	MCLa	1	149	1.07
Middle	MCLm	1	149	1.07
Posterior	MCLp	1	149	1.07
2) Deep Medial Collateral	DMCL	3	80	0.95
3) Posterior Oblique	POL	2	50	0.97
4) Lateral Collateral	LCL	3	197	1.05
5) Anterolateral Structure	ALS	3	36	0.75
6) Popliteofibular	PFL	3	31	0.9
7) Posterior Capsule				
Medial	PCm	3	90	1.06
Lateral	PCl	3	90	1.06
8) Posterior Cruciate				
Anterolateral	alPCL	2	36	1.06
Posteromedial	pmPCL	2	42	0.97
9) Anterior Cruciate				
Anteromedial	amACL	2	106	0.99
Posterolateral	plPCL	2	108	0.96

Validation of Unimplanted Knee Finite Element Model

The unimplanted knee model was validated against subject-specific laxity test. Local coordinate systems for the femur and tibia were established from digitized anatomical points provided in the open source dataset and defined within their respective rigid body reference frames. A tibiofemoral three-cylindrical open-chain coordinate system [18, 36] linked these local coordinate systems. The linkage was modeled with three

cylindrical connector elements representing the superior-inferior, anterior-posterior, and medial-lateral axes with the anterior-posterior axis as the floating axis [36]. Each cylindrical element provides translation along and rotation about the axis being represented. This allows for axial forces and torques to be applied to the axes and for the calculation of relative translations and rotations of the tibia relative to the femur in all six degrees of freedom (DOF) during simulation. Model validation was completed using published specimen-specific experimental kinematics measured during laxity tests imposing ±10 Nm varus-valgus (VV) torque, ±8 Nm internal-external (IE) torque, and ±50 N anterior-posterior (AP) force applied individually at knee flexions of 0°, 15°, 30°, 45°, and 60° [18]. The torques and forces were applied to the connector element representing the respective axis in the kinematic linkage, and corresponding rotations and translations output were recorded. The root mean square errors (RMSE) between model kinematics and experimental kinematics were calculated at 1 Nm or 10 N increments for each laxity test at each flexion angle and averaged for each individual test.

Development of TKR Knee Finite Element Model

Following validation, the unimplanted knee model was virtually implanted in neutral alignment with the same cruciate-retaining mobile-bearing TKR system used in the supporting clinical studies in order to develop the TKR model (Figure 4.2) [14, 15]. Neutral TKR component alignment was defined for the femoral component as 90° to the mechanical axis in the frontal and sagittal planes and parallel to the transepicondylar axis in the transverse plane, and for the tibial baseplate as 90° to the mechanical axis in the frontal plane, 5° posterior slope in the sagittal plane, and rotational alignment with the

medial third of the tibial tubercle in the transverse plane. Furthermore, the femoral component and tibial baseplate translational alignments were adjusted to match the ligament tensions of the unimplanted knee model at full extension and 90° flexion, similar to ligament balancing techniques practiced clinically.

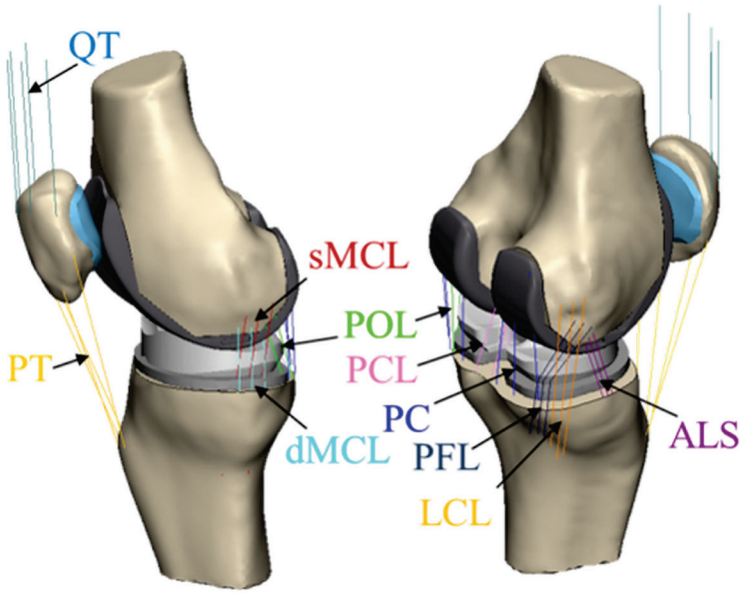

Figure 4.2. Virtual model of implanted knee with femoral component (dark grey), tibial baseplate (light grey) and mobile bearing tibial insert (white).

The femoral component and tibial baseplate geometries were meshed with rigid triangular shell elements and the tibial insert with eight-noded hexahedral elements using a previously verified mesh density with element lengths no greater than 0.9mm [16]. The tibial insert was assigned elastic material properties of UHMWPE (E=571 MPa, v=0.45)[16]. Contact between TKR components was defined using a penalty-based method with a weight factor and coefficient of friction of 0.04 [16, 17]. Following the same technique as the kinematic linkage described above, a three-cylindrical open chain

coordinate system [36] was modeled in order to link the local coordinate systems of the femoral component and tibial baseplate and to prescribe and record component relative motions for all six kinematic DOFs.

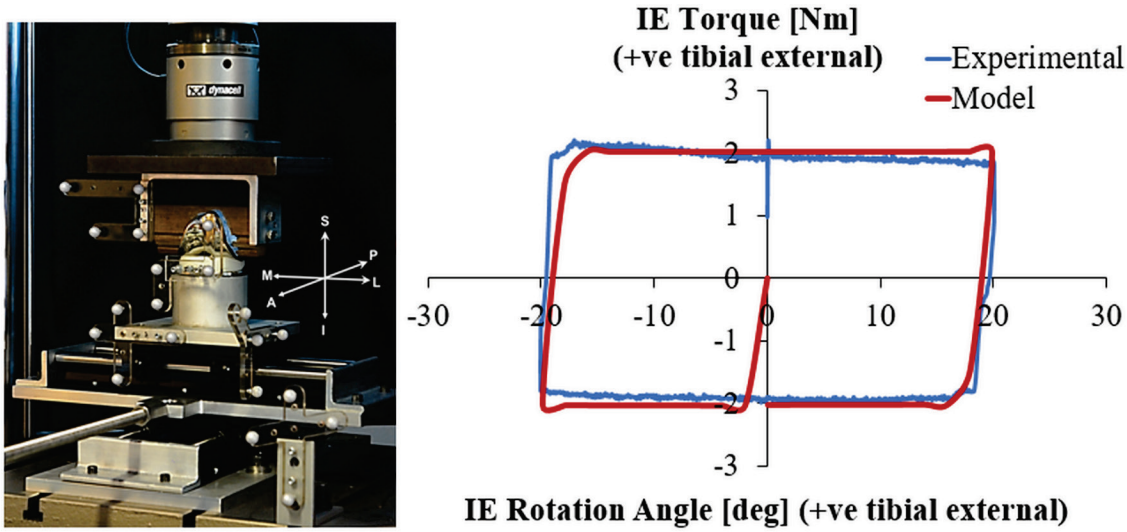

Figure 4.3. Experimental test setup for constraint testing performed to generate torque-rotation data to calibrated modeled mobile-bearing tibial insert behavior. Calibration curve shown for 60º knee flexion.

In the TKR model, the physical interface between the mobile-bearing tibial insert and the tibial baseplate was modeled with a hinge connector element to represent the rotating platform behavior of the insert. The modeled behavior of the connector was calibrated against experimental IE rotation constraint testing [37] performed on the same TKR system at 0º, 30º, 60º, and 90º of flexion. A Polaris Vicra (NDI, Ontario, Canada) optical tracking system tracked the axial rotation of the mobile-bearing while a servohydraulic test system (Instron Corp. Norwood, MA) simultaneously applied a 712N compressive load and ±20º of axial IE rotation and output axial torque (Figure 4.3). The

collected motion and torque data were synced in order to generate torque versus rotation curves at each flexion angle. The experimental IE constraint tests were reproduced in a finite element simulation of the isolated TKR components at each flexion angle. The damping and friction parameters of the connector behavior were calibrated resulting in an average RMSE between experimental and model torques of 0.17 Nm across all flexion angles (Figure 4.3).

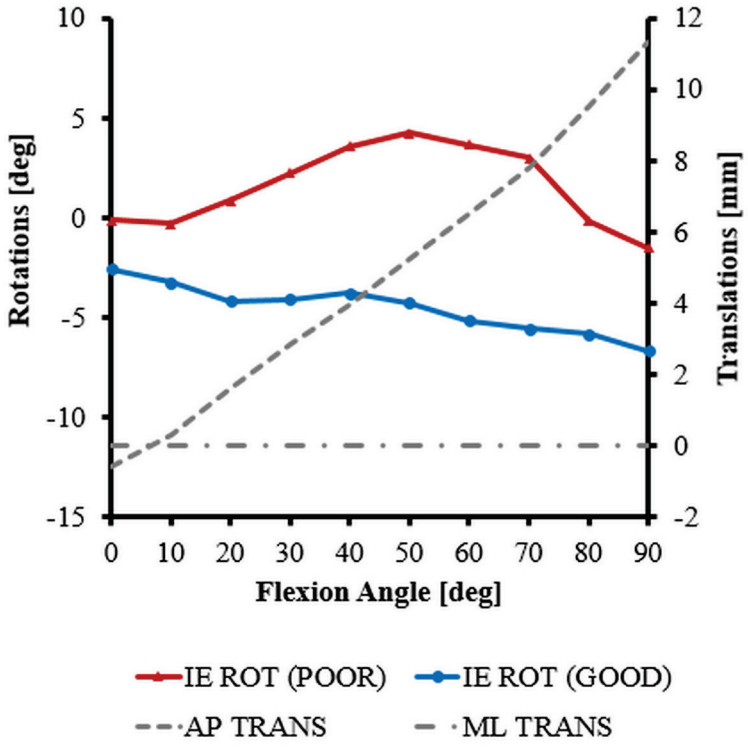

Figure 4.4. Averaged kinematics (rotations and translations) of the tibial baseplate relative to the femoral component for TKR patients with good and poor functional outcomes which were applied as model inputs to the kinematically-driven FE simulations.

Definition of Clinical Dataset

Tibiofemoral joint kinematic data for 67 TKR patients with cruciate-retaining, mobile-bearing components (Scorpio PCS, Stryker Orthopaedics) were obtained from single-plane fluoroscopic images acquired intraoperatively during passive ROM from 0°-120° flexion [14, 38]. The kinematic data provided measurement of the relative translation and rotation of the tibial baseplate relative to the femoral component in all six DOFs. The TKR patients were divided into two groups based on clinical evaluations performed over a two year follow-up interval using the Knee Society Score (KSS). A Good Function group included patients with greater than a 20 point improvement in Knee Society function scores at the two year evaluation, and a Poor Function group included patients with less than a 20 point improvement in Knee Society function scores at the two year evaluation. The Good Function group included 60 TKR patients and the Poor Function group included 7 TKR patients.

Model Loading and Boundary Conditions

In the current study, TKR kinematics served as model inputs. TKR kinematics for each kinematic DOF with respect to flexion angle were averaged for each patient group (Figure 4.4). It should be noted that the average kinematic profiles for the Good Function group and Poor Function group were nearly identical in all kinematic DOFs with the exception of IE rotation which demonstrated statistically significant differences and was determined to be indicative of functional outcomes in the supporting clinical study [14]. Thus, all kinematic profiles were kept the same between the Good Function and Poor Function groups except for IE rotation in order to isolate the sensitivity of the model to this

specific kinematic DOF. During model simulations, varus-valgus rotation was unconstrained in order to promote stable medial-lateral contact between the femoral component and tibial insert throughout the range of flexion, and a compressive 200N load was applied to the superior-inferior DOF.

Experimental Design of Study

The TKR model was run to complete two simulations of passive ROM. One simulation represented the Good Function group and the other simulation represented the Poor Function group. Simulations of Good Function and Poor Function were completed with the TKR components in neutral alignment and model inputs consisting of average kinematics measured during intraoperative passive ROM for each respective group. Model sensitivity was defined as the absolute percent difference in calculated ligament tension between the Good Function and Poor Function simulations for each ligament modeled from 0^{o}-70^{o} flexion. Percent difference calculations were not performed when tensions for a given ligament were <10N in either simulation to prevent artificially high percent difference calculations.

Results

The unimplanted knee model was validated against specimen-specific experimental laxity test. The average RMSE was less than 5.1 deg during IE rotations, less than 2.4 deg during VV rotations, and less than 2.3 mm during AP translation (Table 4.2). In general, errors in AP translation and VV rotation were smaller at lower flexion angles, and errors in IE rotation were smaller at higher flexion angles. The errors did not increase or decreases appreciably across the different flexion angles simulated for the VV, IE, or AP tests.

Torque-rotation and force-displacement profiles between the experiments and model simulations showed good agreement in trends (Figure 4.5).

Table 4.2. RMSEs (mean ±stdev) between experimental and model-predicted kinematics for the unimplanted knee model at each flexion angle and each DOF along with the range of motion (ROM) achieved during each laxity test.

Flexion Angle	Loading DOF	RMSE [ROM]
0°	AP (mm)	1.2 ± 0.8 [5.8]
	VV (deg)	0.5 ± 0.4 [3.2]
	IE (deg)	4.8 ± 2.9 [11.5]
15°	AP (mm)	0.5 ± 0.3 [8.3]
	VV (deg)	1.7 ± 1.0 [4.5]
	IE (deg)	5.1 ± 3.3 [18.7]
30°	AP (mm)	0.8 ± 1.0 [9.7]
	VV (deg)	2.1 ± 0.8 [4.5]
	IE (deg)	4.5 ± 2.7 [24.5]
45°	AP (mm)	1.5 ± 0.9 [9.5]
	VV (deg)	2.0 ± 0.7 [6.5]
	IE (deg)	2.7 ± 1.7 [28.0]
60°	AP (mm)	2.3 ± 2.0 [7.5]
	VV (deg)	2.1 ± 1.4 [7.2]
	IE (deg)	3.6 ± 2.3 [30.3]

There were notable differences in the calculated ligament tension profiles between the Good Function and Poor Function simulations. The Poor Function simulation generally resulted in higher ligament tension in lateral structures while the Good Function simulation resulted in higher ligament tension in the medial structures (Figure 4.6). Ligament tensions in the MCL, DMCL, and POL were higher in the Good Function TKR group. Ligament tension in the PFL was higher in the Poor Function TKR group.

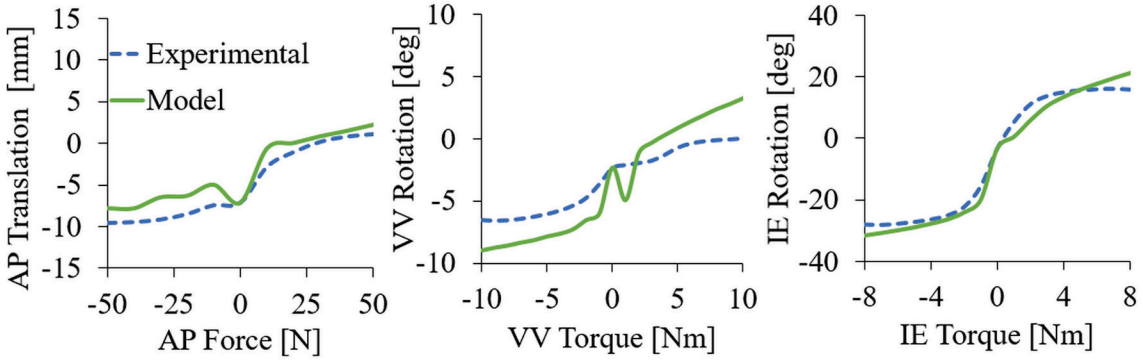

Figure 4.5. Experimental and model-predicted force-displacement and torque-rotation curves for AP, VV, and IE laxity tests at 45 deg flexion. Positive torque or force and positive rotation or displacement correspond with valgus, external and anterior.

The trend in medial and lateral ligament tensions can be attributed to the positive tibial external rotation exhibited by the Poor Function TKR group during the passive ROM (Figure 4.4). Correspondingly, initial engagement of the ligaments were offset by approximately 10° flexion when comparing the two simulations with the DMCL and POL engaging earlier in flexion in the Good Function simulation and the PFL engaging earlier in flexion in the Poor Function simulation (Figure 4.6). The MCLm, MCLp, ALS and LCL were not tense during the 0°-70° flexion range analyzed.

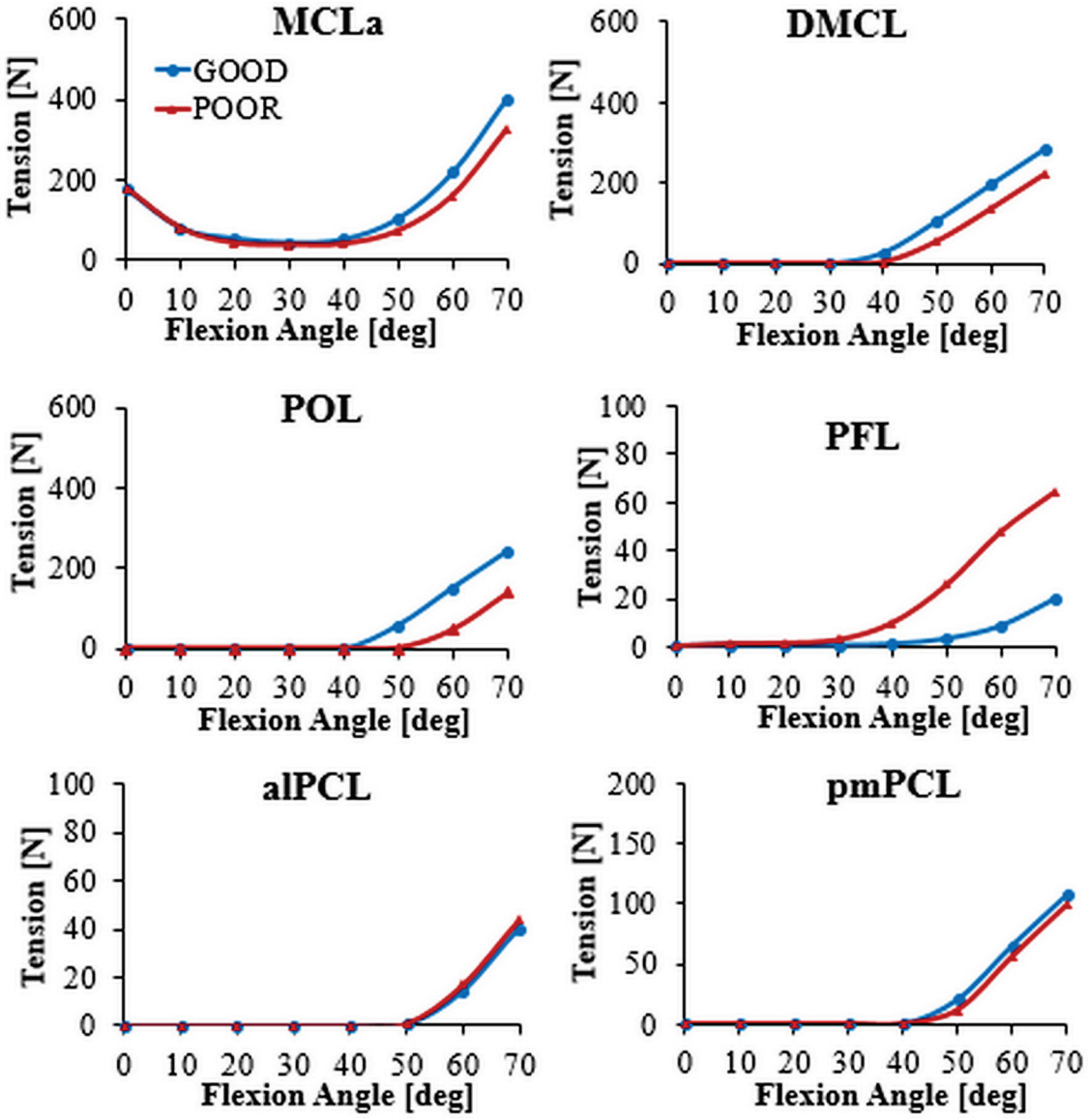

Figure 4.6. Individual ligament tension versus flexion angle during simulated passive ROM for both Good Function and Poor Function simulations under neutral TKR component alignment conditions.

The sensitivity of calculated ligament tensions to variation in kinematics between TKR patient groups with good and poor function varied across all the ligaments and the knee flexion range, but exhibited the greatest sensitivity to ligaments identified as primary

restraints to IE rotation and during mid-flexion. The average percent differences in calculated ligament tensions between the Good Function and Poor Function simulations ranged from 4% to 367% over the passive ROM (Table 4.3). The POL and PFL were the primary soft tissue restraints to IE rotation [39] exhibiting the greatest sensitivity with average percent differences of 55% and 367%, respectively. The MCL, also a primary soft tissue restraint, exhibited less sensitivity with average percent differences below 17%. The DMCL and PCL were the secondary soft tissue restraints exhibiting sensitivity with average percent differences of 32% and 25%, respectively. The maximum percent difference calculations followed similar trends, but notably the maximum sensitivity for each ligament occurred during the mid-flexion range of 30°-70°.

Table 4.3. Absolute % Difference calculations between Good Function and Poor Function simulations under neutral TKR component alignments from 0°-70° flexion.

Ligamentous Structure	IE Restraint	Average % Difference	Maximum % Difference	Flexion Angle (deg)
MCLp	Primary	5	5	0
MCLm	Primary	4	7	10
MCLa	Primary	17	30	50
POL	Primary	55	69	60
PFL	Primary	367	465	60
LCL	Primary	-	-	-
PCL	Secondary	25	48	60
DMCL	Secondary	32	72	70
ALS	Secondary	-	-	-

Discussion

This study used a TKR FE model to calculate ligament tensions during simulated intraoperative passive ROM for patient groups with good and poor functional outcomes. The TKR FE model was developed from an open source dataset and input *in vivo* kinematic data. The calculated ligament tensions demonstrated increased sensitivity to kinematic profiles indicative of good and poor function in the mid-flexion range where deviations in kinematics between the two groups were the greatest. The increased sensitivity in the flexion range clinically relevant to functional outcome demonstrates the ability of this modeling approach to discriminate patient outcomes based on output ligament tension. The inclusion of open source data in model development emphasizes this point in the context of a generalized knee model, a common modeling approach when simulating *in vivo* conditions.

The sensitivity of calculated ligament tensions varied in magnitude across the ligaments included in the model. However, the greatest sensitivity exhibited by all the ligaments occurred in the mid-flexion range of 30^{o}-70^{o}. This increased ligament tension sensitivity during mid-flexion agrees with the flexion range where statistically significant differences in IE rotation between the two patient groups occurred [38], and captures the mid-flexion instability noted clinically in the poor outcome TKR patients [14]. The literature lacks computational models that link model outputs to clinical outcomes; however, the unique kinematic dataset used in this study allowed model calculated ligament tension profiles to link with clinical outcomes.

Furthermore, since IE rotation between the two simulations was the only distinguishing factor, differences in ligament tension were attributed to the external tibia rotation exhibited by the Poor Function group and internal rotation exhibited by the Good Function group. This resulted in greater tension in the medial ligaments for the Good Function simulation and higher tension in the lateral ligaments for the Poor Function simulation. These trends in ligament tension are supported by cadaver laxity tests that have identified medial ligaments as primary restraints to internal rotation and lateral ligaments as primary restraints to external rotation [39]. Specifically, the MCL is a major resistor to internal rotational and to a lesser extent external rotation [25], the POL resists internal rotation [18], and the PFL resists external rotation [28, 40].

The behavior of the ligaments during the simulations agrees with experimental studies on cadaver limbs and other computational work. During the simulated passive ROM, some lateral soft tissue structures including the LCL and ALS remained lax during the mid-flexion range, and thus were not able to be included in the sensitivity analysis. This finding is supported by computational and experimental studies reporting a decreased role of the LCL to knee stability during flexion [18, 39, 41] and lack of engagement of the ALS until mid-flexion [18]. In contrast, the PFL maintains tension throughout flexion [42]. The tibial external rotation that occurred with the Poor Function simulation caused the PFL to engage earlier in flexion, but this was not captured in the percent difference calculations since PFL tension was still zero in the Good Function simulation. Additionally, the posterior capsule became lax as the knee flexed for both simulations which agrees with experimental observations [39].

The different magnitudes in ligament tensions measured for the Good Function and Poor Function simulations (Table 4.3) were within relevant ranges shown to alter TKR range of motion and contact mechanics. Quantification of ligament tension during TKR assessments have been limited to measurement of joint gaps [3, 4] and joint distraction forces [5, 6] which only provide a measure of global tension in the knee soft-tissues and have not been strongly correlated with postoperative outcomes [4-6]. Computational models can provide further detail on the individual role of ligaments during TKR assessments. Using patient-specific FE models, Oh, et al. simulated ligament balancing by reducing the MCL cross sectional area by 10-20% to effectively decrease ligament tension and correct uneven medial-lateral contact force distributions [43]. Steinbruck, et al. utilized a FE model to simulate PCL balancing by quantifying the effect of decreasing ligament stiffness by 50-75% had on range of motion and stress on the tibial insert during squat activity [44]. Given that ligament tension, ligament cross sectional area and ligament stiffness are directly proportional, these computational studies support that the percent changes reported herein for ligament tension are within relevant ranges shown to alter TKR performance during simulated ligament balancing. Additionally, tibiofemoral force has been measured *in vitro* during passive flexion and shown percent changes ranging from 30-150% for different insert thicknesses [45] further supporting the magnitudes of percent changes reported in this study despite being an indirect measurement of ligament tension.

The simulations in this study were kinematically-driven to make use of joint kinematics measured *in vivo*, which have been widely used for evaluating function in a variety of TKR designs [38, 46-55]. The VV rotation DOF was left unconstrained to allow

for stable medial-lateral contact between the femoral component and tibial insert throughout the simulated ROM as this would be difficult to achieve with all kinematic DOFs in motion-control due to the inherent error present in kinematic measurements. The VV DOF selected because it was not a distinguishing kinematic parameter for the two patient groups and previous studies have shown tibiofemoral contact is highly sensitive to kinematic measurement error in the VV DOF when under motion-control [56]. Furthermore, it should be noted that even if *in vivo* loads were available, it is difficult to accurately estimate kinematics in load-driven simulations without patient-specific ligament parameters and attachment sites [57]. In other words, a kinematically-driven model does not rely on the passive constraint of the soft tissues to drive joint motion as would a load-driven simulation of passive ROM. Thus, prescribing *in vivo* kinematics as inputs to simulate passive ROM provides a more robust approach for comparing between patients when patient-specific ligament details are unavailable.

The FE knee model includes several notable simplifications. Soft tissue structures were represented with one dimensional spring elements and did not include surface interaction between ligaments and the surrounding anatomy. This simplified representation provided computational efficiency and has shown to be suitable for simulating knee kinematics and acceptable for providing appropriate constraint [31, 34]. Furthermore, this representation was appropriate given the parameter of interest in this study was ligament tension and not internal ligament stresses. Similarly, the bone anatomy and implant components were modeled as rigid bodies to aid computational efficiency and was justified since deformation of these geometries were negligible.

A limitation to the FE knee model is that model validation was only completed between full knee extension and 60º flexion which matched the range of flexion used in the published specimen-specific experimental test data and associated ligament parameter calibrations [18]. Validation up to 60º flexion was appropriate for the scope of this study since the mid-flexion range demonstrated the greatest discrepancies in passive kinematics between the two patient groups and it captures the mid-flexion instability noted clinically in the poor function TKR patients [14].

The findings of this study should be interpreted in the context of neutral TKR component alignment used in both simulations in order to isolate ligament tension sensitivity to kinematic differences between the two patient groups. Previous computational studies have shown TKR component alignment affect ligament tensions in knee models [8-10, 32]. Future work will consider patient-specific TKR component alignments as well as the sensitivity of ligament tension to component alignment.

This study used open source models combined with *in vivo* kinematics as a powerful computational approach for estimating ligament tension profiles in different TKR patient populations. This approach recognizes that patient-specific anatomy and ligament parameters are commonly unknown in clinical datasets. The availability of specimen-specific calibrated ligament properties combined with experimental laxity test data from an unimplanted cadaver specimen allowed for a one-to-one model validation of the unimplanted knee model. Alternatively, many studies using patient data for model inputs define generalized ligament parameters based on published data not specific to the patients being simulated [7, 57-59]. The combination of specimen-specific ligament parameters

and in vitro cadaver testing from the open source dataset used in this study provided a more robust generalized knee model than used previously.

A potential application for the developed TKR model is to utilize existing intraoperative kinematic data to prescribe simulations and calculate ligament tensions to better inform surgeons of adequate ligament tensions during TKR. This application is enabled by clinical adoption of computer navigated surgery during TKA and development of novel intraoperative technologies for measuring intraoperative kinematics [11-14, 60]. However, very few studies have linked such kinematics to functional outcomes [14, 38] and it is unclear what surgeons should do to correct abnormalities in intraoperative kinematics [59]. A study by Mihalko et al. determined it was feasible to use *in vivo* kinematics measured from an intraoperative navigation system during TKR surgery and computational modeling to determine optimal TKR rotational alignments, and proposed the potential for providing personalized implant positioning for each patient [61]. This application is hindered by the lack of a clinically defined sensitivity threshold for ligament tension. In the current study, it is likely the model calculated ligament tension profiles were within clinically undetectable ranges. Integration of such data with intraoperative sensing technology could help surgeons address knee instability by providing enhanced sensitivity and the ability to detect subclinical abnormalities not detected solely by the surgeon [2, 62].

Conclusion

In summary, a FE model of the implanted knee was developed from validated specimen-specific open source data of an unimplanted knee and used to calculate ligament

tensions while simulating intraoperative kinematics during passive ROM. Model calculated ligament tensions were sensitive to variations in passive TKR kinematics and enabled discrimination of TKR patients groups with good and poor functional outcomes. Model behavior agreed with experimental cadaver tests and captured the mid-flexion instability noted clinically in the poor outcome TKR patients. The FE model was validated using calibrated ligament parameters and experimental data specific to a cadaveric specimen demonstrating the potential to utilize *in vivo* kinematics collected intraoperatively without knowledge of patient-specific anatomy or ligament properties. Application of this validated model could immediately impact surgical planning for revision TKR to correct ligament balance in the event of poor TKR function in the early follow-up interval, and has potential to inform technology innovation for more meaningful use of existing surgical tools for intra-operative sensing of soft tissue tension and knee motions during primary TKR.

References

[1] Schroer WC, Berend KR, Lombardi AV, Barnes CL, Bolognesi MP, Berend ME, Ritter MA, Nunley RM. Why are total knees failing today? Etiology of total knee revision in 2010 and 2011. Journal of Arthroplasty. 2013, 28(8 Suppl):116-119.

[2] Smith T, Elson L, Anderson C, Leone W. How are we addressing ligament balance in TKA? A literature review of revision etiology and technological advancement. Journal of Clinical Orthopaedics. 2016, 7: 248-255.

[3] Yagishita K, Muneta T, Ikeda H. Step-by-step measurements of soft tissue balancing during total knee arthroplasty for patients with varus knees. Journal of Arthroplasty. 2003, 18(3): 313-320.

[4] Watanabe T, Muneta T, Sekiya I, Banks SA. Intraoperative joint gaps and mediolateral balance affect postoperative knee kinematics in posterior-stabilized total knee arthroplasty. The Knee. 2015, http://dx.doi.org/10.1016/j.knee.2015.03.006.

[5] Asano H, Hoshino A, Wilton TJ. Soft-tissue tension total knee arthroplasty. Journal of Arthroplasty. 2004, 19(5): 558-561.

[6] Zalzal P, Papini M, Pertruccelli D, de Beer J, Winemaker MJ. An *in vivo* biomechanical analysis of the soft-tissue envelope of osteoarthritic knees. Journal of Arthroplasty. 2004, 19(2): 217-223.

[7] Guess TM, Razu S, Jahandar H. Evaluation of knee ligament mechanics using computational models. Journal of Knee Surgery. 2016, 29:126-137.

[8] Kuriyama S, Ishikawa M, Nakamura S, Furu M, Ito H, Matsuda S. Posterior tibial slope and femoral sizing afftect posterior cruciate ligament tension in posterior cruciate-retaining total knee arthroplasty. Clinical Biomechanics. 2015, 30: 676-681.

[9] Kang KT, Koh YG, Son J, Kwon OR, Baek C, Jung SH, Park KK. Measuring the effect of femoral malrotation on knee joint biomechanics for total knee arthroplasty using computational simulation. Bone & Joint Research. 2016, 5: 552-559.

[10] Thompson JA, Hast MW, Granger JF, Piazza SJ, Siston RA. Biomechanical effects of total knee arthroplasty component malrotation: a computational simulation. Journal of Orthopaedic Research. 2011, 29: 969-975.

[11] Omori G, Nishino K, Suzuki Y, Segawa H, Hayshi T, Koga, Y. Intraoperative measurements of knee motion in total knee arthroplasty. The Knee. 2003, 10: 75-79.

[12] Mihalko WM, Mounawar A, Phillips MJ, Bayers-Thering M, Krackow KA. Passive knee kinematics before and after total knee arthroplasty. Journal of Arthroplasty. 2008, 23(1): 57-60.

[13] Belvedere C, Ensini A, Leardini A, Dedda V, Feliciangeli A, Cenni F, Timoncini A, Barbadoro P, Giannini S. Tibio-femoral and patella-femoral joint kinematics during navigated total knee arthroplasty with patellar resurfacing. Knee Surgery, Sports Traumatology, Arthroscopy. 2014, 22:1719-1727.

[14] Lutzner J, Krischner S, Gunther KP, Harman MK. Patients with no functional improvement after total knee arthroplasty show different kinematics. International Orthopaedics. 2012, 36:1841-1847.

[15] Lutzner J, Krummenauer F, Wolf C, Gunther KP, Kirschner S. Computer-assisted and conventional total knee replacement. Journal of Bone and Joint Surgery. 2008, 90(8):1039-1044.

[16] Halloran JP, Petrella AJ, Rullkoetter PJ. Explicit finite element modeling of a total knee replacement mechanics. Journal of Biomechanics. 2005, 38:323-331.

[17] Godest AC, Beaugonin M, Haug E, Taylor M, Gegson PJ. Simulation of a knee joint replacement during gait cycle using explicit finite element analysis. Journal of Biomechanics. 2002, 35:267-275.

[18] Harris MD, Cyr AJ, Ali AA, Fitzpatrick CK, Rullkoetter PJ, Malestky LP, Shelburne KB. A combined experimental and computational approach to subject-specific analysis of knee joint laxity. Journal of Biomechanical Engineering. 2016, 138:081004-1.

[19] Fitzpatrick CK, Baldwin MA, Rullkoetter PJ. Computationally efficient finite element evaluation of natural patellofemoral mechanics. Journal of Biomechanical Engineering. 2010, 132:121013.

[20] Grosland NM, Bafina R, Magnotta VA. Automated hexahedral meshing of anatomic structures using deformable registration. Computer Methods in Biomechanics and Biomedical Engineering. 2009, 12: 35-43.

[21] Halloran JP, Easley SK, Petrella AJ, Rullkoetter PJ. Comparison of deformable and elastic foundation finite element simulations for predicting knee replacement mechanics. Journal of Biomechanical Engineering. 2005, 127(5):813-818.

[22] LaParde RF, Tso A, Wentorf FA. Force measurements on the fibular collateral ligament, popliteofibular ligament, and popliteus tendon to applied loads. American Journal of Sports Medicine. 2004, 32(7):1695-1701.

[23] Sugita T, Amis AA. Anatomic and biomechanical study of the lateral collateral and popliteofibular ligaments. American Journal of Sports Medicine. 2001, 29(4):466-472.

[24] Grood ES, Noyes FR, Butler DL, Suntay WJ. Ligamentous and capsular restraints preventing straing medial and lateral laxity in intact human cadaver knees. Journal of Bone and Joint Surgery. 1981, 63:1257-1269.

[25] Robinson JR, Bull AMJ, Thomas RRD, Amis AA. The role of the medial collateral ligament and posteromedial capsule in controlling knee laxity. American Journal of Sports Medicine. 2006, 34:1815-1823.

[26] Robinson JR, Sanchez-Ballester J, Bull AM, Thomas Rde W, Amis AA. The posteromedial corner revisited. An anatomical description of the passive restraining structures of the medial aspect of the human knee. Journal of Bone and Joint Surgery. 2004, 86(5):674-681.

[27] Claes S, Vereecke E, Maes M, Victor J, Verdonk P, Bellemans J. Anatomy of the anterolateral ligament of the knee. Journal of Anatomy. 2013, 223(4):321-328.

[28] Lim HC, Bae JH, Bae TS, Moon BC, Shyam AK, Wang JH. Relative role changing of lateral collateral ligament on the posterolateral rotatory instability according to the knee flexion angles: a biomechanical comparative study of role of lateral collateral ligament and popliteofibular ligament. Archives of Orthopaedic and Trauma Surgery. 2012, 132:1631-1636.

[29] Butler DL, Noyes FR, Grood ES. Ligamentous restraints to anterior-posterior drawer in the human knee- biomechanical study. Journal of Bone and Joint Surgery. 1980, 62:259-270.

[30] Petersen W, Loerch S, Schanz S, Raschke M, Zantop T. The role of the posterior oblique ligament in controlling posterior tribial translation in the posterior cruciate ligament-deficient knee. American Journal of Sports Medicine. 2008, 36: 495-501.

[31] Fitzpatrick CK, Komistek RD, Rullkoetter PJ. Developing simulations to reproduce *in vivo* fluoroscopy kinematics in total knee replacement patients. Journal of Biomechanics. 2014, 47:2398-2405.

[32] Fitzpatrick CK, Clary, CW, Laz PJ, Rullkoetter PJ. Relative contributions of design, alignment and loading variability in knee replacement mechanics. Journal of Orthopaedic Research. 2012, 30:2015-2024.

[33] Baldwin MA, Clary C, Maletsky LP, Rullkoetter PJ. Verification of predicted specimen-specific natural and implanted patellofemoral kinematics during simulated deep knee bend. Journal of Biomechanics. 2009, 42(14):2341-2348.

[34] Baldwin MA, Clary C, Fitzpatrick CK, Deacy JS, Maletsky LP, Rullkoetter PJ. Dynamic finite element knee simulation for evaluation of knee replacement mechanics. Journal of Biomechanics. 2012, 45:474-483.

[35] Staubli HU, Schatzmann L, Brunner P, Rincon L, Nolte LP. Mechanical tensile properties of the quadriceps tendon and patellar ligament in young adults. American Journal of Sports Medicine. 1999, 27(1):27-34.

[36] Grood ES, Suntay WJ. A joint coordinate system for the clinical description of three-dimensional motions: application of the knee. ASME. 1983, 105:136-144.

[37] ASTM F1223-14, Standard test method for determination of total knee replacement constraint, ASTM International, West Conshohocken, PA, 2014, www.astm.org.

[38] Harman MK, Banks SA, Kirschner S, Lützner J: Prosthesis alignment affects axial rotation motion after total knee replacement: A prospective *in vivo* study

combining computed tomography and fluoroscopic evaluations. BMC Musculoskeletal Disorders. 2012, 13(1):206-216.

[39] Athwal KK, Hunt NC, Davies AJ, Deehan DJ, Amis AA. Clinical biomechanics of instability related to total knee arthroplasty. Clinical Biomechanics. 2014, 29: 119-128.

[40] Veltri DM, Deng XH, Torzilli PA, Maynard MJ, Warren RF. The role of the popliteofibular ligament in stability of the human knee – a biomechanical study. American Journal of Sports Medicine. 1996, 24:19-27.

[41] Gollehon DL, Torzilli PA, Warren RF. The role of the posterolateral and cruciate ligaments in the stability of the human knee – a biomechanical study. Journal of Bone and Joint Surgergy. 1987, 69A: 233-242.

[42] Sugita T, Amis AA. Anatomic and biomechanical study of the lateral collateral and popliteofibular ligaments. American Journal of Sports Medicine. 2001, 29: 466-472.

[43] Oh Kj, Park WM, Kim K, Kim YH. Quantification of soft tissue balance in total knee arthroplasty using finite element analysis. Computer Methods in Biomechanics and Biomedical Engineering. 2014, 17 (14): 1630-1634.

[44] Steinbruck A, Woiczinski M, Weber P, Muller PE, Jansson V, Schroder C. Posterior cruciate ligament balancing in total knee arthroplasty: a numerical study with a dynamic force controlled knee model. Biomedical Engineering Online. 2014, 13:91.

[45] Schrim AC, Jeffcote BO, Nicholls RL, Jakob H, Kuster MS. Sensitivity of knee soft-tissues to surgical technique in total knee arthroplasty. The Knee. 2011, 18: 180-184.

[46] Kuroyanagi Y, Mu S, Hamai S, Robb WJ, Banks SA. In vivo knee kinematics during stair and deep flexion activities in patients with bicruciate substituting total knee arthroplasty. Journal of Arthroplasty. 2012, 27(1): 122-128.

[47] Tamaki M, Tomita T, Watanabe T, Yamazaki T, Yoshikawa H, Sugamoto K. In vivo kinematic analysis of a high-flexion, posterior-stabilized, mobile-bearing knee prosthesis in deep knee bending motion. Journal of Arthroplasty. 2009, 24(6): 972-978.

[48] Grieco TF, Sharma A, Komistek RD, Cates HE. Single versus multiple-radii cruciate-retaining total knee arthroplasty: an in vivo mobile fluoroscopy study. Journal of Arthroplasty. 2016, 31: 694-701.

[49] Ngai V, Wimmer MA. Kinematic evaluation of cruciate-retaining total knee replacement patients during level walking: a comparison with the displacement-controlled ISO standard. Journal of Biomechanics. 2009, 42: 2363-2368.

[50] Okamoto N, Nakamura E, Nishioka H, Karasugi T, Okada T, Mizuta H. In vivo kinematic comparison between mobile-bearing and fixed-bearing total knee arthroplasty during step-up activity. Journal of Arthroplasty. 2014, 29: 2393-2396.

[51] Moonot P, Shang Mu, Railton GT, Field RE, Banks SA. In vivo weight bearing kinematics with medial rotation knee arthroplasty. The Knee. 2010, 17:33-37.

[52] Moro-oka T, Muenchinger M, Canciani JP, Banks SA. Comparing in vivo kinematics of anterior cruciate-retaining and posterior cruciate-retaining total knee arthroplasty. Knee Surgery, Sports Traumatology, Arthroscopy. 2007, 15: 93-99.

[53] Banks SA, Fregly BJ, Boniforti F, Reinschmidt C, Romagnoli S. Comparing in vivo kinematics of unicondylar and bi-unicondylar knee replacements. Knee Surgery, Sports Traumatology, Arthroscopy. 2005, 13: 551-556.

[54] Banks SA, Markovich GD, Hodge AW. In vivo kinematics of cruciate-retaining and –substituting knee arthroplasties. Journal of Arthroplasty. 1997, 12(3): 297-304.

[55] Nakamura S, Sharma A, Ito H, Nakamura K, Komistek RD. In vivo femoro-tibial kinematic analysis of a tri-condylar total knee prosthesis. Clinical Biomechanics. 2014, 29: 400-405.

[56] Fregly BJ, Banks SA, D'Lima DD, Colwell Jr CW. Sensitivity of knee replacement contact calculations to kinematic measurement errors. Journal of Orthopaedic Research. 2008, 26:1173-1179.

[57] Tanaka Y, Nakamura S, Kuriyama S, Ito H, Furu M, Komistek RD, Matsuda S. How exactly can computer simulation predict the kinematics and contact status after TKA? Examination in individualized models. Clinical Biomechanics. 2016, 39:65-70.

[58] Fitzpatrick CK, Komistek RD, Rullkoetter PJ. Developing simulations to reproduce *in vivo* fluoroscopy kinematics in total knee replacement patients. Journal of Biomechanics. 2014, 47: 2398-2405.

[59] Mihalko WM, Conner DJ, Benner R, Williams JL. How does TKA kinematics vary with transverse plane alignment changes in a contemporary implant? Clinical Orthopaedics and Related Research. 2012, 470: 186-192.

[60] Koga Y. Three-dimensional motion analysis and its application in total knee arthroplasty: what we know, and what we should analyze. Journal of Orthopaedic Science. 2015, 20: 239-249.

[61] Mihalko WM, Williams JL. Total knee arthroplasty kinematics may be assessed using computer modeling: a feasibility study. Orthopedics. 2012 Oct, 35(10 Suppl): 40-44. doi: 10.3928/01477447-20120919-56.

[62] Wasielewski RC, Galat DD, Komistek RD. An intraoperative pressure-measuring device used in total knee arthroplasties and its kinematics correlations. Clinical Orthopaedics and Related Research. 2004, 427:171-178.

CHAPTER FIVE*

KNEE LIGAMENT TENSION DURING INTRAOPERATIVE PASSIVE RANGE OF MOTION DISCRIMINATES FUNCTIONAL OUTCOMES IN PATIENT-SPECIFIC FINITE ELEMENT MODELS

Introduction

Component malalignment and inadequate soft tissue balance after total knee replacement (TKR) contribute to approximately 50% of revisions within 5 years [1-3], and are recognized as preventable causes for revision at the time of operation [2, 4]. During TKR, intraoperative assessments of passive (non-weight bearing) range of motion (ROM) are routinely performed by the surgeon to assess knee stability and determine if proper TKR component alignment and soft tissue balance have been achieved [5, 6]. Previous studies demonstrated that mid-flexion kinematics during intraoperative passive ROM are significantly altered by component malalignment and predictive of poor functional outcomes at the two-year follow-up interval [7, 8]. However, intraoperative assessments of passive ROM do not generate quantitative feedback about ligament tension and studies linking passive ROM kinematics to TKR functional outcomes are rare. There is a need to establish quantitative relationships between ligament tension during passive ROM and clinical outcome.

*Results and data provided in this chapter were submitted for publication in:
Snethen K, Harman MK, Lutzner J, Yao H, Fitzpatrick C. Knee ligament tension during intraoperative passive ROM discriminates functional outcomes in patient specific FE models. Journal of Orthopaedic Research. Manuscript submitted and in review, 2018.

Computational modeling provides an approach to utilize kinematic data in order to calculate ligament tensions while simulating passive ROM. Cadaveric studies investigating the mechanical function of ligaments *in vitro* have either been limited to individual superficial soft tissues [9-11], or only provided global representation of the soft-tissue envelope as a whole [12-15]. Computational modeling can calculate individual ligament tension profiles for the numerous complex structures and discern the individual contribution each has to knee stability. Previous computational studies have quantified the effect of TKR component alignment on ligament tension, but have focused on weight-bearing activity and were not linked with functional outcome [16-18]. Accurate measurements of knee kinematics during intraoperative passive ROM combined with a computational modeling approach provides an opportunity to calculate ligament tensions while simulating passive ROM and inform TKR surgical assessments.

The objective of the current study was to determine ligament tension patterns that discriminate *in vivo* clinical outcomes in two TKR patient populations. It was hypothesized that ligament tension patterns predicted from patient-specific simulations would be significantly different for TKR patients with good functional outcomes versus poor functional outcomes. This study uses the TKR FE model adapted from a validated open source knee model in Chapter 4. The TKR FE model inputs patient-specific kinematic data to simulate intraoperative passive ROM for each TKR patient and outputs tension patterns for eight ligaments and soft tissue structures.

Methods

Description of Clinical Dataset

Two groups of TKR patients were identified using inclusion/exclusion criteria based on clinical outcomes (Knee society function scores or KSS) and TKR alignment (i.e. anatomic alignment and rotational mismatch) from a clinical dataset of 69 TKR patients implanted with cruciate-retaining, mobile-bearing components (Scorpio PCS, Stryker Orthopaedics) [8]. A Nominal Group included patients with improved knee function, defined as greater than a 20 point increase in KSS at the two-year evaluation, and rotational mismatch, defined as the angular divergence between the femoral and tibial components in the transverse plane, within $\pm 5^{o}$ (Table 5.1). An Outlier Group included patients with no improvement in knee function, defined as less than a 20 point increase in KSS, and rotational mismatch exceeding $\pm 10^{o}$ (Table 5.1). Additionally, the use of a generalized knee model to represent the unknown bone geometries and ligaments of the TKR patients required TKR component sizes to match the predefined bone dimensions. Available TKR patients meeting inclusion criteria resulted in a sample size of five patients for the Nominal Group and four patients for the Outlier Group (Table 5.1)

Tibiofemoral joint kinematic data from the nine TKR patients were previously obtained from single-plane fluoroscopic images acquired intraoperatively during passive ROM from 0°-120° flexion [7, 8]. The kinematic data provided measurement of the relative translation and rotation of the tibial baseplate relative to the femoral component in all six degrees of freedom (DOF) (Figure 5.1). In addition, TKR component alignment for each patient was obtained from long-leg radiographic and computed tomography (CT) images

captured within a week of the arthroplasty [8, 19] (Table 5.1). TKR component alignment was specified as both an anatomic rotational alignment, defined as the component rotational alignments relative to bone anatomic landmarks in the coronal, sagittal, and transverse planes, and rotational mismatch alignment, defined as the angular divergence between the femoral and tibial components in the transverse plane.

Table 5.1. Demographics and implant sizing for Outlier and Nominal patients chosen for patient-specific simulations. All Outlier patients exhibited no improvement in knee functional score and > 10° of rotational mismatch between femoral and tibial TKR components.

Group	#Side	Sex/Age	BMI	Sizes[1]	Outcome[2]	Limb[3]	F-rotation[4]	T-rotation[4]	Mismatch[5]
Outlier	47L	M/69	29.8	9/9/10	Not Improved	-5.9°	1.7°	-2.2°	10.6°
	65R	F/80	32.3	9/7/10		0.9°	3.2°	0.0°	12.7°
	60L	M/54	32.9	9/7/10		1.1°	0.8°	17.8°	14.1°
	4R	M/53	32.9	9/7/12		-0.2°	-1.1°	10.6°	14.4°
Nominal	63R	F/72	29.4	9/7/10	Improved	-2.6°	0.0°	0.5°	1.4°
	57R	M/63	33	9/9/10		-2.7°	0.1°	-4.4°	-3.7°
	21L	F/70	37	9/7/10		1.0°	2.3°	5.1°	-1.6°
	80L	F/70	30	9/7/10		-4.0°	2.3°	0.0°	3.3°
	51L	F/62	44	9/7/10		-2.9°	-2.1°	0.0°	4.6°

[1]Sizes of the femoral component, tibial component, polyethylene insert thickness, respectively.

[2]Based on the 0-100 point scale of Knee Society functional outcome score.

[3]Mechanical axis limb alignment after TKR, as measured from coronal long-leg radiographs.

[4]Anatomic rotational alignment of the femoral component (F-rotation) and tibial component (T-rotation) Negative = External rotation.

[5]Rotational mismatch alignment. Negative = Femoral external rotation relative to tibial.

Adaption of Finite Element TKR Model

The FE TKR model developed in Chapter 4, and implanted with the same cruciate-retaining, mobile-bearing TKR system as the TKR patients was used to complete patient-specific simulations of passive ROM. The FE TKR model was developed from an open-source

dataset of a generalized knee model, and the model behavior was validated against *in vitro* specimen-specific laxity test data. The FE TKR model consisted of femoral and tibia bones, TKR implant components, and eight ligaments and soft tissue structures. Bone anatomy and TKR components were represented by rigid bodies with the exception of a deformable UHMWPE tibial insert. Soft-tissue structures in the TKR knee model included the Anterolateral Structure (ALS), Posterior Capsule (PC), Lateral Collateral Ligament (LCL), Posterior Cruciate Ligament (PCL), superficial Medial Collateral Ligament (MCL), Deep Medial Collateral Ligament (DMCL), Popliteofibular Ligament (PFL), and Posterior Oblique Ligament (POL). Ligaments were represented by bundles of point-to-point, tension-only, nonlinear spring elements [20-22] with specimen-specific reference strains and linear stiffness parameters adopted from a previous study [23]. Additionally, the patellar tendon (PT) was represented by nonlinear springs and a 40N tensile load applied to the quadriceps tendon (QT) in order to allow the patella tor track physiologically during the passive ROM.

Model Loading and Boundary Conditions

The FE TKR model was developed for utilizing TKR kinematics and TKR component alignments as patient-specific inputs. Kinematics were prescribed using a three-cylindrical open chain coordinate system (Figure 5.2) [24] which linked the local coordinate systems of the femoral component and tibial baseplate and provided six DOFs. Additional linkages between each TKR component and the respective bone geometry were modeled to prescribe patient-specific component alignments in sagittal, transverse and coronal planes. Patient-specific passive ROM was simulated by prescribing the measured kinematics from the corresponding patient to the modeled open chain coordinate system in all DOFs except for

superior-inferior translation and varus-valgus rotation. A 200N compressive load was applied in the superior-inferior DOF and varus-valgus rotation was left unconstrained.

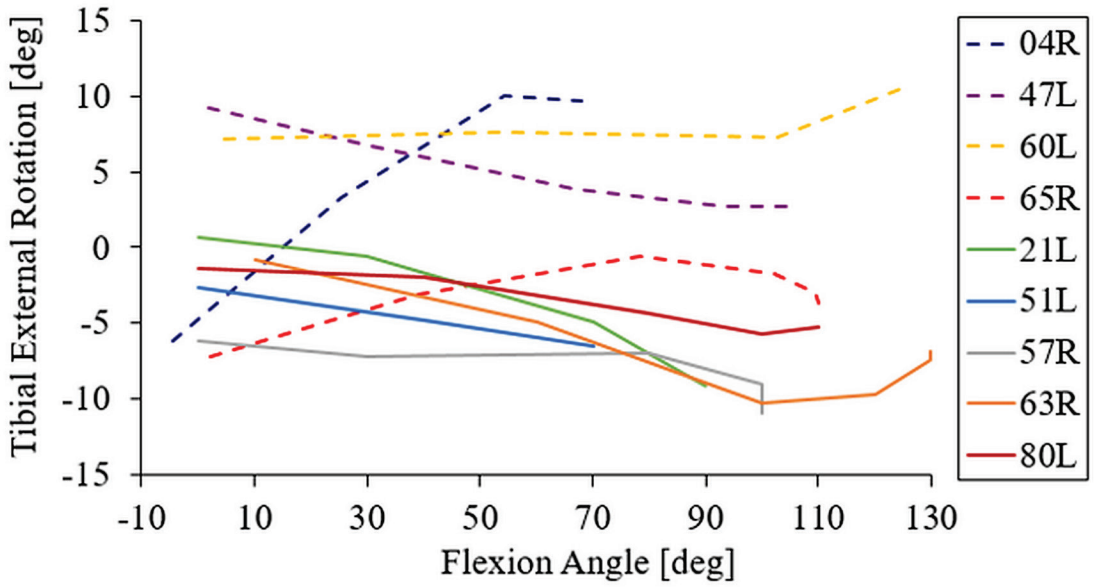

Figure 5.1. Tibial internal-external rotation measured during passive ROM for five Nominal Group patients (solid lines) and four Outlier Group patients (dashed lines). Passive kinematic profiles including internal-external rotation were prescribed as model inputs.

Model Sensitivity Study

Sensitivity of model calculated ligament tensions to measurement error in model inputs were systematically evaluated. Model inputs included joint kinematics and TKR component alignments which each exhibit inherent measurement error. Measurement error in single plane fluoroscopy and shape matching technique used to measure the *in vivo* joint kinematics was previously quantified as 0.3° for rotations and 1.0mm for translations [7]. Measurement error in femoral component rotational alignment was defined as 0.1° for each DOF, and in tibial

baseplate alignment as 0.3° for VV and FE DOFs and 0.1° and 0.6° for external and internal rotation, respectively [25-26]. Analysis of ligament tension sensitivity to kinematic measurement error involved individually simulating each variation in IE, ML, and AP kinematic DOFs in both the positive and negative orientations and required six simulations. Additionally, analysis of ligament tension sensitivity to measurement error in component rotational alignment involved individually simulating each variation in component alignment and required 12 simulations. Differences in ligament tension at every 10° flexion was calculated for each simulation with respect to the nominal simulation.

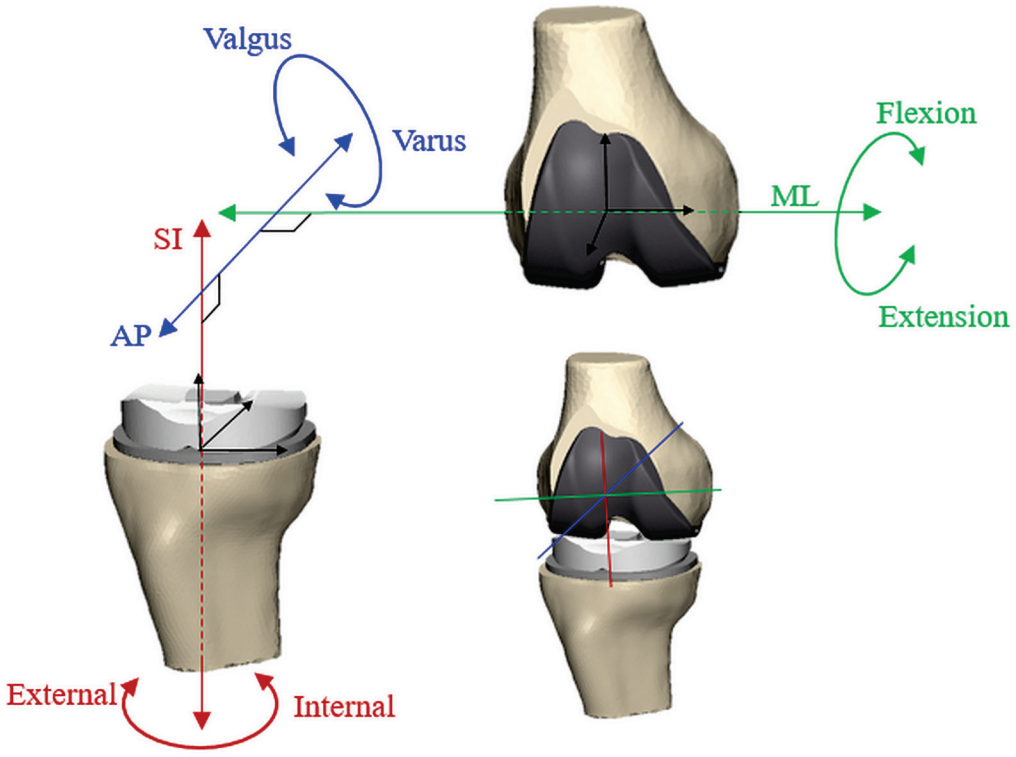

Figure 5.2. Schematic of the three-cylindrical open chain coordinate system which linked the local coordinate systems of the femoral component and tibial baseplate in order to prescribe six DOFs knee kinematics including varus-valgus, internal-external, and flexion-extension rotations and anterior-posterior (AP), superior-inferior (SI), and medial-lateral (ML) translations.

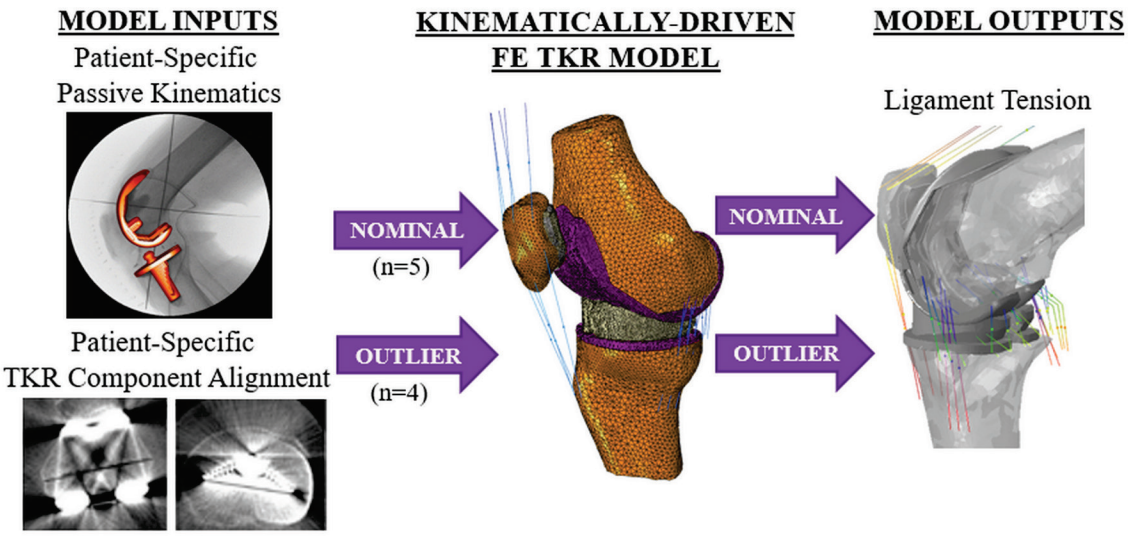

Figure 5.3. Schematic of the experimental design. Patient-specific kinematics and component alignments [21, 32] served as model inputs to the FE TKR model to calculate ligament tensions during simulated passive ROM of five Nominal Group and four Outlier Group patients.

Experimental Design of Study

The FE TKR model simulated passive ROM using data from each of the five Nominal Group patients and four Outlier Group patients resulting in a total of nine simulations. Model inputs for each simulation included patient-specific TKR component alignment and tibiofemoral kinematics (Figure 5.3). The model output ligament tension patterns over the passive ROM, consisting of the tension magnitudes for each flexion angle, were compared between the Nominal and Outlier Groups. For both the Nominal and Outlier groups, an average tension versus flexion angle curve was generated for each ligament by averaging the calculated tension at every 10° flexion from 0°-70° for all five simulations in the Nominal Group and all four simulations in the Outlier Group. A two-factor repeated measures analysis of variance (ANOVA) was performed in Minitab (Minitab Inc., State College, PA) to

determine if clinical outcome (patient grouping of Nominal or Outlier) and knee flexion angle were significant factors affecting the ligament tension patterns. Tukey's post-hoc pairwise comparisons were performed to compare the ligament tensions of the Nominal and Outlier groups at individual flexion angles. The level of significance was set at $p \leq 0.05$.

Results

The model calculated ligament tension was sensitive to inherent measurement error in prescribed kinematics and component alignment (Table 5.2). Model ligament tensions were the least sensitive to kinematic measurement error in IE rotation with an average percent change of 2% between the nominal and perturbed kinematic conditions. Model ligament tensions were more sensitive to kinematic measurement errors in AP and ML translation, with an average percent change of 26% and 16% between the nominal and perturbed kinematic conditions, respectively. Sensitivity to kinematics varied across the ligaments with the PFL, PCL and MCLm exhibiting the greatest sensitivities for IE rotation, AP translation, and ML translation, respectively. For measurement error in component rotational alignments, model ligament tensions demonstrated the greatest sensitivity to varus-valgus alignment but did not exceed 5% when averaged across all ligaments from 0^{o}-70^{o} flexion (Table 5.3). Sensitivity to component alignment also varied across the ligaments and flexion angles.

Based on the ligament tension patterns calculated during passive ROM, it was possible to differentiate the two functional outcomes groups (Figure 5.4, Figure 5.5). For the Nominal Group, the MCL was the only ligament to maintain tension throughout the passive ROM, whereas other medial structures (DMCL and POL) tensed from mid-flexion

to full flexion. The PFL was the only lateral structure to tense beyond full extension, while the ALS, LCL, and PCAP became lax in early flexion. The average ligament tension patterns for the Outlier group matched trends of the Nominal group with the exception of the LCL which maintained tension throughout the passive flexion range. As expected, the PCL became more tense with knee flexion for both the Nominal and Outlier Groups, with similar tension patterns over the passive ROM.

Table 5.2. Sensitivity of model calculated ligament tensions to measurement error in kinematic inputs during simulated passive ROM. Averaged and maximum percent change in output ligament tension to measurement errors in kinematic inputs.

Kinematic DOF	Measurement Error	Average % Change	Maximum % Change	Ligament	Flexion Angle
IE Rotation	±0.3°	2	20	PFL	60°
AP Translation	±1.0mm	26	158	PCL	40°
ML Translation	±1.0mm	16	143	MCLm	10°

Averaged ligament tension patterns were significantly higher for medial ligaments in the Nominal Group and significantly higher for lateral ligaments in the Outlier Group over the simulated passive ROM (Figure 5.5). This corresponded with initial engagement of the medial and lateral ligaments occurring at different flexion angles in each respective functional group. Most notably for the medial ligaments, the POL was recruited earlier in flexion and the PFL was recruited later in flexion for the Nominal Group compared to the Outlier Group. For the lateral ligaments, the PFL and ALS demonstrated significantly higher tension during mid-flexion (40°-70°) for the Outlier Group compared to the Nominal

Group (Figure 5.5). The LCL also demonstrated notable differences between the functional groups, especially beyond 20° flexion when the LCL becomes lax in the Nominal Group but remains tense in the Outlier Group; however, these were not statistically significant.

Table 5.3. Sensitivity of model calculated ligaments tensions to measurement error in TKR component alignments during simulated passive ROM. Averaged and maximum percent change in output ligament tension to measurement errors in TKR component alignment inputs.

Alignment DOF	Measurement Error	Average % Change	Maximum % Change	Ligament	Flexion Angle
Femoral IE	±0.1°	2	17	MCLa	30°
Femoral VV	±0.1°	2	40	PFL	70°
Femoral FE	±0.1°	1	5	DMCL	50°
Tibial IE	+0.1°, -0.6°	2	10	POL	60°
Tibial VV	±0.3°	5	26	PFL	70°
Tibial FE	±0.3°	2	15	MCLm	10°

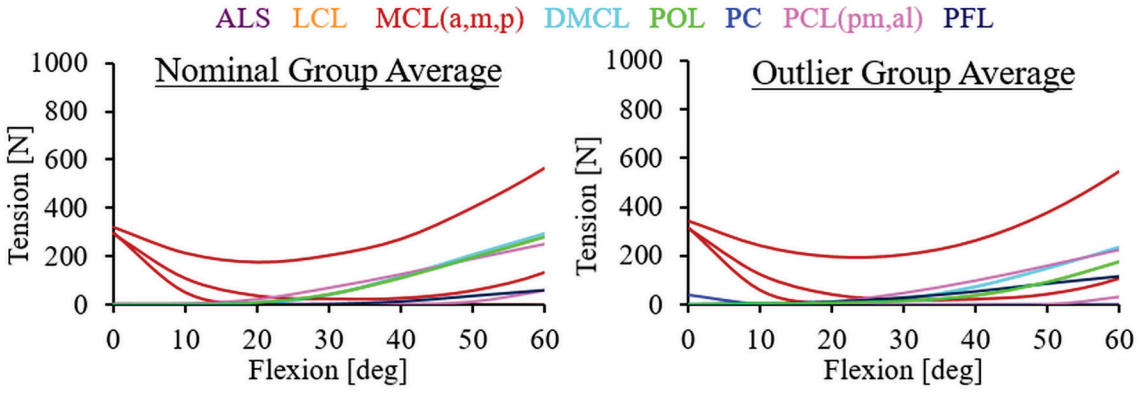

Figure 5.4. Averaged ligament tension patterns for the Nominal Patient Group (left) and Outlier Patient Group (right) during passive ROM. Ligament tensions were averaged for each ligament from patient-specific simulations of five Nominal and four Outlier patients.

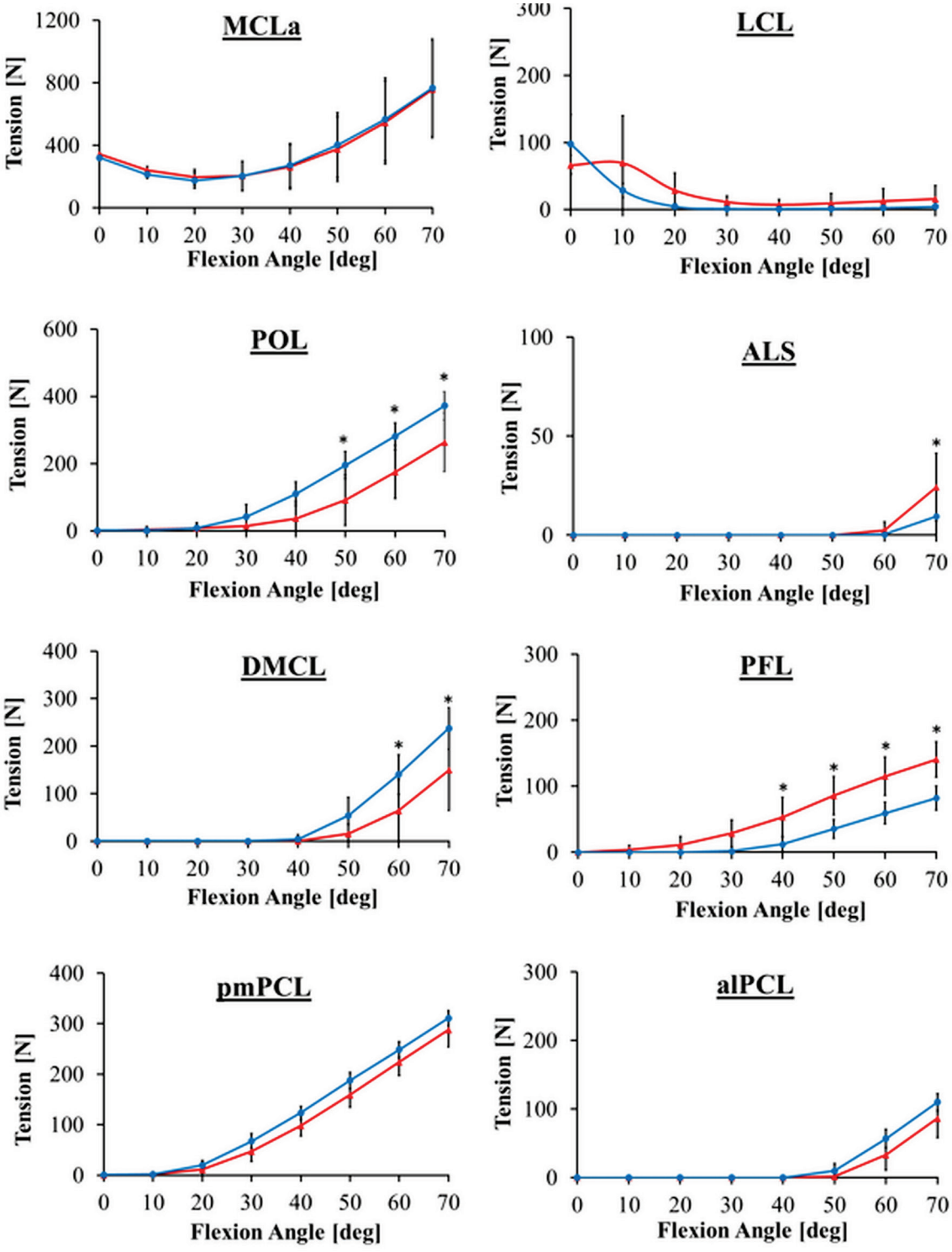

Figure 5.5. Comparison between average ligament tension patterns for the Nominal and Outlier Groups during passive ROM. Significant differences are symbolized by * (α=0.05).

Discussion

Using this validated FE TKR model and patient-specific component alignment and kinematic inputs, it was possible to discriminate functional outcomes in TKR patients based on the calculated ligament tensions during simulated passive ROM. The medial and lateral ligaments demonstrated distinct tension patterns as a result of differences in knee kinematics, which were previously shown to be indicative of functional outcomes at the two-year follow-up interval [8]. These results support the hypothesis that ligament tension patterns calculated during the patient-specific simulations were significantly different for TKR patients with good and poor functional outcomes.

The ligament tension patterns calculated for the Nominal and Outlier Groups were consistent with distinctions in the patient-specific model inputs. Knee kinematics and component rotational alignments prescribed as model inputs both exhibited distinctions in the IE rotational DOF. For knee kinematics, the Nominal Group exhibited tibial internal rotation during passive ROM and the Outlier Group exhibited tibial external rotation while all other kinematic DOFs showed nearly identical trends and magnitudes. Furthermore, the Outlier Group all exceeded 10^{o} positive rotational mismatch alignments (tibial component externally rotated relative to the femoral component), whereas the Nominal Group were within $\pm 5^{o}$ of rotational mismatch. Both of these conditions contribute to having a more externally rotated tibia relative to the femur in the Outlier Group compared to the Nominal Group. The trends in ligament tension patterns in the current study are supported by cadaveric laxity tests that have established the counteracting restraint the medial and lateral soft tissues provide to internal and external rotation, respectively [27].

Specifically, the medial ligaments resist tibial internal rotation and the lateral ligaments resist tibial external rotation which corresponds with the higher lateral ligament tensions in the Outlier Group and higher medial ligament tensions in the Nominal Group.

The intent of this study was to identify the ligaments exhibiting significant differences in tension between patients with good and poor functional outcomes in order to elucidate mechanisms contributing to poor function. Analysis of the calculated ligament tensions revealed significant differences in tensions for the DMCL, POL, PFL and ALS between the Nominal and Outlier Groups (Figure 5.5). Previous cadaveric studies have identified these ligaments as contributors to passive knee constraint during flexion [28-31]. In particular, the ligaments in the posteromedial corner (PFL and POL) are major stabilizers of the knee over the 0-90^{o} flexion range [28, 29]. The DMCL also contributes to passive restraint from 15-90^{o} flexion [30]. Similarly, cadaveric tests suggest the ALS provides constraint in the 30-90^{o} flexion range whereas the LCL only contributes at full extension [31].

Computational modeling has been used previously to simulate ligament balance in TKR, but with notable limitations. Steinbruck, et al. demonstrated PCL stiffness altered knee kinematics after TKR [32], and Zelle, et al. determined PCL behavior in TKR is sensitive to small variations in PCL mechanical and anatomic properties during simulated squat [33]. In the current study, insignificant differences were calculated in PCL tension between the Nominal and Outlier Groups. This was expected given that factors known to affect PCL tension where either identical or similar across all simulations including PCL mechanical properties, AP translation, and tibial component slope, and that the PCL is not

recognized as contributor to IE rotation constraint [27]. The effect of ligament release of the MCL and LCL on medial-lateral contact force imbalance was investigated by Oh, et al. through patient-specific FE TKR simulations of weight-bearing stance [34]. These studies support a computational approach for simulating ligament balance, but with notable limitations including representation of only the PCL, MCL, and LCL soft tissues, simulation under weight-bearing conditions, and no link to functional outcome. Although the PCL, MCL, and LCL are the most clinically relevant tissues to ligament balance during TKR, additional soft tissue structures contribute to knee constraint, especially during the passive loading conditions that exist intraoperatively [27]. The current study addresses these limitations by representing additional soft tissues critical to knee constraint and simulating passive ROM linked to functional outcome.

Analyzing intraoperative ligament tension through computational simulation provides an unrestricted approach compared to the limitations in assessing ligament tension during TKR surgery. Current standard techniques for intraoperative ligament manipulation focus on the medial and lateral collateral ligaments [35]. Discerning tensions in soft tissue structures embedded beneath the collaterals from manual feedback alone presents a great challenge, and even *in vivo* studies quantifying ligament balance during TKR only provide a global representation of medial and lateral ligament tension [12-15]. Additionally, soft tissue assessments are typically completed at full extension (0^o flexion) and 90^o flexion [35, 36], but proper balance at these two endpoints does not guarantee suitable ligament tensions within this flexion range [37]. The FE TKR model calculated ligament tensions for eight soft-tissue structures over a full ROM providing additional information to

surgeons than currently obtained during TKR surgery. Given that ligament tension is not directly measured during surgery, model calculated ligament tensions could be integrated with currently used intraoperative sensing devices to detect subclinical abnormalities [38]

The model calculated ligament tensions were largely insensitive to measurement errors in most of the model inputs, specifically component alignment and kinematics. In particular, the FE model was least sensitive to errors in IE rotation and axial (IE) component alignment DOFs, which were the model inputs exhibiting the most distinct differences between the Nominal and Outlier Groups. Maximum sensitivities of the PFL and POL to those DOFs were deemed negligible. The FE TKR model was most sensitive to measurement errors in AP and ML translations, but these were nearly identical amongst the Nominal and Outlier Groups. The PCL and MCLm were the ligaments most affected by those errors, and thus, did not substantially influence the reported findings. Similarly, the PFL was most affected by varus-valgus component alignment error, especially at 70^{o} flexion, but this was not a distinguished attribute between the Nominal and Outlier Groups and not a substantial influence on the results. Furthermore, the sensitivities reported were at the outer bounds of measurement error, and it is expected that actual measurement error would be less for a given model input.

The main limitation to the TKR knee model lies in the representation of the soft tissue structures. Ligament parameters and attachment sites were constant across all FE simulations despite acknowledging ligament properties vary across patient populations. The calibrated parameters used in the model validation were implemented for all subsequent models, as additional data to inform patient-specific ligament properties were

unavailable. The use of a kinematically-driven simulation instead of a load-driven simulation helps mitigate this uncertainty because the ligament properties only influence the output ligament tension. In a kinematically-driven approach, ligament tension is a response to joint motion that is prescribed, whereas in a load-driven approach, ligament tension constrains joint motion in addition to being a response to applied external loading which would therefore be difficult to accurately simulate without assigning patient-specific ligament properties. Although variation in ligament properties is still expected to influence the calculated ligament tensions, the current study benefited from a kinematically-driven approach in that any distinctions in ligament tensions between the Nominal and Outlier Groups were only attributed to patient-specific inputs (TKR alignment and kinematics) that were statistically distinguishing factors between the two groups [7].

Conclusion

In summary, using this validated FE TKR model, it was possible to discriminate TKR patients with good and poor functional outcomes based on calculated ligament tensions during simulated passive ROM with patient-specific inputs. The FE TKR model demonstrated the ability to analyze more complex knee ligaments than possible *in vitro* or *in vivo* and provided subclinical details regarding ligament tension. Although current ligament balancing techniques focus on the collateral ligaments, this study identified the DMCL, POL, PFL and ALS as ligaments with tension patterns that could distinguish between patients with good and poor functional outcomes. Given the increase in intraoperative kinematic data becoming available, this computational approach could

further link ligament tensions during intraoperative assessments to functional outcomes after TKR.

References

[1] Babazadeh S, Stoney JD, Lim K, Choong FM. The relevance of ligament balancing in total knee arthroplasty: how important is it? A systematic review of the literature. Orthopedic Reviews. 2009, 1:e26.

[2] Smith T, Elson L, Anderson C, Leone W. How are we addressing ligament balance in TKA? A literature review of revision etiology and technological advancement. Journal of Clinical Orthopaedics and Trauma. 2016, In Press.

[3] Dalruy DF, Pomery DL, Gorab RS, Adams MJ, BSN. Why are total knee arthroplasties being revised? Journal of Arthroplasty. 2013, 28(Suppl. 1): 120-121.

[4] Fehring TK, Odum S, Griffin WL, Mason JB, Nadaud M. Early failures in total knee arthroplasty. Clinical Orthopaedics and Related Research. 2001, 392:315-18.

[5] Le DH, Goodman SB, Maloney WJ, Huddleston JI. Current mode of failure in TKA: Infection, instability, and stiffness predominate. Clinical Orthopaedics and Related Research. 2014, 472:2197-2200.

[6] Schroer WC, Berend KR, Lombardi AV, Barnes CL, Bolognesi MP, Berend ME, Ritter MA, Nunley RM. Why are total knees failing today? Etiology of total knee revision in 2010 and 2011. Journal of Arthroplasty. 2013, 28(8 Suppl):116-119.

[7] Harman MK, Banks SA, Kirschner S, Lützner J: Prosthesis alignment affects axial rotation motion after total knee replacement: A prospective *in vivo* study

combining computed tomography and fluoroscopic evaluations. BMC Musculoskeletal Disorders. 2012, 13(1):206-216.

[8] Lutzner J, Krischner S, Gunther KP, Harman MK. Patients with no functional improvement after total knee arthroplasty show different kinematics. International Orthopaedics. 2012, 36:1841-1847.

[9] Gardiner JC, Weiss JA, Rosenberg TD. Strain in the human medial collateral ligament during valgus loading of the knee. Clinical Orthopaedics and Related Research. 2001, 391:266-274.

[10] Halewood C, Risebury M, Thomas NP, Amis AA. Kinematic behavior and soft tissue management in guided motion total knee replacement. Knee Surgery, Sports Traumatology, Arthroscopy. 2014, 22:3074-3082.

[11] Ghosh KM, Merican AM, Iranpour F, Deehan DJ, Amis AA. Length-change patterns of the collateral ligaments after total knee arthroplasty. Knee Surgery, Sports Traumatology, Arthroscopy. 2012, 20:1349-1356.

[12] Yagishita K, Muneta T, Ikeda H. Step-by-step measurements of soft tissue balancing during total knee arthroplasty for patients with varus knees. Journal of Arthroplasty. 2003, 18(3): 313-320.

[13] Watanabe T, Muneta T, Sekiya I, Banks SA. Intraoperative joint gaps and mediolateral balance affect postoperative knee kinematics in posterior-stabilized total knee arthroplasty. The Knee. 2015, http://dx.doi.org/10.1016/j.knee.2015.03.006.

[14] Asano H, Hoshino A, Wilton TJ. Soft-tissue tension total knee arthroplasty. Journal of Arthroplasty. 2004, 19(5): 558-561.

[15] Zalzal P, Papini M, Pertruccelli D, de Beer J, Winemaker MJ. An *in vivo* biomechanical analysis of the soft-tissue envelope of osteoarthritic knees. Journal of Arthroplasty. 2004, 19(2): 217-223.

[16] Thompson JA, Hast MW, Granger JF, Piazza SJ, Siston RA. Biomechanical effects of total knee arthroplasty component malrotation: a computational simulation. Journal of Orthopaedic Research. 2011, 29:969-975.

[17] Kuriyama S, Ishikawa M, Nakamura S, Furu N, Ito H, Matsuda S. Posterior tibial slope and femoral sizing affect posterior cruciate ligament tension in posterior cruciate-retaining total knee arthroplasty. Clinical Biomechanics. 2015, 30:676-681.

[18] Kang KT, Koh YG, Son J, Kwon OR, Baek C, Jung SH, Park KK. Measuring the effect of femoral malrotation on knee joint biomechanics for total knee arthroplasty using computational simulation. Bone & Joint Research. 2016, 5:552-559.

[19] Lutzner J, Krummenauer F, Wolf C, Gunther KP, Kirschner S. Computer-assisted and conventional total knee replacement. Journal of Bone and Joint Surgery. 2008, 90(8):1039-1044.

[20] Fitzpatrick CK, Komistek RD, Rullkoetter PJ. Developing simulations to reproduce *in vivo* fluoroscopy kinematics in total knee replacement patients. Journal of Biomechanics. 2014 47:2398-2405.

[21] Fitzpatrick CK, Clary, CW, Laz PJ, Rullkoetter PJ. Relative contributions of design, alignment and loading variability in knee replacement mechanics. Journal of Orthopaedic Research. 2012, 30:2015-2024.

[22] Baldwin MA, Clary C, Maletsky LP, Rullkoetter PJ. Verification of predicted specimen-specific natural and implanted patellofemoral kinematics during simulated deep knee bend. Journal of Biomechanics. 2009, 42(14):2341-2348.

[23] Harris MD, Cyr AJ, Ali AA, Fitzpatrick CK, Rullkoetter PJ, Malestky LP, Shelburne KB. A combined experimental and computational approach to subject-specific analysis of knee joint laxity. Journal of Biomechanical Engineering. 2016, 138:081004-1.

[24] Grood ES, Suntay WJ. A joint coordinate system for the clinical description of three-dimensional motions: application of the knee. ASME. 1983, 105:136-144.

[25] Victor J, Doninck DV, Labey L, Innocenti B, Parizel PM, Bellemans J. How precise can bony landmarks be determined on a CT scan of the knee? The Knee. 2009, 16: 358-365.

[26] Jazrawi LM, Birdzell L, Kummer KJ, Di Cesare PE. The accuracy of computed tomography for determining femoral and tibial total knee arthroplasty component rotation. Journal of Arthroplasty. 2000, 15(6): 761-766.

[27] Athwal KK, Hunt NC, Davies AJ, Deehan DJ, Amis AA. Clinical biomechanics of instability related to total knee arthroplasty. Clinical Biomechanics. 2014, 29: 119-128.

[28] Sugita T, Amis AA. Anatomic and biomechanical study of the lateral collateral and popliteofibular ligaments. American Journal of Sports Medicine. 2001, 29: 466-472.

[29] Petersen W, Loerch S, Schanz S, Raschke M, Zantop T. The role of the posterior oblique ligament in controlling posterior tribial translation in the posterior cruciate ligament-deficient knee. American Journal of Sports Medicine. 2008, 36: 495-501.

[30] Robinson JR, Bull AMJ, Thomas RRD, Amis AA. The role of the medial collateral ligament and posteromedial capsule in controlling knee laxity. American Journal of Sports Medicine. 2006, 34:1815-1823.

[31] Claes S, Vereecke E, Maes M, Victor J, Verdonk P, Bellemans J. Anatomy of the anterolateral ligament of the knee. Journal of Anatomy. 2013, 223(4):321-328.

[32] Steinbruck A, Woiczinski M, Weber P, Muller PE, Jansson V, Schroder C. Posterior cruciate ligament balancing in total knee arthroplasty: a numerical study with a dynamic force controlled knee model. BioMedical Engineering OnLine. 2014, 13:91.

[33] Zelle J, Heesterbeek PJ, de Waal MM, Verdonschot N. Numerical analysis of variations of posterior cruciate ligament properties and balancing techniques on total knee arthroplasty loading. Medical Engineering & Physics. 2010, 32:700-707.

[34] Oh Kj, Park WM, Kim K, Kim YH. Quantification of soft tissue balance in total knee arthroplasty using finite element analysis. Computer Methods in Biomechanics and Biomedical Engineering. 2013, doi:10.1080/10255842.10252013.10765409.

[35] Bottros J, Gad B, Krebs V, Barsoum WK. Gap balancing in total knee arthroplasty. Journal of Arthroplasty. 2006, 21(4) Suppl. 1: 11-15.

[36] Vince KG, Abdeen A, Sugimoi T. The unstable total knee arthroplasty. Journal of Arthroplasty. 2006, 21(4) Suppl. 1: 44-49.

[37] D'Lima DD, Patil S, Steklov N, Colwell CW. Dynamic intraoperative ligament balancing for total knee arthroplasty. Clinical Orthopaedics and Related Research. 2007, 463: 208-212.

[38] Wasielewski RC, Galat DD, Komistek RD. Correlation of compartment pressure data from an intraoperative sensing device with postoperative fluoroscopic kinematic results in TKA patients. Journal of Biomechanics. 2005, 38: 333-339.

CHAPTER SIX

VALIDATION OF A FORCE-DRIVEN TKR MODEL TO SIMULATE INTRAOPERATIVE PASSIVE RANGE OF MOTION

Introduction

A successful total knee replacement (TKR) requires both proper resection of bone tissue for optimal component alignment and proper handling of the soft-tissues surrounding the knee joint, referred to clinically as ligament balance [1]. Knee instability, arthrofibrosis, and component malalignment alone account for approximately 50% of early revisions [2,3], and are recognized as preventable causes for revision at the time of surgery [1, 3, 4]. During the TKR procedure, surgeons routinely put the knee through passive range of motion (ROM) in order to determine if proper TKR component alignment and ligament balance have been achieved. The influence of TKR component alignment and ligament balance on the mechanical environment of the knee is poorly understood due to a lack in intraoperative quantitative measures. Computational studies have demonstrated that TKR component alignment affects ligament tensions during weight bearing activity [5-8]. However, this relationship has not been quantified during passive ROM. A validated force-driven passive knee model capable of simulating passive ROM for various TKR alignment conditions could quantify the relationship between intraoperative ligament tensions and TKR component alignment.

Common practice for validating computational knee models requires experimentally measured external loading, corresponding kinematic data, and specimen-

specific imaging data. Previous experimental studies investigating knee joint mechanics have utilized various measurement techniques to obtain this data including optical motion capture systems or fluoroscopy for limb and TKR component motions and in-floor force plates or load cells for quantifying external loads [9-13]. These measurement techniques have been adapted into experimental test knee rigs which provide a repeatable testing environment optimal for validation of computational knee models [14-16]. Current knee models are validated with force-driven cadaveric knee rigs that actuate the quadriceps to replicate dynamic weight-bearing activities, and for this reason do not represent the intraoperative scenario [9, 13-16]. Previous studies developed passive knee rigs using similar technology, but were limited to joint laxity studies [17-19] with the exception of a knee rig developed by Anglin, et al. to simulate intraoperative passive ROM [20]. This study, however, was strictly experimental and consequently lacked key information to develop a specimen-specific computational model for one-to-one validation including imaging data and measured external loading [20]. The data necessary to validate a force-driven knee model simulating passive ROM is currently unavailable.

The purpose of this study was to quantify loads applied during intraoperative passive ROM and validate a force-driven computational simulation of passive ROM. To complete this aim, *in vitro* biomechanical testing was completed on an implanted cadaveric knee specimen and subsequently a specimen-specific TKR knee model was developed and validated against the measured experimental data. Applied external loads and passive kinematics were measured during experimentally simulated passive ROM in order to provide boundary conditions (external loads) for the force-driven computational simulation

and kinematic data to validate model outputs against. A validated force-driven model provides an efficient approach to simulate different TKR alignment conditions and quantify the relationship between component alignments and ligament tension during passive ROM assessments. Quantifying these relationships will improve the objectivity of intraoperative assessments.

Methods

The workflow of the current study consists of both experimental and computational elements. A custom-designed mechanical knee rig was used to experimentally simulate passive ROM on an implanted cadaver knee specimen while measuring external loads applied and joint kinematics. Subsequently, a specimen-specific, force-driven TKR model was developed and validated with the experimental data to analyze ligament tensions during simulated passive ROM. Experimental and computational simulations were completed for three different TKR component alignment conditions.

Surgical Implantation of TKR Components in Neutral Alignment

A fresh-frozen lower limb 94 year-old female specimen was used for the experimental simulations. Severe osteoarthritis was noted on the lateral side of the left knee specimen. The specimen was implanted with modified components of a mobile-bearing cruciate-retaining TKR design (Scorpio PCS, Stryker) by experienced orthopaedic surgeons. The femoral component was cemented onto the distal end of the femur and the tibial baseplate secured to the tibial plateau with metal screws. The patella was not resurfaced. A neutral baseline alignment was defined as the preferred component alignment based on surgical assessment post-implantation in both flexion and extension

and the surgeons' discretion. Sagittal, coronal, and axial rotational alignments for the neutral baseline were 0.4° flexion, 4.3° varus, and 1.7° external for the femoral component and 8.1° tibial slope, 8.1° valgus, and 7.4° internal for the tibial baseplate, respectively. A 2.3° rotational mismatch, defined as the angular divergence between the femoral and tibial components in the transverse plane, was measured for neutral alignment from long leg computed tomography (CT) of the TKR knee specimen near full extension [21]. The axial rotational alignment of the tibial baseplate was varied ±15° from the neutral baseline in both the internal and external directions to represent three different alignment conditions (neutral, external, and internal). The tibia and femur were amputated at the mid-diaphysis and a stainless steel threaded rod (6-32 thread) was cemented into the intramedullary canal of each bone at a length that recreated the limb length from the articular surface of the ankle to the center of the femoral head. The uncemented ends of the threaded rods interfaced with the mechanical linkages on the knee rig. Fiducial markers were implanted onto the bone anatomy to identify key anatomic landmarks on the superior, inferior, medial, and lateral aspects of the femur and tibia bones.

Modification of TKR Components for Rotational Alignment Incrementation

TKR components were modified in order to allow for easy manipulation of rotational alignment relative to the bone. Physical TKR components of a mobile-bearing cruciate retaining TKR system (Scorpio PCS, Stryker) were 3D scanned to generate virtual geometries for modification using computer aided design. The articulating surfaces were kept intact and internal geometries remained compatible with the required TKR cutting guides. The reverse engineered TKR components including the tibial baseplate, femoral

component and tibial insert were refabricated in a rigid polymer matrix material (Objet350, Statasys) for use in the experimental simulator (Figure 6.1) [22]. Permanent fiducial markers (aluminum ball bearings) were implanted onto the TKR components in order to establish local reference frames for motion analysis and for component visualization in radiography (Figure 6.1).

Design of Biomechanical Knee Rig

A mechanical rig was designed for the experimental simulation of intraoperative passive motions performed on an implanted cadaver knee. The knee rig design was constructed of a horizontal rail with mechanical linkages at the proximal femur bone representing the 'hip joint' and at the distal tibia bone representing the 'ankle joint' [20]. The mechanical hip joint exhibited one rotational degree of freedom (DOF) in flexion-extension rotation. The ankle joint exhibited three DOFs (internal-external rotation, anterior-posterior translation, and medial-lateral translation) when linked to the knee rig and easily disengaged from the knee rig in order to free float while handheld by the surgeon (Figure 6.2). This setup is similar to the clinical configuration by retaining all six DOFs of the knee joint, and allowing the femur to be held in place while manipulations occurred at the tibia. The quadriceps tendon was firmly secured to the knee rig via a custom-designed clamp and linear spring (stiffness of 1.2 N/mm) that acted parallel to the physiological line of action to mimic the passive resistance of the extensor mechanism and ensure the patella remains in contact with the femur during knee flexion [20].

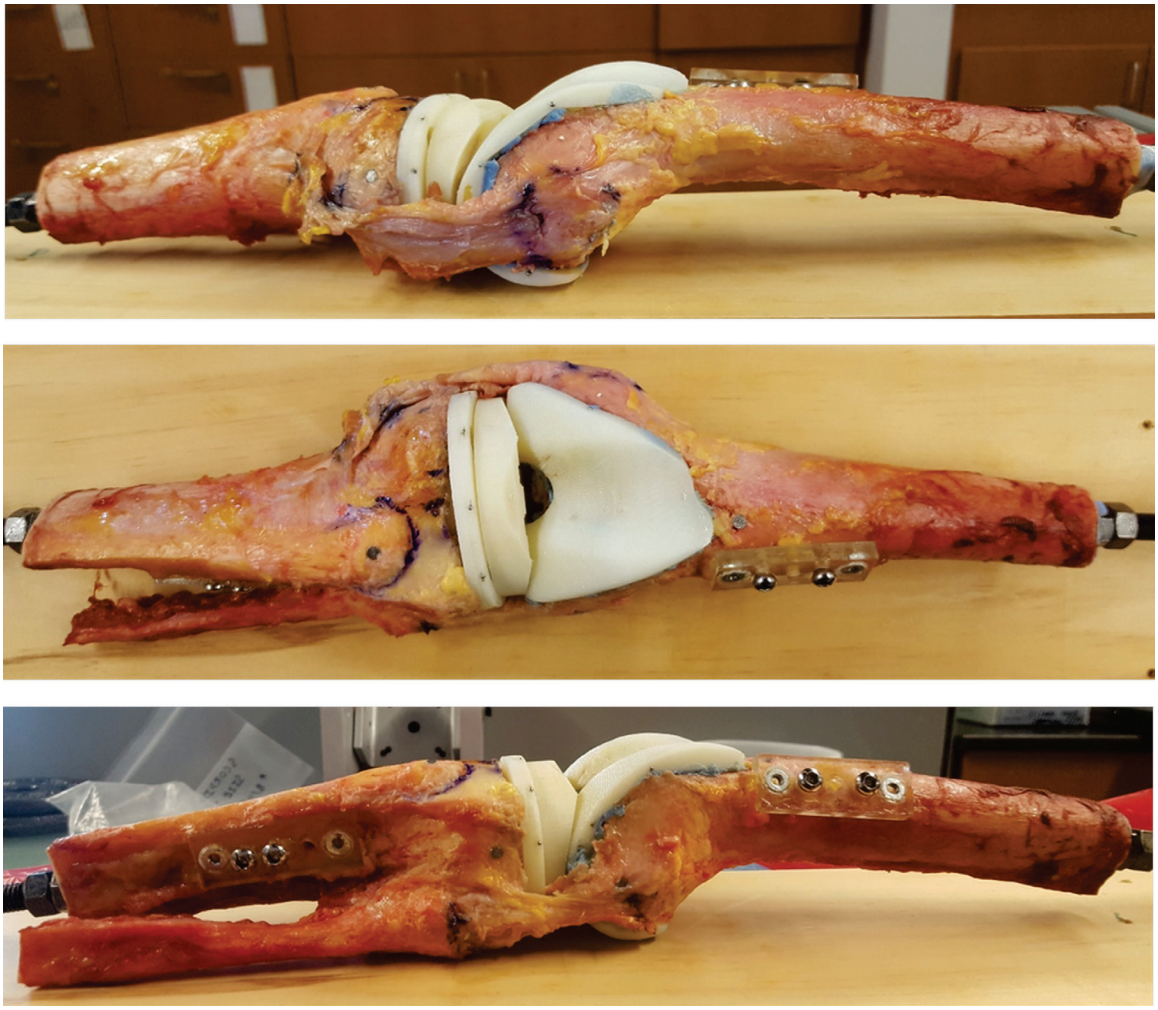

Figure 6.1. Implanted cadaver knee specimen dissected down to the MCL, LCL, and PCL. The specimen was implanted with custom 3D printed TKR components embedded with metallic fiducial markers.

Experimental Testing Sequence

Passive tests experimentally completed on the TKR knee specimen include passive laxity tests and passive ROM. Passive laxity tests were performed at 0°, 15°, 30°, 45°, and 60° by stabilizing the distal femur in one hand and manually applying forces at the instrumented ankle joint with the other hand to generate a 10 Nm varus-valgus (VV) torque or 3 Nm internal-external (IE) torque about the knee joint. Flexion angle was approximated

during testing using an external goniometer. The passive laxity tests were completed under the neutral alignment condition only.

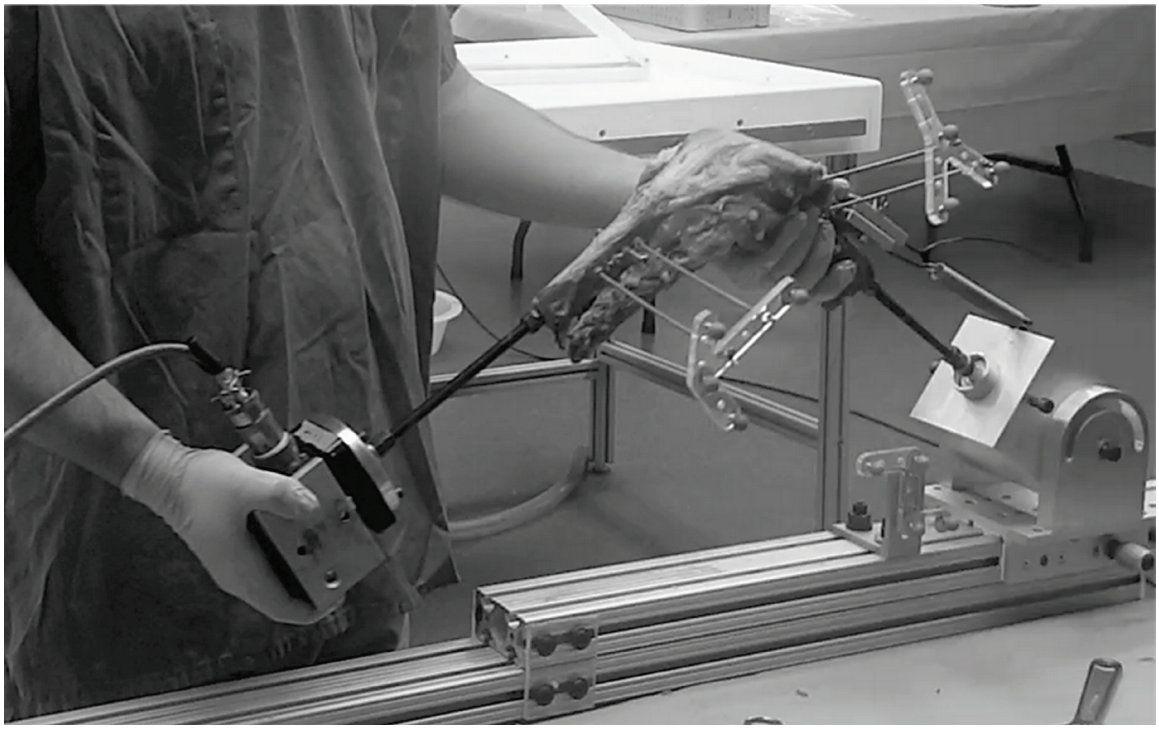

Figure 6.2. Biomechanical knee rig with cadaver knee assembled in the passive ROM test configuration. Joint motion was captured with passive marker arrays fixed to the femur and tibia bones and a 6 DOF load cell attached at the simulated ankle joint measured external loads.

The passive ROM test was performed by stabilizing the distal femur in one hand and manually applying forces at the instrumented ankle joint with the other hand to flex the knee from full extension to approximately 120^{o} flexion and then reverse direction back to full extension. A constant speed was maintained to complete a full cycle (0^{o}-120^{o}-0^{o}) in 5-10 seconds. The passive ROM test was repeated for each TKR alignment condition (neutral, external, and internal) for a total of three tests. Following experimental testing,

the knee specimen was dissected down to the posterior-cruciate ligament (PCL) and medial and lateral collateral ligaments. The attachment sites on the femur and tibia were then digitized using an optically tracked maker array fixed to a metallic probe for the PCL, superficial and deep medial collateral ligaments (MCL and DMCL) and the lateral collateral ligament (LCL).

Experimental Measurements

A series of passive tests were performed on the TKR cadaver knee when mounted in the biomechanical knee rig while measuring external loading and limb motions simultaneously. The ankle joint was instrumented with a 6 DOF load cell (MC3A 1000, AMTI) rigidly fixed to the distal tibia at the ankle joint in order to measure external loading applied during the passive tests [23]. The amplifier gain and excitation voltage were adjusted to optimize signal resolution under the anticipating loading conditions. The accuracy of the load cell was 8.8 N and 0.11 Nm in the axial direction (compressive load and IE torque) and 4.4 N and 0.22 Nm in the other DOFs. LabVIEW (National Instruments, Austin, TX) provided a visual display of the loads being applied in all 6 DOFs in real-time. The threaded rods and load cell axes were digitized in order to calculate the moments applied at the knee joint from the measured loads. For kinematic measurements, a two-camera optical tracking system (Polaris Vicra, NDI Medical) and two passive marker arrays rigidly fixed to the femur and tibia bones measured limb motions relative to an array defining a global coordinate system. The root-mean-square accuracy of the optical tracking system was 0.5 mm. The handheld digital probe registered the x,y,z coordinate locations of the fiducial markers on the implanted TKR components in order to define local

coordinate systems for the individual components within the global reference frame. A custom-written MATLAB (MathWorks, Natick, MA) script performed coordinate transformations on limb motions to calculate TKR kinematics based on the Grood Suntay coordinate system [24] from the digitized fiducial markers on the TKR components. Both the load cell and optical tracking system were operated at 20 Hz and synced using a manual trigger.

Development of Specimen-Specific Finite Element Model

A force-driven specimen-specific finite element (FE) model of the TKR cadaver knee was developed in ABAQUS/EXPLICIT (Simulia, Providence, RI) using the same modeling techniques used in Chapters 4 and 5. Bone geometries were reconstructed from segmented CT images using Mimics software (Materialise, Leuven, Belgium), and subsequently meshed using rigid triangular elements in Hypermesh software (Altair, Troy, MI). Specimen-specific 3D TKR geometry was virtually implanted onto the bones and also meshed using rigid triangular elements except for a deformable tibial insert meshed using eight-node hexahedral elements. As described previously in Chapter 4, eight tibiofemoral ligaments were represented by non-linear, tension-only springs. Ligament locations were defined using the digitized ligament attachment sites and anatomical descriptions. The patellar tendon and quadriceps tendon were also modeled as bundled springs, and tension was applied to the quadriceps tendon in order to allow the patella to track physiologically and mimic the mechanical spring used in the knee rig. The FE TKR model was positioned into the experimental space by matching up point clouds on the meshed geometries corresponding with the fiducial markers and the digitized spatial

locations of those fiducial markers recorded during the experiment. Kinematics were calculated using the Grood Suntay coordinate system modeled as a kinematic linkage between the coordinate systems of the femoral component and tibial baseplate. Boundary conditions were defined from the experimentally measured external loads including compressive force, varus-valgus moment, flexion-extension moment, and internal-external moment. For each simulation, the starting pose of the knee model was matched to that measured experimentally prior to applying the external loads.

Calibration of Soft Tissue Parameters in FE Model

The ligaments in the specimen-specific FE TKR model were calibrated using the load and kinematic data collected during the passive laxity test in order to better represent the cadaver soft tissue and further improve the validation process. Calibrated ligament parameters include linear ligament stiffness, reference strain, and attachment site for each ligament. In individual simulations, the external loading applied during each of the passive laxity tests performed experimentally (i.e. VV and IE torques) were replicated at each flexion increment tested from 0^{o}-60^{o}. The computational simulations were constrained to the kinematic DOF being ranged in order to isolate ligaments contributing to laxity in that specific DOF (e.g. only varus-valgus rotation unconstrained during applied varus-valgus torque).

The ligament parameters were calibrated using the Isight (Simulia, Providence, RI) optimization software. An adaptive simulated annealing optimization technique was applied to minimize the RMSE between model-predicted and experimentally-measured kinematics for each simulation simultaneously [9, 10]. The optimization process was

repeated for 500 iterations and the convergence criterion set at 0.01 degrees. During the calibration, ligament attachment locations were allowed to vary up to 3 mm except in directions that caused the location to move off or inside the bone surface. Ligament stiffness values were allowed to vary based off variability reported in the literature [10]. For reference strain, ligaments located based off of experimental digitization data (i.e. MCL, PCL, LCL) were only allowed to vary 10% whereas ligaments located based off anatomical descriptions (i.e. ALS, PFL, POL) were allowed to vary up to 25%.

Validation of Force-Driven Passive Knee Model

The force-driven specimen-specific FE model was validated by applying external loads measured experimentally during Passive ROM tests and calculating the RMSE between experimentally-measured and model-predicted knee kinematics. Specifically, tibiofemoral anterior-posterior (AP) and medial-lateral (ML) translations and flexion-extension (FE), internal-external (IE), and varus-valgus (VV) rotations were compared. Model validation was performed for each TKR alignment condition experimentally simulated. Additionally, model predicted ligament tensions output from the different TKR alignment conditions were compared. From calculated ligament tensions under TKR neutral alignment, the percent difference (increase or decrease) in tension was calculated for each ligament between 15^{o} changes in rotational alignment at discrete flexion angles from 0^{o} to 60^{o} flexion.

Results

Several abnormalities were noted in the knee specimen during TKR including severe osteoarthritis on the lateral compartment of the tibia and erosion of the postero-

lateral articular surface and bone of the tibia. The attending orthopaedic surgeons also noted medial laxity when assessing the ligaments of the knee specimen indicating a lack in tension in the medial soft tissues. The PCL was also noted to be lax in extension and early flexion.

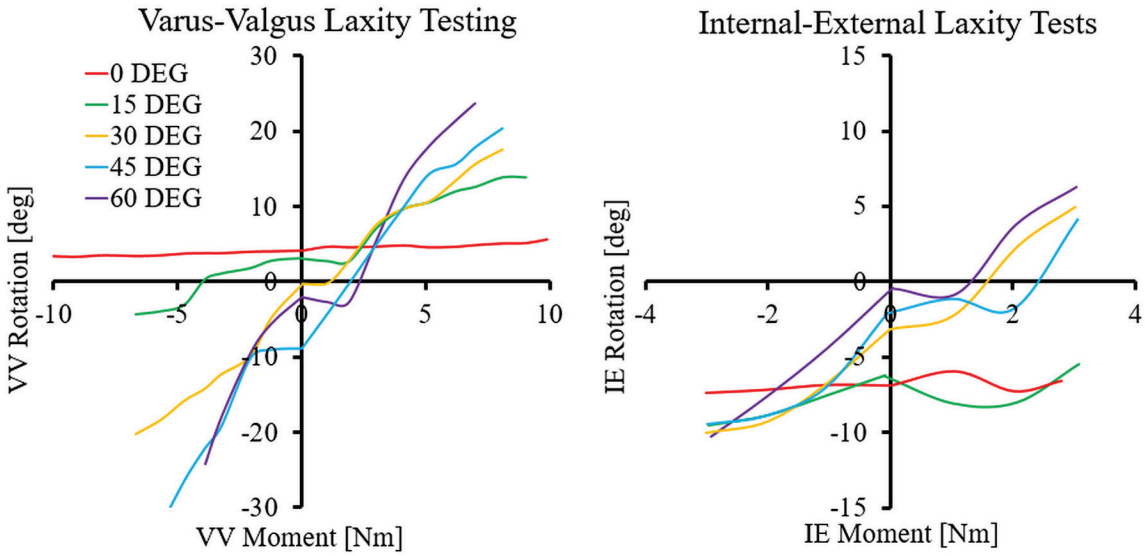

Figure 6.3. Experimental torque versus rotation curves measured during varus-valgus (VV) and internal-external (IE) passive laxity tests at flexion angles of 0°, 15°, 30°, 45°, and 60°.

During the experimental laxity tests, the full ±10 Nm VV torque and ±3 Nm IE torque could not be achieved at all flexion angles due to an increase in laxity at various flexion angles and to prevent any soft tissue damage that would compromise further testing. Both series of tests demonstrated increased ROM with increasing flexion angle. For the VV tests, the ROM increased from 2° at extension to 48° at 60° flexion (Figure 6.3). For the IE tests, the ROM increased from 1° at extension to 16° at 60° flexion (Figure 6.3). In

general, valgus torque generated greater rotation than varus torque, and similar rotation magnitudes were generated for internal or external torque.

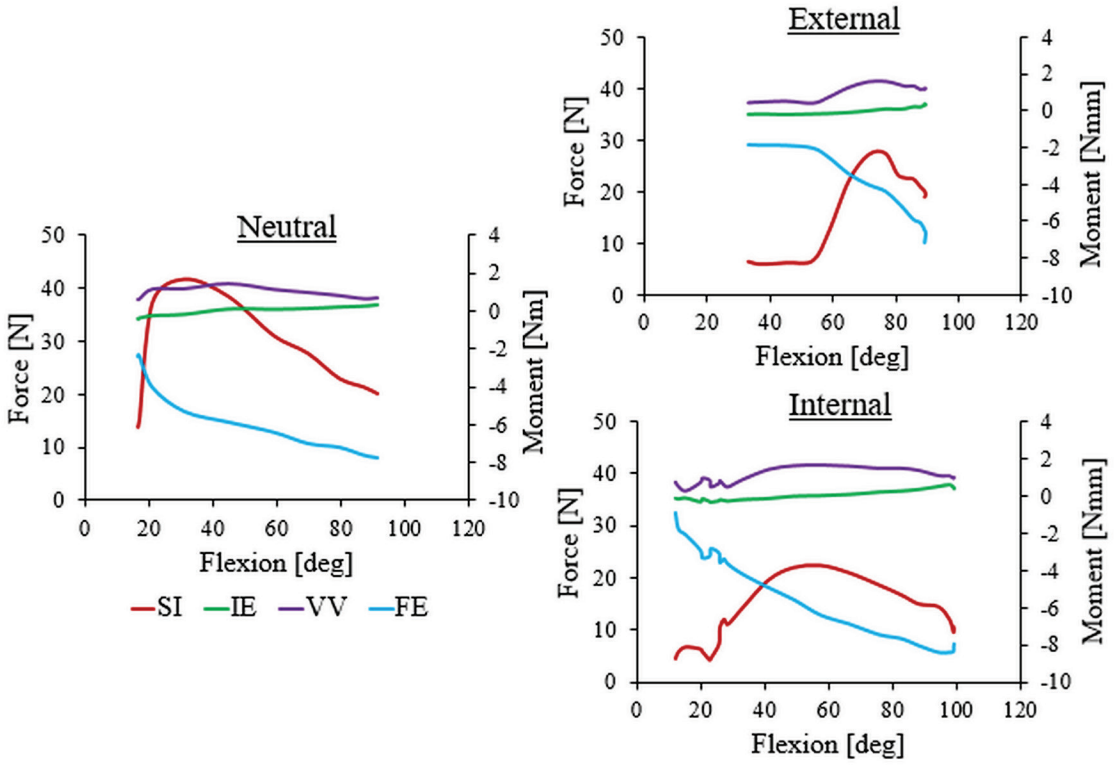

Figure 6.4. Applied loads measured during passive ROM for neutral, internal, and external TKR component alignments. Positive force and torque values represent compressive axial force in superior-inferior (SI) direction, internal torque, varus torque, and flexion torque.

The loads measured during passive ROM for each TKR alignment condition were similar in magnitudes and trends. Loading conditions of passive ROM were characterized by an internal torque, flexion torque, valgus torque and a compressive axial force (Figure 6.4). The most notable difference amongst the three alignment conditions was that the external tibial alignment required less flexion torque to passively flex the knee compared

to the neutral and internal alignment conditions. The greatest discrepancy in flexion-extension torque between external alignment compared to the other two conditions was approximately 4 Nm near 50° flexion (Figure 6.4). Variations in varus-valgus torque and internal-external torque were less than 1.2 Nm and 0.3 Nm, respectively (Figure 6.4). The compressive force recorded demonstrated increased variability amongst the three alignment conditions in the early- to mid-flexion range, but converged with continued knee flexion.

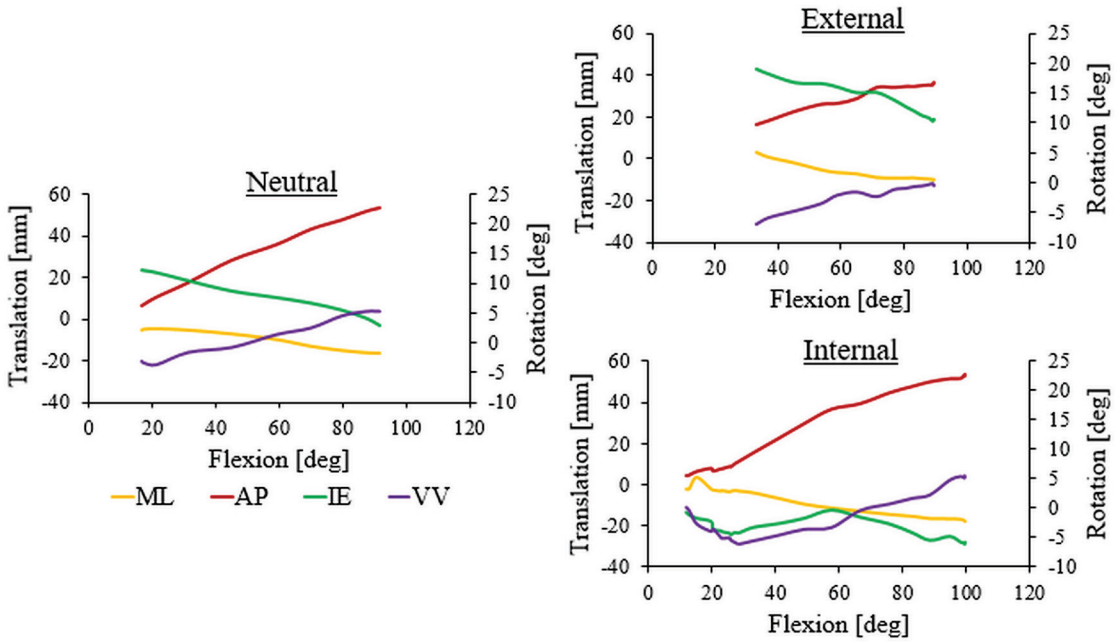

Figure 6.5. Knee kinematics measured during passive ROM for neutral, internal, and external TKR component alignment. Positive translation and rotation values represent lateral translation, anterior translation, external rotation, and valgus rotation of the tibial component relative to the femoral component.

Table 6.1. Final ligament parameters determined from calibration and used in the specimen-specific TKR knee model. Stiffness and reference strain bounds for each ligament are shown in brackets along with the reference length defined.

Ligament	Stiffness (N/mm)	Reference Strain	Reference Length (mm)
ALS	58 [15-135]	0.93 [0.75-1.25]	27.7
LCL	127 [60-200]	0.99 [0.85-1.15]	56.1
MCLa	121 [60-180]	0.92 [0.85-1.15]	79.9
MCLm	121 [60-180]	0.95 [0.85-1.15]	79.9
MCLp	121 [60-180]	0.96 [0.85-1.15]	79.9
DMCL	114 [50-180]	0.83 [0.85-1.15]	48.3
POL	63 [30-90]	0.88 [0.75-1.25]	32.3
PCAPl	100 [50-110]	1.09 [0.75-1.25]	48.8
PCAPm	52 [50-110]	1.05 [0.75-1.25]	45.7
PCLal	41 [30-100]	0.86 [0.85-1.15]	37.9
PCLpm	32 [30-100]	0.95 [0.85-1.15]	34.8
PFL	17 [10-90]	0.99 [0.75-1.25]	49.4

Kinematics measured during the experimental passive ROM under each of the TKR alignment conditions were characterized by valgus rotation, internal rotation, anterior translation, and medial translation of the tibia relative to the femur as the knee flexed (Figure 6.5). The only exception to these trends was external rotation exhibited by the internal alignment condition during mid-flexion. As expected, IE rotation demonstrated the greatest discrepancies with at least a 5° offset between neutral and internal or external alignment, and a maximum difference of 15° over the passive flexion range (Figure 6.5). For VV rotation, the internal and external alignment conditions presented a varus rotation offset compared to neutral, but variations in VV rotation did not exceed 5°. ML and AP translations followed very closely between neutral and internal alignments while external alignment had a lateral offset of at least 5 mm and AP translation diverged up to 19 mm posterior as the knee flexed (Figure 6.5).

The calibrated ligament parameters including reference strain and stiffness values are reported in Table 6.1. A total of 500 iterations were run during the calibration process in Isight. All ligaments exhibited reference strains below 1.0 with the exception of the posterior capsule, and the medial ligaments exhibited lower reference strains compared to the lateral ligaments.

RMSE between experimental and model kinematics for each of the three TKR alignment conditions during passive ROM are displayed in Table 6.2. For the neutral alignment condition, the average RMSE up to 60° flexion were less than 2.4° for flexion and VV rotations, 4.3° for IE rotations and 8 mm for AP and ML translations, and all translations and rotations matched trends of the experimental kinematics (Figure 6.6).

Model predicted kinematics under internal and external TKR alignment conditions also matched trends with experimental kinematics with the exception of IE rotation in the external alignment condition (Figure 6.7 & Figure 6.8). Overall, average RMSE for the internal and external TKR alignments were less than 7° for flexion and VV rotation, 16.3° for IE rotation, and 10 mm for AP and ML translations (Table 6.2).

Table 6.2. RMSE between experimental and model kinematics during passive ROM for neutral, internal, and external alignments. Flexion-extension (FE), internal-external (IE), and varus-valgus (VV) rotations and medial-lateral (ML) and anterior-posterior (AP) translations were compared.

	Kinematic DOF				
TKR Alignment Condition	FE (deg)	IE (deg)	VV (deg)	ML (mm)	AP (mm)
Internal	5.9	16.3	6.5	8.2	10.1
Neutral	2.4	4.3	2.1	7.9	6.5
External	6.5	9.3	6.1	3.5	11.3

Computational simulation of passive ROM only calculated ligament tensions in the lateral soft tissue structures for all three TKR alignments. In general, the ALS increased in tension, the LCL decreased in tension, and tension in the PFL remained relatively constant as the knee was flexed (Figure 6.9). External rotation of the tibial baseplate decreased tension in the ALS by approximately 80%, and decreased tension in the LCL and PFL by approximately 72% and 21%, respectively, before disengagement beyond 30° flexion (Figure 6.9). Internal rotational of the tibial baseplate decreased tension in the ALS by approximately 87% and delayed engagement until 50° flexion, increased tension in the

PFL by approximately 30%, and never engaged the LCL (Figure 6.9). The medial ligaments including the superficial MCL and DMCL did not generate any tension during the passive ROM except beyond 30° flexion for tibial internal alignment. The POL, posterior capsule and PCL did not engage during passive ROM.

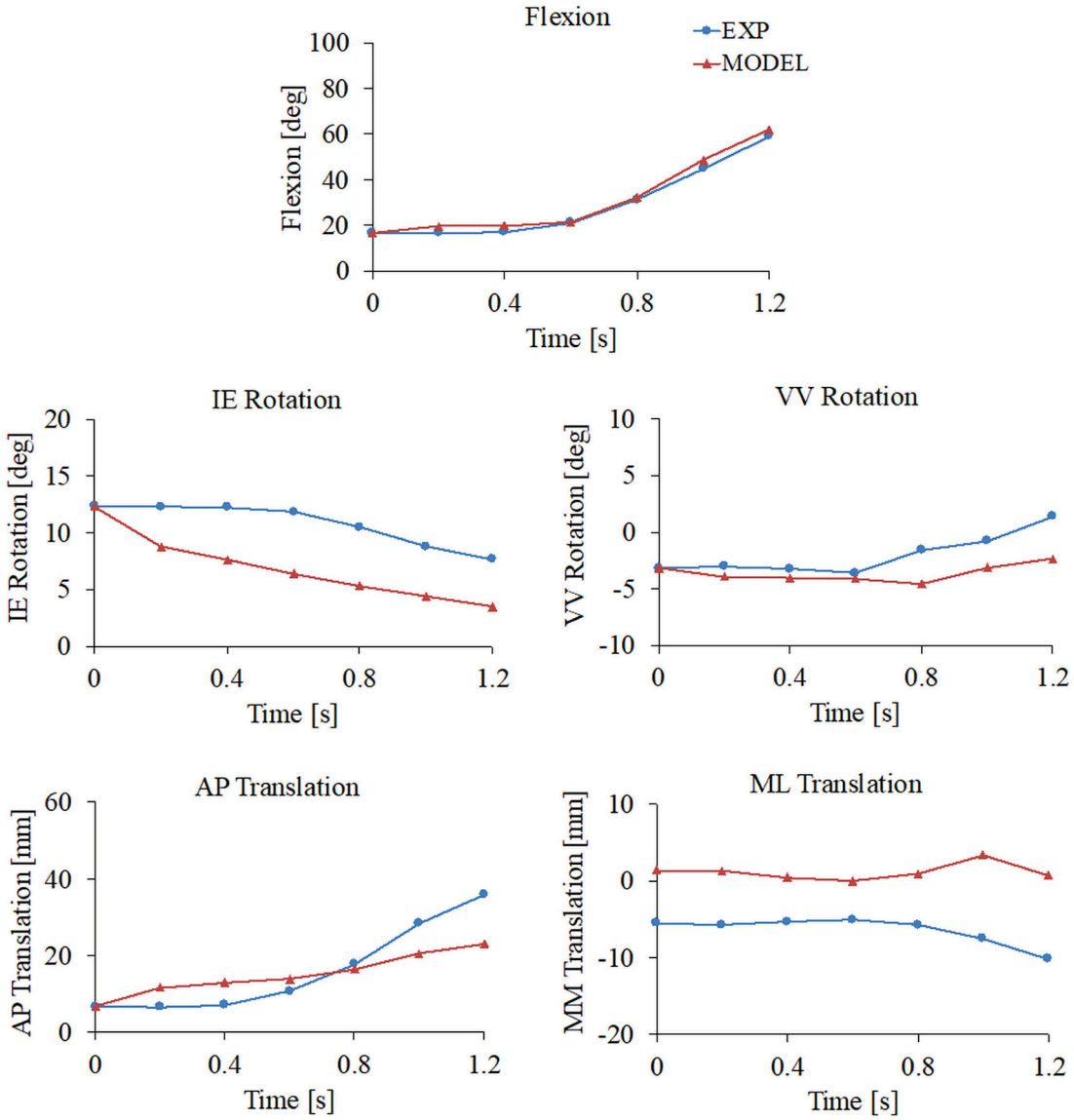

Figure 6.6. Comparison of experimental and model kinematics during simulated passive ROM under neutral alignment.

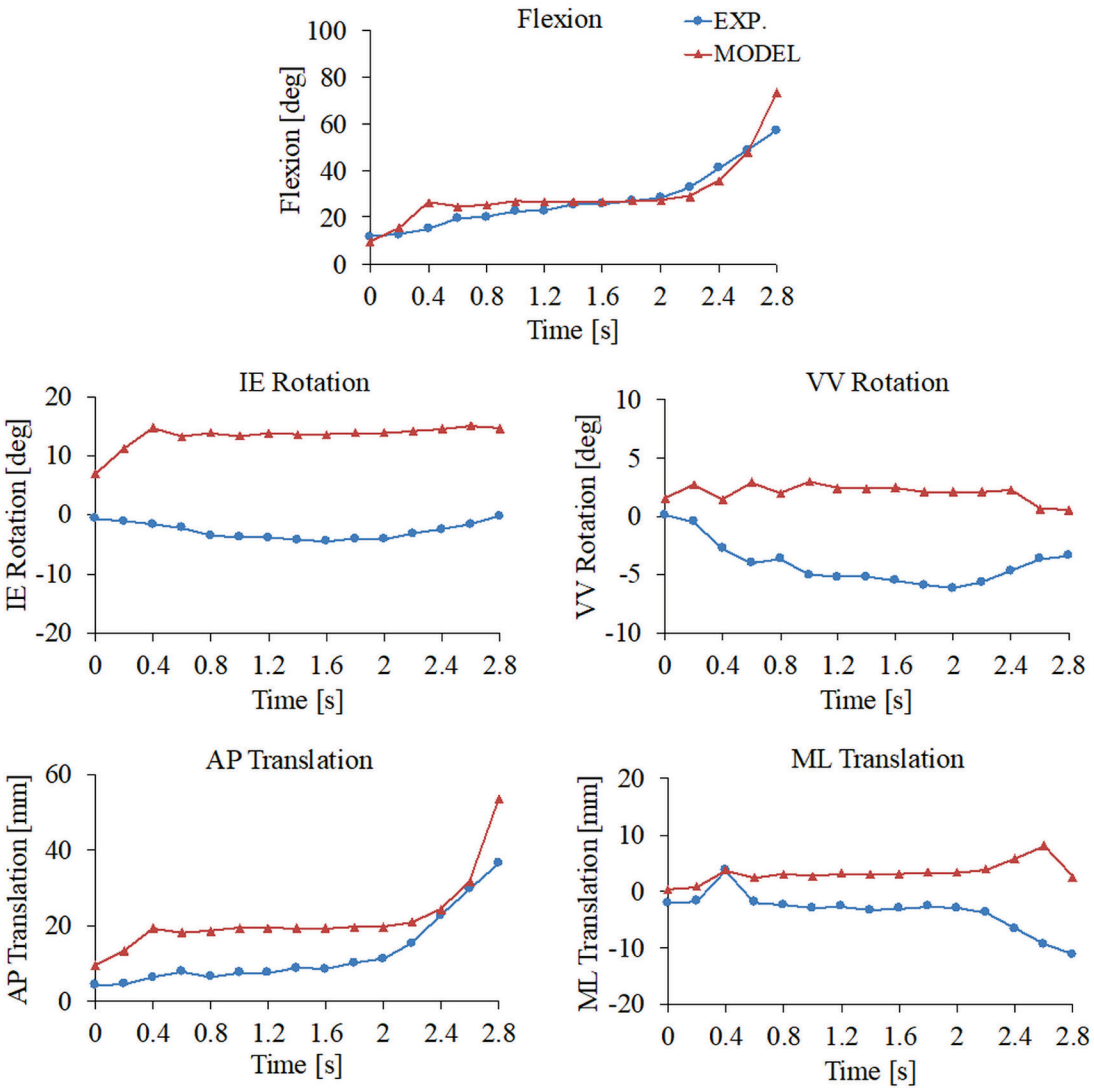

Figure 6.7. Comparison of experimental and model kinematics during simulated passive ROM under internal alignment.

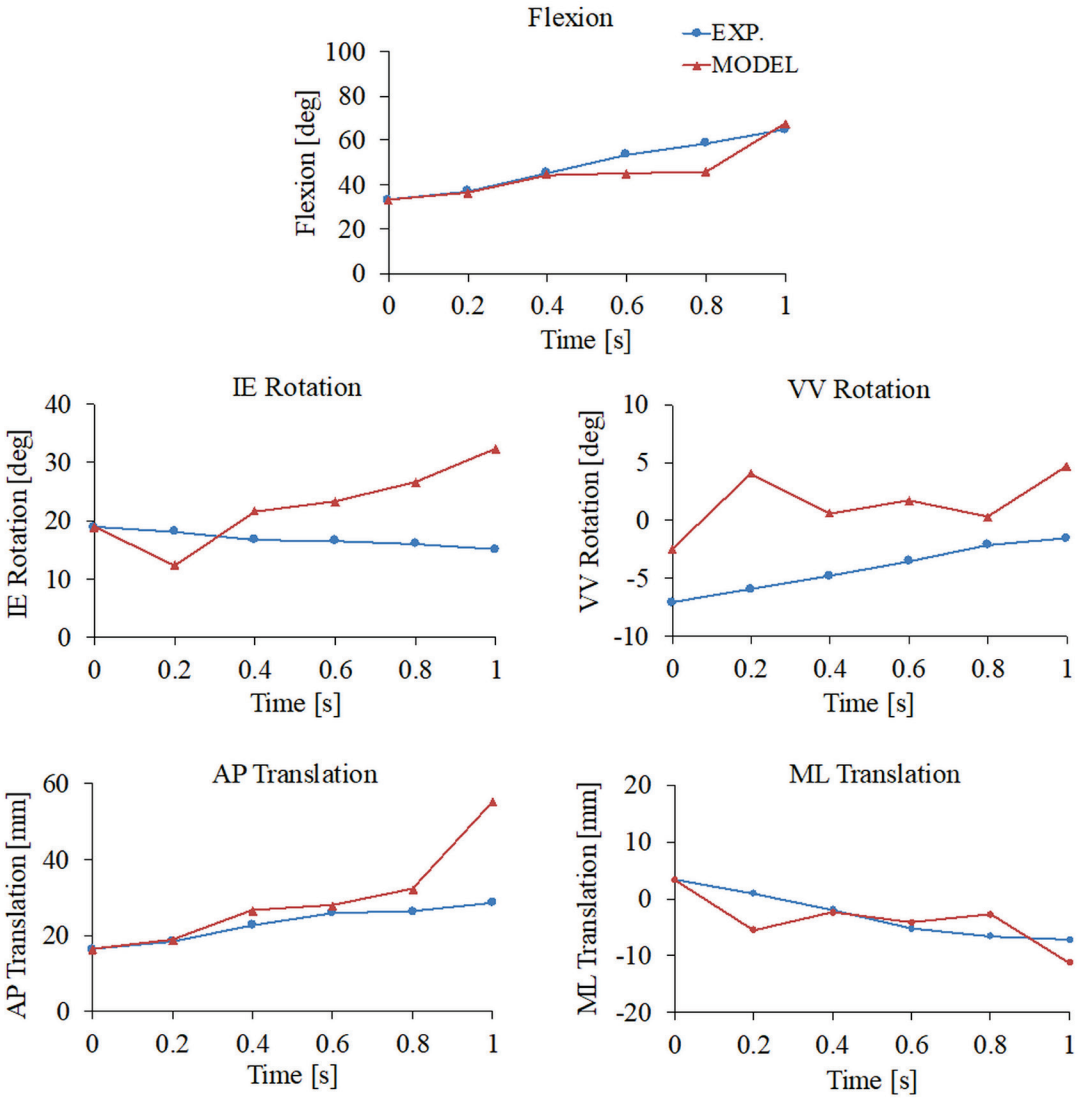

Figure 6.8. Comparison of experimental and model kinematics during simulated passive ROM under external alignment.

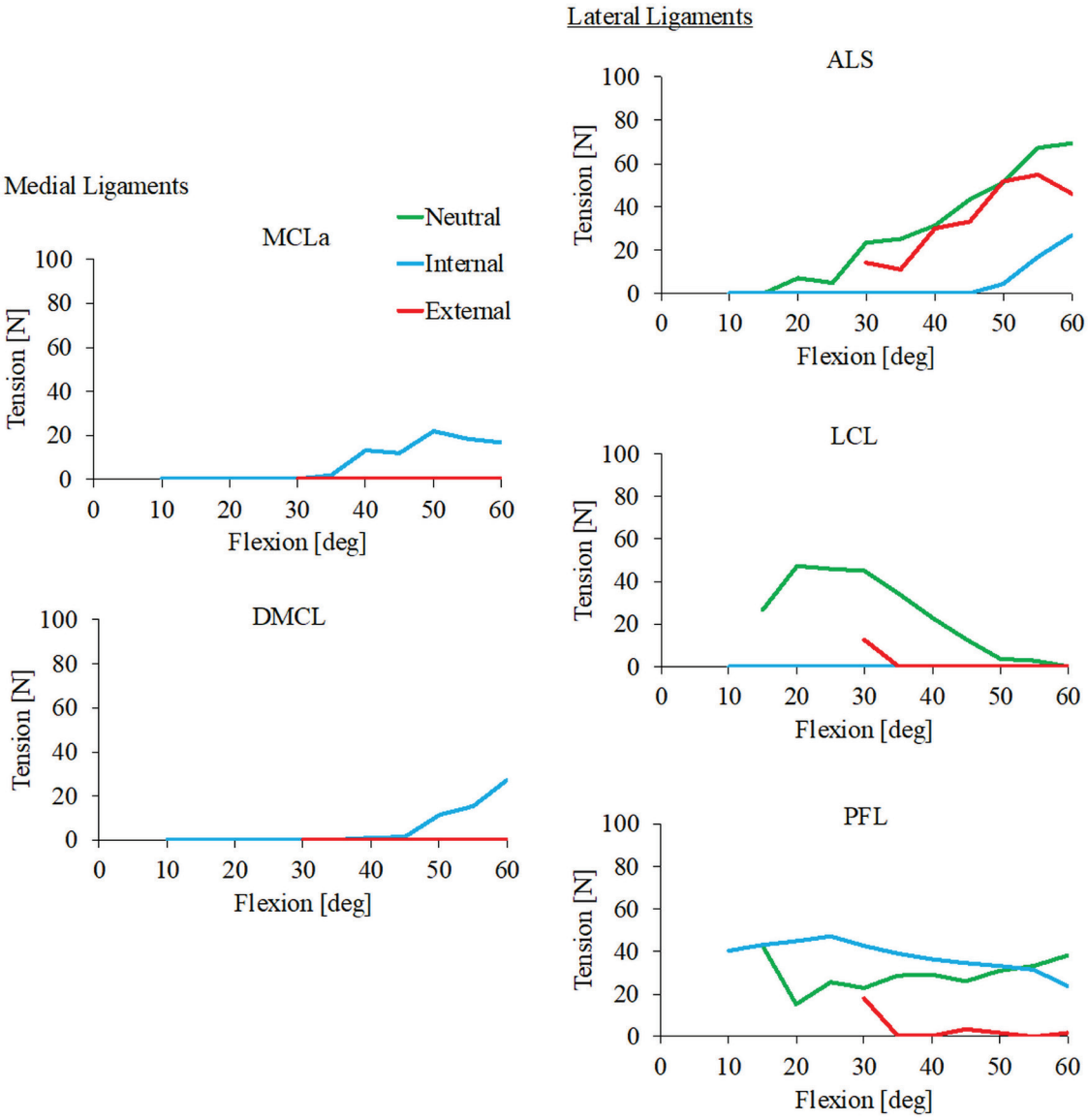

Figure 6.9. Model predicted ligament tension during passive ROM for neutral, internal, and external alignments. For the medial ligaments, only the superficial and deep medial collateral ligament (MCL and DMCL) calculated tension. For the lateral ligaments, the anterolateral structure (ALS), lateral collateral ligament (LCL) and popliteofibular ligament (PFL) calculated tension.

Discussion

In the current study, experimental simulation of passive ROM was completed on a TKR cadaver knee in order to quantify applied loads and kinematics and to validate a specimen-specific FE TKR model for computational simulation of passive ROM and calculation of ligament tensions. Experimental and computational simulations were completed for neutral component alignment and when the tibial baseplate was internally and externally rotated in order to compare loading conditions, kinematics, and ligament tensions under intraoperative conditions. Loading conditions for all alignment conditions were characterized by an internal torque, flexion torque, valgus torque and a compressive axial force, and exhibited similar magnitudes with the exception of flexion torque for external alignment. Besides the external rotation produced by internal component alignment, kinematic profiles either matched closely or exhibited a consistent offset. Model validation for neutral alignment resulted in the best match between experimental and model kinematics, but general trends in experimental kinematics were predicted for all three models especially for flexion angle, the dominant kinematic DOF during passive ROM. In comparison to neutral alignment, internal alignment decreased tension in lateral ligaments and increased tension in the medial ligaments whereas external alignment decreased tension in all ligaments.

Applied load profiles measured during experimental passive ROM were relatively low in magnitudes and did not vary considerably for the different alignment conditions tested. Compressive forces recorded were orders of magnitude less than reported during weight-bearing activity [25, 26] and in agreement with intraoperative forces quantified

during TKR surgeries using load-sensing technology [27-29]. The reported flexion moment during passive ROM in the current study was also appreciably less than the previously reported 30-50 Nm moments generated by muscles acting about the knee joint during gait [30,31]. These lower load magnitudes could contribute to the lack in unique load profiles among the different alignment conditions, and highlight the difficulty in distinguishing distinct differences in component alignments during intraoperative passive ROM based off the "feel" of the surgeon alone [1].

Although experimental kinematics were also similar between the different TKR alignment conditions, differences in IE rotation were consistent with clinical observations. A previous study reported tibial external rotation during passive ROM in patients implanted with the same mobile-bearing TKR design as the current study when tibial component rotational alignments were greater than 10^{o}, and was indicative of poor TKR functional outcomes when rotational mismatch also exceeded 10^{o} [32]. Given neutral alignment measured a 2.3^{o} rotational mismatch and tibial component rotational alignment was perturbed ±15^{o}, these findings agree with the external rotation displayed by the internal alignment condition during mid-flexion. In contrast, neutral and external alignments generated tibial internal rotation during passive ROM despite external alignment also featuring rotational mismatch greater than 10^{o}.

Validation of the FE TKR model revealed better agreement for neutral alignment compared to internal and external alignments. RMSEs calculated during validation of the neutral alignment FE TKR model were similar to those reported for other knee models validated against coupled motion of the knee during flexion [9, 10]. Although the internal

and external alignment FE TKR models matched magnitudes for the dominant kinematic DOF, flexion, they had increased errors in IE and VV rotations. There are several possible explanations for these inconsistencies. From an experimental perspective, the testing sequence completed passive ROM under neutral alignment immediately following passive laxity testing used for ligament calibration, and then performed passive ROM for internal and external alignments subsequently thereafter. Hence, the latter two alignment conditions tested were more at risk to changes in soft-tissue properties. Another possible explanation is that modeled internal and external alignment conditions were more susceptible to measurement error since only the neutrally aligned components were mapped into the model and not recreated by virtual adjustment in the model. Also, given the known associated instability with the internal and external alignment conditions tested combined with the medial laxity already being accounting for in the model ligament properties, the FE model may not of been able to adequately constrain the knee. Nonetheless, all models matched trends of the experimental kinematics, matched magnitudes of the dominant kinematic DOF, and provide confidence that the model can be executed under different TKR alignment conditions.

Comparison of ligament tension for the different tibial component rotational alignments revealed mixed agreement with literature findings. Although there is a general consensus that femoral component internal and external rotation increases tension in the MCL and LCL, respectively, the effects of tibial component axial rotation on soft-tissue tension is not well defined [5,8]. Thompson, et al. concluded that only femoral component axial rotation affected ligament tension and reported zero tension in the MCL and LCL

during simulated squat for ±15° malrotation of the tibial component [5]. However, Kuriyama, et al. reported increased LCL tension when the tibial component was 15° externally rotated, and increases in both the MCL and LCL when the tibial component was 15° internally rotated [33]. In the current study, internal alignment predicted higher tension in medial ligaments, but only higher tension in the PFL on the lateral side during simulated passive ROM. In essence, the inconclusive trends between ligament tension and tibial component rotational alignment in the literature were also evident in this study.

The ligament calibration process and absence of medial ligament engagement in the model confirmed the medial laxity noted in the knee specimen during TKR. Compared to *in vivo* studies of cruciate retaining TKR, the TKR knee specimen in the current study exemplified abnormal medial laxity with excessive VV ROM and greater valgus laxity compared to varus [34, 35]. This medial laxity translated over to the calibrated ligament parameters as evidence by lower reference strains in the medial ligament compared to the lateral ligaments and lower stiffness in the medial posterior capsule compared to the lateral side. Although the post-operative medial laxity limited the range of flexion that could be simulated, the ability to model the behavior of a diseased knee was encouraging, and has not been done previously [36].

The computational simulation of passive ROM was actuated by recreating the experimentally measured loads at the knee joint. However, the simulation also required a force applied to the extensor mechanism via the quadriceps tendon in order to counter the applied flexion moment and accurately predict the flexion profile. In the experimental setup, a linear spring was used to mimic the passive restraint of the extensor mechanism,

but the force generated during passive ROM was not quantified. As a result, the tension applied to the quadriceps tendon in the FE simulation was manually adjusted in order to match the flexion profile. The tension was adjusted within 10-90 N as recorded during passive flexion in a similar *in vitro* test that also used a spring of nearly identical stiffness [20]. Similar approaches of adjusting quadriceps load to match kinematic profiles during experimental [37, 38] and computational [9, 16] simulations have been applied previously.

This study included several notable limitations experimentally and computationally. Experimentally, loading conditions were quantified during passive ROM performed by a single subject. Although variability in applied loads during passive ROM has not been quantified, substantial variability has been noted during other clinical assessments of the passive knee [23, 39]. Thus, including additional subjects would help further define these loading conditions. Additionally, the current study chose to only perturb axial rotational alignment of the tibial baseplate because it exhibits the greatest variability out of all alignment DOFs with no gold standard [40] and has been indicative of functional outcome [32].

From a computational perspective, the unique loading conditions applied to the FE simulation of each TKR alignment may have contributed to the difficulty in quantifying relationships between TKR component alignment and ligament tension in this study. *In vitro* knee rigs and computational models are typically used to analyze such relationships between surgical factors and knee mechanics due to repeatability of loading and boundary conditions [6, 20]. Perturbing component alignment under identical loading conditions may provide a more effective parametric approach. Also, ligament calibration and model

validation was only performed up to 60º flexion. This was due to the poor function of the TKR knee specimen beyond 60º flexion during experimental testing as described earlier. Despite this limitation, the model is still clinically relevant since it is valid during the mid-flexion range where passive kinematics during intraoperative assessments have been indicative of functional outcome [32].

Conclusion

In summary, a force-driven FE TKR model was validated for simulation of passive ROM performed during surgery. Model development was preceded by experimental simulation of passive ROM performed on a TKR cadaver knee to measure applied loads and knee kinematics. Although the cadaver knee specimen was characteristic of a diseased-state, validation of a diseased TKR model has not been previously accomplished and provides a more clinically accurate representation. Definitive trends between tibial component rotation alignment and ligament tension were not discerned despite overall agreement in model and experimental kinematics for neutral, internal, and external tibial component alignments. Future cadaver work is on-going and will help add clarity to these reported findings. Nonetheless, the force-driven knee model provides a foundation to quantify the relationship between TKR component alignment and ligament tension during intraoperative passive ROM.

References

[1] Schroer WC, Berend KR, Lombardi AV, Barnes CL, Bolognesi MP, Berend ME, Ritter MA, Nunley RM. Why are total knees failing today? Etiology of total knee revision in 2010 and 2011. Journal of Arthroplasty. 2013, 28(8 Suppl):116-119.

[2] Fehring TK, Odum S, Griffin WL, Mason JB, Nadaud M. Early failures in total knee arthroplasty. Clinical Orthopaedics and Related Research. 2001, 392:315-18.

[3] Thompson JA, Hast MW, Granger JF, Piazza SJ, Siston RA. Biomechanical effects of total knee arthroplasty component malrotation: a computational simulation. Journal of Orthopaedic Research. 2011, 29:969-975.

[4] Babazadeh S, Stoney JD, Lim K, Choong FM. The relevance of ligament balancing in total knee arthroplasty: how important is it? A systematic review of the literature. Orthopedic Reviews. 2009, 1:e26.

[5] Dalury DF, Pomeroy DL, Gorab RS, Adams MJ. Why are total knee arthroplasties being revised? Journal of Arthroplasty. 2013, 28(1 Suppl):120-121.

[6] Fitzpatrick CK, Clary CW, Rullkoetter PJ. The role of patient, surgical, and implant design variation in total knee performance. J Biomech. 2012a, 45:2092-2102.

[7] Kuriyama S, Ishikawa M, Nakamura S, Furu N, Ito H, Matsuda S. Posterior tibial slope and femoral sizing affect posterior cruciate ligament tension in posterior cruciate-retaining total knee arthroplasty. Clinical Biomechanics. 2015, 30:676-681.

[8] Kang KT, Koh YG, Son J, Kwon OR, Baek C, Jung SH, Park KK. Measuring the effect of femoral malrotation on knee joint biomechanics for total knee arthroplasty using computational simulation. Bone & Joint Research. 2016, 5:552-559.

[9] Baldwin MA, Clary C, Fitzpatrick CK, Deacy JS, Maletsky LP, Rullkoetter PJ. Dynamic finite element knee simulation for evaluation of knee replacement mechanics. Journal of Biomechanics. 2012, 45:474-483.

[10] Harris MD, Cyr AJ, Ali AA, Fitzpatrick CK, Rullkoetter PJ, Malestky LP, Shelburne KB. A combined experimental and computational approach to subject-specific analysis of knee joint laxity. Journal of Biomechanical Engineering. 2016, 138:081004-1.

[11] Anglin C, Brimacombe JM, Wilson DR, Masri BA, Greidanus NV, Tonetti J, Hodgson AJ. Biomechanical consequences of patellar component medialization in total knee arthroplasty. Journal of Arthroplasty. 2010, 25(5):793-802.

[12] Harman MK, Banks SA, Hodge WA. Polyethylene damage and knee kinematics after total knee arthroplasty. Clinical Orthopaedics and Related Research. 2001, 392:383-93.

[13] Halloran JP, Clary CW, Maletsky LP, Taylor M, Petrella AJ, Rullkoetter PJ. Verification of predicted knee replacement kinematics during simulated gait in Kansas knee simulator. Journal of Biomechanical Engineering. 2010, 132(8): 1-6.

[14] Fitzpatrick CK, Komistek RD, Rullkoetter PJ. Developing simulations to reproduce *in vivo* fluoroscopy kinematics in total knee replacement patients. Journal of Biomechanics. 2014 47:2398-2405.

[15] Ali AA, Shalhoub SS, Cyr AJ, Fitzpatrick CK, Malestky LP, Rullkoetter PJ, Shelburne KB. Validation of predicted patellofemoral mechanics in a finite element model of the healthy and cruciate-deficient knee. Journal of Biomechanics. 2016, 49(2):302-309.

[16] Fitzpatrick CK, Baldwin MA, Clary C, Maletsky LP, Rullkoetter P. Evaluating knee replacement mechanics during ADL with PID-controlled dynamic finite element

analysis. Computer Methods in Biomechanics and Biomedical Engineering. 2014c, 17(4):360-369.

[17] Cyr AJ, Shalhoub SS, Fitzwater FG, Ferris LA, Maletsky LP. Mapping of contributions from collateral ligaments to overall knee joint constraint: an experimental cadaveric study. Journal of Biomechanical Engineering. 2015, 137:061006.

[18] Ewing JA, Kaufman MK, Hutter EE, Granger JF, Beal MD, Piazza SJ, Siston RA. Estimating patient-specific soft tissue properties in a TKA knee. Journal of Orthopaedic Research. 2015 (in press). doi:10.1002/jor.23032.

[19] Hunt NC, Ghosh KM, Blain AP, Rushton SP, Longstaff LM, Deehan DJ. No statistically significant kinematic difference found between a cruciate-retaining and posterior-stabilised Triathlon knee arthroplasty. Journal of Bone & Joint Surgery. 2015, 97-B:642-648.

[20] Anglin C, Brimacombe JM, Wilson DR, Masri BA, Greidanus NV, Tonetti J, Hodgson AJ. Intraoperative vs. weightbearing patellar kinematics in total knee arthroplasty: A cadaveric study. Clinical Biomechanics. 2008, 23:60-70.

[21] Harman MK, Banks SA, Kirschner S, Lützner J: Prosthesis alignment affects axial rotation motion after total knee replacement: A prospective *in vivo* study combining computed tomography and fluoroscopic evaluations. BMC Musculoskeletal Disorders. 2012, 13(1):206-216.

[22] Schroder C, Steinbruck A, Muller T, Woiczinski M, Chevalier Y, Weber P, Muller PE, Jansson V. Rapid prototyping for *in vitro* knee rig investigations of prosthetized

knee biomechanics: comparison with cobalt-chromium alloy implant material. BioMed Research International. 2015, 185142.

[23] Clarke JV, Wilson WT, Wearing SC, Picard F, Riches PE, Deakin AH. Standardising the clinical assessment of coronal knee laxity. Journal of Engineering in Medicine. 2012, 226(9):699-708.

[24] Grood ES, Suntay WJ. A joint coordinate system for the clinical description of three-dimensional motions: application of the knee. ASME. 1983, 105:136-144.

[25] Kutzner I, Heinlein B, Graichen F, Bender A, Rohlmann A, Halder A, Beier A, Bergmann G. Loading of the knee joint during activities of daily living measured *in vivo* in five subjects. Journal of Biomechanics. 2010, 43: 2164-2173.

[26] Mundermann A, Dyrby CO, D'Lima DD, Colwell CW, Andriacchi TP. *In vivo* loading characteristics during activities of daily living as measured by an instrumented total knee replacement. Journal of Orthopaedic Research. 2008, 26: 1167-1172.

[27] Nodzo SR, Franceschini V, Della Valle AG. Intraoperative load-sensing variability during cemented, posterior-stabilized total knee arthroplasty. Journal of Arthroplasty. 2017, 32:66-70.

[28] Crottet D, Kowal J, Sarfert SA, Maeder T, Bleuler H, Nolte LP, Durselen L. Ligament balancing in TKA: evaluation of a force-sensing device and the influence of patellar eversion and ligament release. Journal of Biomechanics. 2007, 40: 1709-1715.

[29] Anastasiadis A, Megnissalis E, Tsakonas A. A novel intraoperative sensor for soft tissue balancing in total knee arthroplasty. Journal of Medical Engineering & Technology. 2010, 34(7-8): 448-454.

[30] Lundberg HJ, Rojas IL, Foucher KC, Wimmer MA. Comparison of antagonist muscle acitivity during walking between total knee replacement and control subjects using unnormalized electromyography. Journal Arthroplasty. 2016, 31: 1331-1339.

[31] Fantozzi S, Benedetti MG, Leardini A, Banks SA, Cappello A, Assirelli D, Catani F. Fluoroscopic and gait analysis of the functional performance in stair ascent of two total knee replacement designs. Gait and Posture. 2003, 17:225-234.

[32] Lutzner J, Krischner S, Gunther KP, Harman MK. Patients with no functional improvement after total knee arthroplasty show different kinematics. Int Orthop. 2012, 36:1841-1847.

[33] Kuriyama S, Ishikawa M, Furu M, Ito H, Matsuda S. Malrotated tibial component increases medial collateral ligament tension in total knee arthroplasty. Journal of Orthopaedic Research. 2014, 32: 1658-1666.

[34] Heesterbeek PJC, Keijsers NLW, Wymenga AB. Ligament releases do not lead to increased postoperative varus-valgus laxity in flexion and extension: a prospective clinical study in 49 TKR patients. Knee Surgery, Sports Traumatology, Arthroscopy. 2010, 18: 187-193.

[35] Takeda M, Ishii Y, Hoguchi H, Matsuda Y, Sato J. Changes in varus-valgus laxity after total knee arthroplasty over time. Knee Surgery, Sports Traumatology, Arthroscopy. 2012, 20:1988-1993.

[36] Rossi R, Rosso F, Cottino U, Dettoni F, Bonasia E, Bruzzone M. Total knee arthroplasty in the valgus knee. International Orthopaedics. 2014, 38: 273-283.

[37] Most E, Li G, Sultan PG, Park SE, Rubash HE. Kinematic analysis of conventional and high-flexion cruciate-retaining total knee arthroplasties. Journal of Arthroplasty. 2005, 20(4):529-535.

[38] Li G, Zayontz S, Most E, Otterberg E, Sabbag K, Rubash HE. Cruciate-retaining and cruciate-substituting total knee arthroplasty: an *in vitro* comparison of the kinematics under muscle loads. Journal of Arthroplasty. 2001, 16(8 Suppl 1): 150-156.

[39] Cushnaghan J, Cooper C, Dieppe P, Kirwan J, McAlindon T, McCrae F. Clinical assessment of osteoarthritis of the knee. Annals of the Rheumatic Diseases. 1990, 49: 768-770.

[40] Gromov K, Korchi M, Thomsen MG, Husted H, Troelsen A. What is the optimal alignment of the tibial and femoral components in knee arthroplasty? Acta Orthopaedica. 2014, 85(5): 480-487.

CHAPTER SEVEN

ENGINEERING SIGNIFICANCE, CONTRIBUTIONS AND CONCLUSIONS

The objective of this dissertation was to accurately represent material nonlinearity for computational analysis of the implanted knee joint by focusing on different aspects of TKR where material nonlinearity plays a major role in the biomechanics of the system under investigation. This objective was addressed through completion of three aims exemplifying a combined experimental and computational approach to analyze modes of failure in TKR that involve nonlinear material behavior including stresses in modular taper junctions (Aim 1) and ligament tensions during passive knee motions (Aims 2 and 3). Chapters 1 and 2 addressed Aim 1, Chapters 3 and 4 addressed Aim 2, and Chapter 5 addressed Aim 3 (Figure P.1).

Aim 1: Determine the stresses within modular taper junctions using FE analysis and their sensitivity to material model selection and geometry.

Aim 1 was accomplished by developing and validating multiple FE models of modular TKR taper junctions with varying taper geometries and material representations (i.e. linear elastic and elastoplastic) in order to analyze the impact of taper fit (i.e. angular mismatch) and material behavior on model-predicted stresses. Chapter 2 detailed the development of the taper junction FE model from retrieved prostheses and the development of material models from experimental datasets in order to compare stress analyses implementing linear elastic and elastoplastic material representations. Chapter 3 applied the developed elastoplastic taper junction FE model to perform a parametric analysis between taper geometry and contact mechanics.

Taper surfaces of explanted modular components reveal evidence of mechanically-assisted corrosion mechanisms, which suggests the taper junctions can experience elevated stresses in concentrated regions and cyclic micromotion [1-5]. Global deformations of modular implants analyzed experimentally [3, 6-9] and local deformations at the bore-cone taper interface analyzed computationally [10-13] treat the deformations as an elastic behavior despite evidence of plastic material deformation in explanted modular components [1,2,14] and reported post-yield stresses in macroscale FE taper junction models [10, 11]. Results from Chapter 2 established that linear elastic FE models of modular TKR taper junctions overestimate and even calculate unrealistic stresses for some taper geometries under *in vivo* loading conditions due to post-yield material behavior. Specifically, plastic deformation was evident at the leading edge of the cone taper when the bore taper angle exceeded the cone taper angle, and required an elastoplastic model to accurately capture the full stress environment (Chapter 2). These findings are consistent with reported permanent deformations of surface topography [2,15] and micron-scale FE submodeling of machining marks that suggests localized plastic deformations play a crucial role in the performance of bore-cone taper junctions [16,17]. Chapter 2 concluded that linear elastic models should be interpreted with caution, and that an elastoplastic material model provides a more robust modeling approach for FE analysis of modular taper junctions.

From a mechanical design perspective, the mating bore and cone components are uniformly tapered and when assembled, an interference fit is achieved through localized material deformation and subsequent residual stresses where the cone compresses against

the bore walls at a location along the taper interface [16, 18]. The desired interference fit is dependent on the geometric design of the taper junction, and specifically the angular mismatch between the bore and cone taper angles. In Chapter 3, it was found that variation in angular mismatch on the order of magnitude consistent with manufacturing tolerances influences the mechanical environment within the taper junction under *in vivo* loading conditions. Previously, ASTM Standard F-1636 specified manufacturing tolerances of modular taper junctions in orthopaedics providing guidance to design engineers; however, it was discontinued without replacement [19]. Angular mismatch within $\pm 10^{o}$ was found to exhibit the lowest stress magnitudes and the weakest correlation with micromotion suggesting the manufacturing tolerances specified in ASTM F-1636 should still be followed (Chapter 3).

The findings in Aim 1 provide insight to engineers into taper junction design and the use of FE analysis in the design process. Strong correlations between manufacturing tolerance and stress combined with the agreement between calculated stress distributions and *in vivo* and *in vitro* corrosion behavior confirms the importance of manufacturing tolerance to taper junction design. However, there is still a lack in quantitative relationships between the mechanics of modular taper junctions and corrosion in order to fully translate model predictions. A deeper understanding of the interplay between such mechanical parameters and corrosion to complement FE analysis would help inform industry on robust target manufacturing ranges.

Aim 2: Determine ligament tension patterns using a kinematically-driven FE knee model simulating patient-specific passive kinematics that discriminate *in vivo* clinical TKR outcomes.

Aim 2 was accomplished by adapting a validated open source FE natural knee model to a FE TKR model that input patient-specific data in order to simulate passive ROM of TKR patients with good and poor functional outcomes and compare calculated ligament tension patterns. Chapter 4 described the development of the passive TKR model from an open source dataset and assessed the ability of the model to input *in vivo* kinematics and discriminate functional outcomes based on calculated ligament tensions. Chapter 5 then applied the FE TKR model to simulate patient-specific passive ROM and elucidate ligament tension patterns characteristic of poor function.

During TKR procedures, intraoperative assessments of passive (non-weight bearing) range of motion (ROM) are routinely performed by the surgeon to assess knee stability and more specifically determine if proper TKR component alignment and ligament tensions have been achieved [20, 21]. Knee kinematic constraint during passive intraoperative assessments is provided by soft tissue tensions and conformity of articulating TKR surfaces due to the absence of muscle forces. Differences in TKR alignment and kinematics are difficult for surgeons to detect intraoperatively due to a lack of quantitative measurements of soft tissue tensions. Computational TKR models have proved to be an effective tool for analyzing knee mechanics, but have focused on simulating weight-bearing activities that are drastically different than the passive conditions in question [22-

25]. The passive FE TKR model produced in Chapter 4 provides a novel approach to simulate passive ROM and quantify ligament tension patterns.

When performing intraoperative assessments, the force applied by the surgeon serves as an mechanical actuator resulting in joint motion which is constrained by tension build-up in the surrounding soft tissues. The FE TKR model provides an efficient means of calculating ligament tensions by either applying external loads or joint kinematics to simulate passive ROM. This versatility to analyze ligament tensions by actuating the FE model using either force-driven or kinematically-driven inputs was utilized in Aims 2 and 3, respectively.

Aim 2 benefits from recent advances in technology making intraoperative kinematic data more readily available [26-28]. In a previous clinical study, knee kinematics were collected intraoperatively during passive flexion and were indicative of TKR functional outcome at two-year follow-ups [29]. This unique kinematic dataset was utilized in Chapter 4 to demonstrate FE TKR model calculated ligament tensions were sensitive to clinically observed variations in intraoperative kinematics and discriminated between TKR patient groups with good and poor functional outcomes.

During knee motion, soft tissues, and in particular ligaments, exhibit nonlinear force-displacement behavior and are nonuniformly loaded in unique recruitment patterns [30, 31] that are known to be impacted by TKR component alignment [32-35]. The previously cited clinical study that links abnormal intraoperative kinematics to poor post-operative functional outcomes highlights the significance of addressing knee instability during surgery [29]. Although it is assumed soft tissues are the responsible mechanism for

knee instability, the individual role each plays is unknown leaving surgeons without a clear approach to address the problem. The kinematically-driven passive FE TKR model produced in Chapter 4 was utilized in Chapter 5 to complete patient-specific simulations of passive ROM and identified ligaments featuring tension patterns characteristic of poor *in vivo* clinical TKR outcomes.

Completion of Aim 2 produced a TKR knee model that can input *in vivo* kinematics for simulating passive ROM and quantifying ligament tension patterns to discriminate TKR patients with different functional outcomes. The impact of this kinematically-driven model does not end with the clinical dataset utilized in this dissertation. Although patient-specific TKR component alignments and *in vivo* kinematics served as model inputs, model anatomy was generalized permitting the implementation of other kinematic datasets, albeit with corresponding TKR component geometries. It has been proposed that intraoperative knee kinematics could help tailor surgery to individual patients if a link between intraoperative measures and functional outcome could be established [36]. Aim 2 supports this initiative by utilizing passive kinematics to link intraoperative ligament tension to functional outcome. The discriminating ligament tension patterns reported provide a critical first step in a computational workflow that targets surgical decision-making.

Aim 3: Determine the effect of TKR alignment on ligament tensions using a validated force-driven passive FE knee model.

Aim 3 was accomplished by validating a specimen-specific FE TKR model under different TKR alignments using experimental data collected during *in vitro* cadaver testing. Chapter 6 detailed the design of the mechanical knee rig used for experimental simulation

of passive ROM and the subsequent development of a force-driven FE TKR model used for computational simulation and calculation of ligament tensions.

Joint motion requires the application of external loading, and during intraoperative TKR assessments, external loading is applied by the surgeon's hands at the ankle joint and mid-thigh. These passive assessments are based on the "feel" of the surgeon which refers to the forces they are applying; thus, a force-driven event. Therefore, the force-driven FE TKR model developed in Chapter 6 to simulate intraoperative assessments improved the representation of the clinical scenario compared to the kinematically-driven model applied in Chapters 4 and 5. Despite attempts to quantify target moment values during passive TKR assessments, a lack in clinical adoption leaves surgical external loading unquantified in the literature [37]. Furthermore, quantification of coupled joint motion and external loading during intraoperative assessments in order to appropriately validate a force-driven FE TKR model is unavailable. Chapter 6 completed *in vitro* cadaver testing to measure applied external loads and passive kinematics simultaneously during experimentally simulated intraoperative assessments, and thus, addressed this technical gap and provided model inputs (external loads) for a force-driven simulation and knee kinematics to validate the model against.

Other computational studies have demonstrated that TKR component alignment affects ligament tensions during weight bearing activity [35, 38, 39]; however, this relationship has not been quantified during passive conditions. The force-driven passive knee model validated in Chapter 6 provides an approach to quantify the effects of TKR component alignment on ligament tension during passive ROM. Furthermore, the

validated FE TKR model represented a diseased knee specimen that presented challenges when analyzing ligament tensions due to abnormal ligament properties and increased joint laxity. However, the ability to validate a diseased knee model was encouraging given that the overall intent of knee modeling is to prevent poor function, and has not been accomplished previously.

Regardless, the validated force-driven passive FE TKR model produced in Aim 3 provides a modeling foundation to quantify the relationship between TKR component alignment and intraoperative ligament tension. Additionally, Aim 3 produced a mechanical knee rig for experimental simulation of passive ROM. The combined experimental and computational workflow established can be repeated on additional knee specimens to further characterize intraoperative loading conditions and improve subjectivity in intraoperative assessments performed during TKR surgery.

Innovations

The innovation in this dissertation resides in both the overall approach of translating computational models to solve clinical problems as well as the methodology used to execute each specific aim. Although computational modeling has become a common tool in analyzing biomechanics of implanted systems, linking the model outputs to clinical outcomes has not been as prevalent. The access to unique clinical data and retrieval analysis has allowed for an integrated computational framework where *in vivo* information can be used to inform modeling decisions and model outputs can be compared directly to clinical outcomes. In Aim 1, retrievals of modular TKR components were used to reconstruct taper junction geometry and corrosion patterns evident on the taper surfaces

agreed with stress distributions calculated by the FE simulations. Furthermore, in development of the taper junction FE model, a novel approach for incorporating experimentally measured mechanical properties of a specific metal alloy from multiple datasets representing different manufacturing processes into a single generalized material constitutive model was achieved and successfully applied in order to compare elastoplastic and linear elastic analysis results.

In Aim 2 and 3, a dramatically new computational model capable of quantifying ligament tensions during intraoperative passive ROM was developed. Computational modeling provides versatility to investigate ligament tensions using either a kinematically-driven or force-driven simulation. In Aim 2, the kinematically-driven model allowed us to input existing *in vivo* kinematics (despite unknown external loads applied) uniquely available through our clinical collaborators in order to simulate passive ROM for TKR patients with different functional clinical outcomes. In Aim 3, external loads measured during passive ROM experimentally simulated on an innovative biomechanical knee rig were applied to force-driven model simulations. This combined computational approach allowed for a multi-level validation where completion of Aim 2 provided *in vivo* functional validation by demonstrating the model can discriminate TKR clinical outcomes and Aim 3 provided experimental validation by demonstrating the model can accurately reproduce experimental data. Successful completion of Aim 2 also provided a kinematically-driven model that can analyze other existing *in vivo* kinematic datasets collected intraoperatively in the absence of quantified external loading. The ability to link model results to clinical outcomes demonstrates the model can differentiate key clinical events (e.g. intraoperative

passive and stability assessments); thus, improving translation of model predictions to impact design and surgical decisions.

Future Directions

The full significance of the completed work does not reside in this dissertation in its entirety. Each Aim provided unique insights from model predictions, but more importantly, modeling foundations to further understand the complex relationships investigated beyond the reported findings. The elastoplastic FE taper junction model developed in Aim 1 can be used to further understand the role plastic deformation plays in taper junction performance and analyze the effect of other taper design parameters in addition to angular mismatch. Moreover, the method for defining elastoplastic material models allows alternative metal alloys to be implemented in the FE analysis. The kinematically-driven, passive FE TKR model developed in Aim 2 can utilize both preexisting and future kinematic datasets to further define intraoperative ligament tension patterns indicative of TKR functional outcome. Future work aimed at expanding the inclusion criteria of the model, such as validating anatomy-scaling techniques, will help maximize this potential. Furthermore, future work should incorporate data collected from intraoperative sensors in addition to kinematics to provide a link between model ligament tension and a quantitative metric currently used during surgery and to improve clinical translation of model predictions. Aim 3 provided a combined experimental and computational workflow for developing specimen-specific, force-driven, passive FE TKR models that is being replicated in on-going cadaver work. On-going and future experimental testing of passive knee motion should account for passive muscle restraint as

this contributed to kinematic constraint more than anticipated. Future work should also use the force-driven TKR model to investigate the effect TKR design has on intraoperative ligament tensions in order to further inform surgical decision-making.

General Conclusions

The overall theme of this dissertation is that the synergy between computational modeling and experimental testing provides more impactful information to complex problems than can be achieved when performed independently. Computational modeling can calculate measures difficult or impossible to obtain *in vitro* or *in vivo*, but adequate verification and validation with experimental data are essential to establish credibility in model predictions. The findings presented in this dissertation are provided by robust computational models that are supported by mechanical testing and clinical outcomes and that advance computational biomechanics.

References

[1] Arnholt CM, MacDonald D W, Tohfafarosh M, Gilbert JL, Rimnac CM, Kurtz SM, Klein G, Mont MA, Parvizi J, Cates HE, Lee G, Malkani A, Kraay M. Mechanically assisted taper corrosion in modular TKA. Journal of Arthroplasty. 2014, 29 Suppl. 2: 205-208.

[2] Pourzal R, Hall DJ, Ha HQ, Urban RM, Levine BR, Jacobs JJ, Lundberg HJ. Does surface topography play a role in taper damage in head-neck modular junctions? Clinical Orthopaedics and Related Research. 2016, 474: 2232-2242.

[3] Grupp TM, Weik T, Bloemer W, Knaebel HP. Modular titanium alloy neck adapter failures in hip replacement – failure mode analysis and influence of implant material. BMC Musculoskeletal Disorders. 2010, 11(3): 1-12.

[4] Goldberg JR, Gilbert JL, Jacobs JJ, Bauer TW, Paprosky W, Leurgans S, A multicenter retrieval study of taper interfaces of modular hip prostheses. Clinical Orthopaedics and Related Research. 2002, 401: 149-161.

[5] Lieberman JR, Rimnac CM, Garvin KL, Klein RW, Salvati EA, An analysis of the head-neck taper interface in retrieved hip prostheses. Clinical Orthopaedics and Related Research. 1994, 300: 162-167.

[6] Porter DA, Urban RM, Jacobs JJ, Gilbert JL, Rodriguez JA, Cooper HJ. Modern trunnions are more flexible: a mechanical analysis of THA taper designs. Clinical Orthopaedics and Related Research. 2014, 472: 3963-3970.

[7] Jani SC, Sauer WL, McLean TW, Lambert RD, Kovacs P. Fretting corrosion mechanisms at modular implant interfaces. American Society for Testing and Materials ASTM STP 1301. 1997.

[8] Goldberg JR, Gilbert JL. *In vitro* corrosion testing of modular hip tapers. Journal of Biomedical Material Research Part B: Applied Biomaterials. 2003, 64: 78-93.

[9] Jauch SY, Huber G, Haschke H, Sellenschloh K, Morlock MM. Design parameters and the material coupling are decisive for the micromotion magnitude at the stem-neck interface of bi-modular hip implants. Medical Engineering & Physics. 2014, 36: 300-307.

[10] Chu Y, Elias JJ, Duda GN, Frassica FJ, Chao EYS. Stress and micromotion in the taper lock joint of a modular segmental bone replacement prosthesis. Journal of Biomechanics. 2000, 33: 1175-1179.

[11] Lanting BA, Teeter MG, Vasarhelyi EM, Ivanov TG, Howard JL, Naudie DDR. Correlation of corrosion and biomechanics in the retrieval of a single modular neck total hip arthroplasty design: modular neck total hip arthroplasty system. Journal of Arthroplasty. 2015, 30: 135-140.

[12] Shareef N, Levine D. Effect of manufacturing tolerances on the micromotion at the Morse taper interface in modular hip implants using the finite element technique. Biomaterials. 1996, 17: 623-630.

[13] Donaldson FE, Coburn JC, Lohmann Siegel K. Total hip arthroplasty head-neck contact mechanics: A stochastic investigation of key parameters. Journal of Biomechanics. 2014, 47: 1634-1641.

[14] Van Citters DW, Martin AJ, Currier JH, Park S-H, Edidin AA, "Factors Related to Imprinting Corrosion in Modular Head-Neck Junctions," Modularity and Tapers in Total Joint Replacement Devices, ASTM STP1591, A. S. Greenwald, S. M. Kurtz, J. E. Lemons, and W. M. Mihalko, Eds., ASTM International, West Conshohocken, PA 2015: 83–98, doi:10.1520/STP159120140138.

[15] Witt F, Guhrs J, Morlock MM, Bishop NE. Quantification of the contact area at the head-stem taper interface of modular hip prostheses. Plos One. 2015, 10(8): 1-15.

[16] Zhang T, Harrison NM, McDonnell PF, McHugh PE, Leen SB. Micro-macro wear-fatigue of modular hip implant taper-lock coupling. Journal of Strain Analysis. 2013, 0(0): 1-17.

[17] Lundberg HJ, Ha NQ, Hall D J, Urban RM, Levine BR, Pourzal R. Contact mechanics and plastic deformation at the local surface topography level after assembly of modular head-neck junctions in modern total hip replacement devices. Modularity and Tapers in Total Joint Replacement Devices, ASTM STP1591. 2015: 59-82.

[18] Hernigou P, Queinnec S, Flouzat Lachaniette CH. One hundred and fifty years of history of the Morse taper: from Stephen A. Morse in 1864 to complications related to modularity in hip arthroplasty. International Orthopaedics. 2013, 37: 2081-2088.

[19] ASTM F1636-95e2, Standard specification for bores and cones for modular femoral heads (withdrawn 2001), ASTM International, West Conshohocken, PA, 1995, www.astm.org.

[20] Babazadeh S, Stoney JD, Lim K, Choong FM. The relevance of ligament balancing in total knee arthroplasty: how important is it? A systematic review of the literature. Orthopedic Reviews. 2009, 1:e26.

[21] Smith T, Elson L, Anderson C, Leone W. How are we addressing ligament balance in TKA? A literature review of revision etiology and technological advancement. Journal of Clinical Orthopaedics and Trauma. 2016, In Press.

[22] Kazemi M, Dabiri Y, Li LP. Recent advances in computational mechanics of the human knee joint. Computational and Mathematical Models in Medicine. 2013, 718423.

[23] Oh KJ, Park WM, Kim K, Kim YH. Quantification of soft tissue balance in total knee arthroplasty using finite element analysis. Computer Methods in Biomechanics and Biomedical Engineering. 2013, doi:10.1080/10255842.10252013.10765409.

[24] Steinbruck A, Woiczinski M, Weber P, Muller PE, Jansson V, Schroder C. Posterior cruciate ligament balancing in total knee arthroplasty: a numerical study with a dynamic force controlled knee model. Biomedical Engineering Online. 2014, 13:91.

[25] Zelle J, Heesterbeek PJ, de Waal MM, Verdonschot N. Numerical analysis of variations of posterior cruciate ligament properties and balancing techniques on total knee arthroplasty loading. Medical Engineering & Physics. 2010, 32:700-707.

[26] Omori G, Nishino K, Suzuki Y, Segawa H, Hayahsi T, Koga Y. Intraopertive measurements of knee motion in total knee arthroplasty. The Knee. 2003, 10:75-79.

[27] Belvedere C, Ensini A, Leardini A, Dedda V, Feliciangeli A, Cenni F, Timoncini A, Barbador P, Giannini S. Tibio-femoral and patello-femoral joint kinematics during navigated total knee arthroplasty with patellar resurfacing. Knee Surgery, Sports Traumatology, Arthroscopy. 2014, 22: 1719-1727.

[28] Mihalko WM, Mounawar A, Phillips MJ, Bayers-Thering M, Krackow KA. Passive knee kinematics before and after total knee arthroplasty. Journal of Arthroplasty. 2008, 23(1): 57-60.

[29] Lutzner J, Krischner S, Gunther KP, Harman MK. Patients with no functional improvement after total knee arthroplasty show different kinematics. International Orthopaedics. 2012, 36:1841-1847.

[30] Bankevoort L, Huiskes R, de Lange A. Recruitment of knee joint ligaments. Journal of Biomechanical Engineering. 1991, 113:94-103.

[31] Cyr AJ, Shalhoub SS, Fitzwater FG, Ferris LA, Maletsky LP. Mapping of contributions from collateral ligaments to overall knee joint constraint: an experimental cadaveric study. Journal of Biomechanical Engineering. 2015, 137:061006.

[32] Barrack RL, Schrader T, Bertot AJ, Wolfe MW, Myers L. Component rotation and anterior knee pain after total knee arthroplasty. Clinical Orthopaedics and Related Research. 2001, 392:46-55.

[33] Nagamine R, White SE, McCarthy DS, Whiteside LA. Effect of rotational malposition of the femoral component on knee stability kinematics after total knee arthroplasty. Journal of Arthroplasty. 1995, 10(3) 265-270.

[34] Song SJ, Detch RC, Maloney WJ, Goodman ST, Huddleston JI. Causes of instability after total knee arthroplasty. Journal of Arthroplasty. 2014, 29:360-364.

[35] Thompson JA, Hast MW, Granger JF, Piazza SJ, Siston RA. Biomechanical effects of total knee arthroplasty component malrotation: a computational simulation. Journal of Orthopaedic Research. 2011, 29:969-975.

[36] Young KL, Dunbar MJ, Richardson G, Astephen Wilson JL. Intraoperative passive knee kinematics during total knee arthroplasty surgery. Journal of Orthopaedic Research. 2015, 33: 1611-1619.

[37] Clarke JV, Wilson WT, Wearing SC, Picard F, Riches PE, Deakin AH. Standardising the clinical assessment of coronal knee laxity. Journal of Engineering in Medicine. 2012, 226(9):699-708.

[38] Fitzpatrick CK, Clary CW, Rullkoetter PJ. The role of patient, surgical, and implant design variation in total knee performance. J Biomech. 2012a, 45:2092-2102.

[39] Kuriyama S, Ishikawa M, Nakamura S, Furu N, Ito H, Matsuda S. Posterior tibial slope and femoral sizing affect posterior cruciate ligament tension in posterior cruciate-retaining total knee arthroplasty. Clinical Biomechanics. 2015, 30:676-681.

[40] Kang KT, Koh YG, Son J, Kwon OR, Baek C, Jung SH, Park KK. Measuring the effect of femoral malrotation on knee joint biomechanics for total knee arthroplasty using computational simulation. Journal of Bone & Joint Research. 2016, 5:552-559.